An Optically Recombined Laser Interferometer for Gravitational Wave Detection

Thesis by

Torrey T. Lyons

In Partial Fulfillment of the Requirements

for the Degree of

Doctor of Philosophy

California Institute of Technology

Pasadena, California

1997

(Submitted August 19, 1996)

LIGO P96035-00-I

To my Parents

Acknowledgments

I am indebted to my research advisor, Fred Raab, for years of patient tutelage, stimulating discussion, and most recently, for painstaking thesis proofreading. His humor, enthusiasm and knowledge have made my stay at Caltech enjoyable and rewarding.

I am also grateful to Robbie Vogt and Barry Barish who oversaw the LIGO project during my tenure here and provided an environment where I could learn and work without concern for the less glamorous aspects of doing science. Robbie Vogt in particular has served as my faculty advisor during the final part of my stay and has served as a source of useful advice and amusing stories.

I thank the entire LIGO team for their time, effort and encouragement. The 40-m interferometer in particular could not be run without the combined efforts of many people. I owe particular thanks to Martin Regehr, who laid the foundation for much of the theory in his own thesis, and was available even after he left Caltech to explain the more subtle points. In the lab, Andy Kuhnert was indispensable as co-worker and source of inspiration. He taught me that some scientific problems are best solved by stubborn determination and some, by going for beers, but that unfortunately, most are in the former category. I would also like to thank Stan Whitcomb and Aaron Gillespie who both provided helpful insights on many of the things that I investigated.

Many of the calculations described here were performed using MATLAB which was provided to the LIGO Project by The MathWorks, Inc., as a research grant.

This work was supported by the National Science Foundation cooperative agreement number PHY-9210038.

Abstract

Kilometer scale interferometers for the detection of gravitational waves are currently under construction by the LIGO (Laser Interferometer Gravitational-wave Observatory) and VIRGO projects. These interferometers will consist of two Fabry-Perot cavities illuminated by a laser beam which is split in half by a beam splitter. A recycling mirror between the laser and the beam splitter will reflect the light returning from the beam splitter towards the laser back into the interferometer. The positions of the optical components in these interferometers must be controlled to a small fraction of a wavelength of the laser light. Schemes to extract signals necessary to control these optical components have been developed and demonstrated on the tabletop. In the large scale gravitational wave detectors the optical components must be suspended from vibration isolation platforms to achieve the necessary isolation from seismic motion. These suspended components present a new class of problems in controlling the interferometer, but also provide more exacting tests of interferometer signal and noise models.

This thesis discusses the first operation of a suspended-mass Fabry-Perot-Michelson interferometer, in which signals carried by the optically recombined beams are used to detect and control all important mirror displacements. This interferometer uses an optical configuration and signal extraction scheme that is planned for the full scale LIGO interferometers with the simplification of the removal of the recycling mirror. A theoretical analysis of the performance that is expected from such an interferometer is presented and the experimental results are shown to be in generally good agreement.

Table of Contents

List of Tables

List of Figures

Chapter 1: Introduction

General Relativity interprets gravity as a curvature of space and time which is produced by mass. The theory predicts that accelerating mass can produce propagating waves of space-time curvature, known as gravitational waves, in an analogous fashion to accelerating charge producing propagating electromagnetic waves. Gravitational waves will appear to inertial observers as producing a fluctuating strain such that the distance between the observers will shrink and expand as a wave goes by in proportion to the distance between the observers.

The lowest order moment of a mass distribution which can accelerate in an oscillatory manner is the quadrupole moment. The monopole moment is fixed due to conservation of energy and the oscillations in the dipole moment are forbidden due to conservation of momentum. This is in contrast to electromagnetic waves where the dominant radiation term is from oscillatory dipole moments. Thus, gravitational waves are quadrupolar in nature and produce a fluctuating shear strain transverse to the direction of propagation. This is shown pictorially in Figure 1-1.

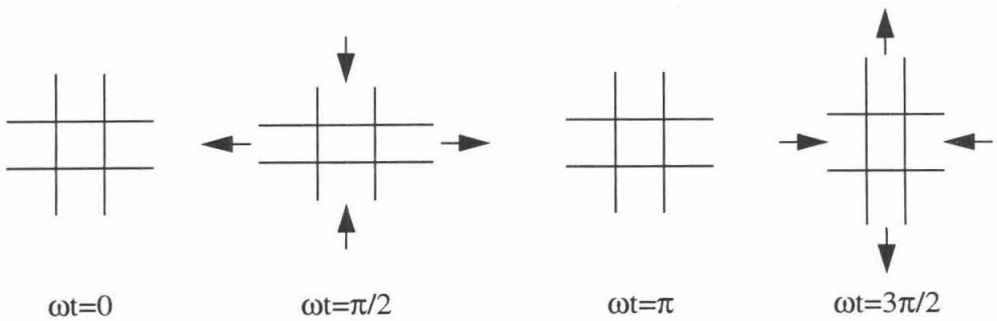

Figure 1-1: Effect of a gravitational propagating into the paper. For one-half of its period, one axis is stretched and the other shrunk, while for the other half of its period it has the opposite effect.

The magnitude of the strain produced by a gravitational wave can be estimated by the quadrupole formula:

$$h \approx \frac{G}{c^4 r} \frac{d^2 Q}{dt^2} \qquad 1\text{-}1$$

where G is the gravitational constant, c is the speed of light, D is the distance to the source of the gravitational wave and Q is the quadrupole moment of the source. Note, d^2Q/dt^2 has units of energy. It is, roughly speaking, the kinetic energy of the quadrupole moment of the mass. The size of the gravitational wave strain is very small as in SI units, $G/c^4 \approx 9\times10^{-45}$ $s^2\,kg^{-1}\,m^{-1}$. Thus to emit appreciable gravitational waves requires a solar mass object being accelerated to a significant fraction of the speed of light in second time scales. For such astrophysical objects,

$$h \sim 10^{-20} \left(\frac{d^2 Q/dt^2}{M_{SUN} c^2} \right) \left(\frac{10 \text{ Mpc}}{r} \right) \qquad 1\text{-}2$$

Thus, objects 10 Mpc (30 million light years) away whose quadrupolar mass moments have kinetic energies one-tenth the mass energy of the sun will produce a strain of 10^{-21} here on earth. 10 Mpc is the distance to the Virgo cluster. To see such exceptionally violent events with a reasonable event rate we will need to be able to detect them out to at least this distance. A strain of 10^{-21} corresponds to 10^{-18} m of relative motion over a 1 km base-line. This is believed to be the threshold of what can be achieved with the next generation of gravitational wave detectors at frequencies near a few hundred Hz.

Direct detection of gravitational waves would provide further confirmation of Einstein's theory of General Relativity. More importantly, however, if the waves can be

detected with reasonable signal-to-noise ratio, they will provide a wealth of information about astrophysical objects that is inaccessible through electromagnetic observations.

1.1 Gravitational Wave Detectors

Three types of gravitational wave detectors have been developed or planned.[1] The original efforts to detect gravitational waves used a resonant bar. [1][2][3] All external disturbances are reduced as much as possible by suspending the bar in a cryogenic vacuum system with additional seismic isolation. A sensor monitors the energy in the quadrupole vibrational modes of the bar. A passing gravitational wave may excite these resonant modes which would be seen as a signal.

Resonant bar detectors have the advantages of simplicity and comparatively low cost. The resonant response of the bar increases its sensitivity to gravitational waves at the frequencies of its resonant modes, but provides little information on the waveform. This is a fundamental disadvantage of bar detectors and it appears that interferometric gravitational wave detectors can more easily provide a high level of broadband sensitivity.

Interferometric gravitational wave detectors are the focus of this thesis. An obvious candidate for measuring the transverse shear strain produced by a gravitational wave is a Michelson interferometer shown in Figure 1-2 and in fact early detectors used this configuration. [4][5][6] The antisymmetric port is held on a dark fringe. A passing gravitational wave from directly overhead will cause the length of one arm of the interferometer to decrease and the other to increase, thus disturbing the dark fringe at the antisymmetric

1. Doppler tracking of spacecraft, pulsar timing, and the anisotropy of the cosmic microwave background can also be used to detect gravitational wave radiation. However, these experiments do not employ equipment that is dedicated to the task of gravitational wave detection.

port and providing a signal.

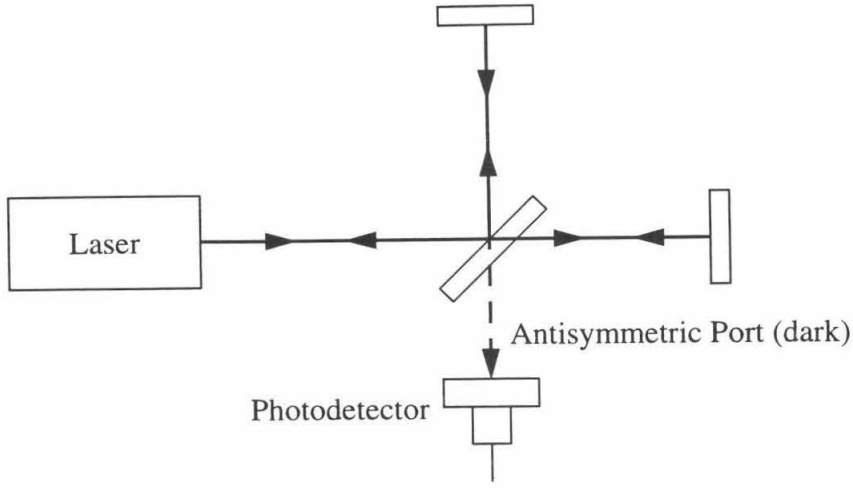

Figure 1-2: Michelson interferometer.

The primary advantage of an interferometric gravitational wave detector is its broad-band response. This allows the extraction of the full gravitational waveform. By increasing the length of the arms the strain sensitivity for a given displacement sensitivity can be increased linearly.[1] More advanced optical topologies are also used in current interferometric detectors to provide additional sensitivity. The main disadvantage of an interferometric detector is its complexity.

A third type of gravitational wave detector being pursued is a proposed space based interferometric detector. As proposed by the LISA project, [7] a space based detector would consist of six spacecraft in a triangular formation with two of the spacecraft at each vertex. The six spacecraft would be in a heliocentric orbit and would function together as a Michelson interferometer. Having six spacecraft would provide some redundancy in case

1. When the length of the interferometer exceeds a quarter of the wavelength of the gravitational wave, the sensitivity no longer increases with increasing length. For the frequencies that earth based interferometers will be sensitive to, this limit is approximately 100 km.

up to two of the spacecraft failed (though not at the same vertex).

The advantages to a space based detector is that the baseline may be made tremendously long,[1] leading to increased strain sensitivity for a given displacement sensitivity, and that the test masses will be in freefall and subject to little external disturbances. This type of detector has the potential to probe the frequency band from 10^{-1} to 10^{-4} Hz which will never be accessible to earth based detectors because of terrestial disturbances. An obvious disadvantage to a space based detector is the high cost.

1.2 The LIGO Project

The goal of the LIGO (Laser Interferometer Gravitational-wave Observatory) project [8] is to make the first direct detection of gravitational waves and to use these waves to learn about violent events in the distant universe. The LIGO project is currently building two 4 km long laser interferometer gravitational-wave detectors, one near Hanford, Washington, and the other near Livingston, Louisiana. This joint project of the California Institute of Technology and the Massachusetts Institute of Technology is funded by the U.S. National Science Foundation.

LIGO operates a 40 meter long interferometer on the campus of the California Institute of Technology which is used in studying the noise sources limiting interferometric detectors and as a prototype for the larger interferometers under construction. Most of the work described in this thesis took place on the 40-m interferometer as part of its ongoing research program.

---

1. The current design calls for a baseline distance between spacecraft in one arm of 5×10^{6} km.

1.3 Noise in Laser Interferometers

Laser interferometer gravitational wave detectors have many noise sources which could limit their ultimate sensitivity. The three fundamental noise sources which we believe will limit the LIGO detectors are seismic noise, thermal noise and photon shot noise as shown in Figure 1-3. [9] In practice our experience with the 40-m interferometer has shown us that other noise sources due to mechanical, optical, or electrical imperfections often limit the sensitivity over some part of the frequency band. One of the challenges for the 40-m interferometer research program is to gain the experience necessary to assure that LIGO will not be limited by these technical noise sources.

Seismic noise includes all external disturbances which are translated mechanically from the external world to the mirrors. In addition to the earth's natural ground motion, there is also man-made ground motion from traffic and machinery among other things, as well as acoustic vibrations of the vacuum system to contend with. To isolate the mirrors from the outside world, the mirrors are suspended as pendula at the top of seismic isolation stacks. This ensures that seismic noise only limits the detector performance below approximately 50 Hz and is attenuated sufficiently at higher frequencies.

Thermal noise arises because the test masses and pendulum suspensions are at room temperature and have $\frac{1}{2} k_B T$ of energy in each degree of freedom. In principle thermal noise could be reduced by cooling down the masses and suspensions, but this would be prohibitively expensive. Instead the thermal motion is concentrated into high Q resonant peaks which are either out of the gravitational wave band or sufficiently narrow that only a small amount of detection bandwidth is lost. The energy in each resonant peak is invariant

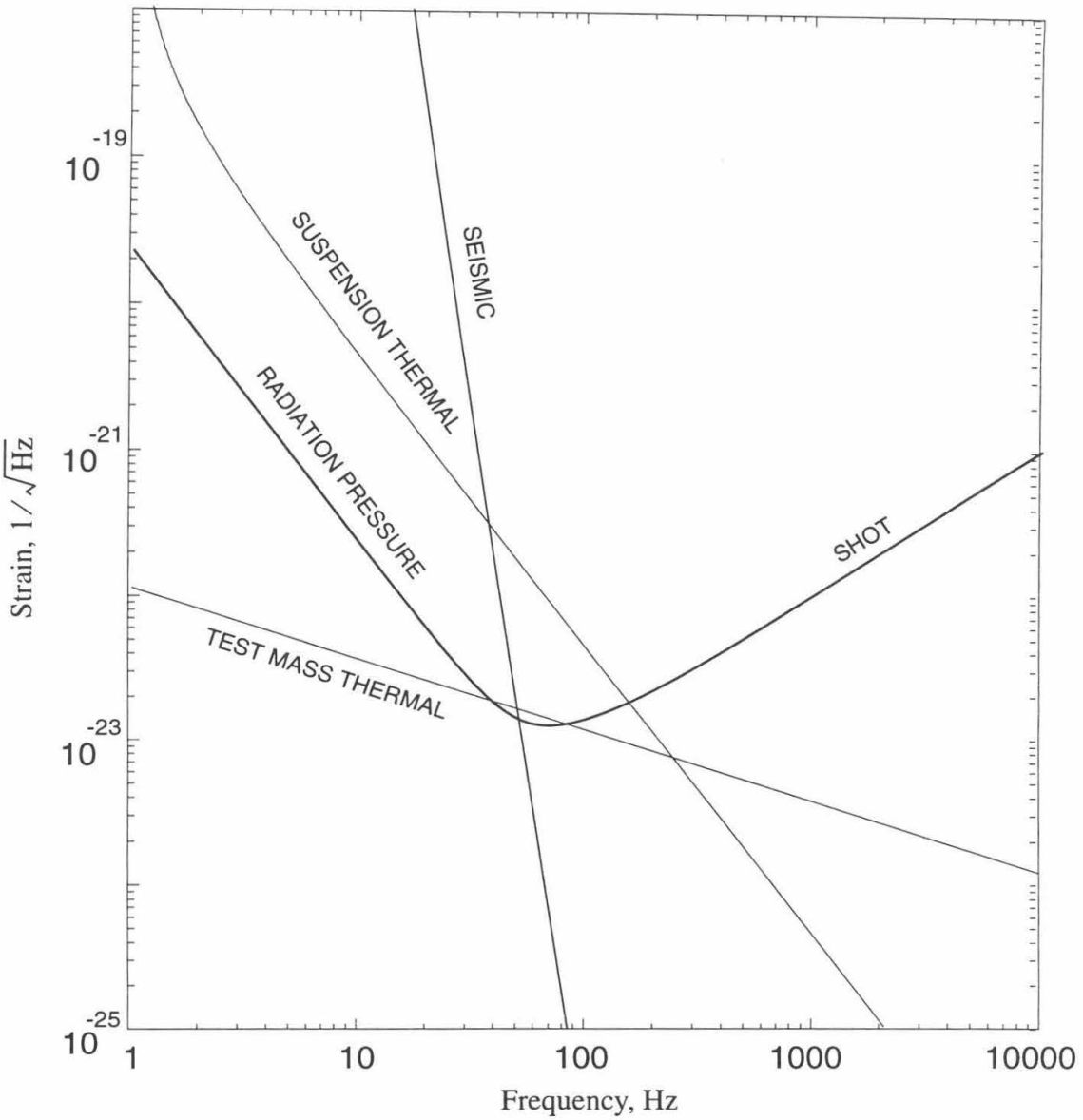

Figure 1-3: Initial LIGO interferometer sensitivity.

so that increasing the Q of the peak raises the height of the peak by lowering the off resonance wings. By careful experimental design the off resonance thermal motion can be made small enough that it is only expected to limit the gravitational wave sensitivity from 50 to 200 Hz.

Photon shot noise is due to the fact that the laser light is quantized into discrete photons. The number of photons arriving at a photodetector per unit time obeys Poisson statistics and thus there is some uncertainty in our measurement of the power at the photodetectors. This uncertainty limits our ability to measure the relative phases of the light returning from both arms of the interferometer and hence the arm length difference. By increasing the number of photons available to the interferometer through higher power lasers and lower loss mirrors, the problems of counting statistics can be reduced. The effects of shot noise can also be reduced by using optical schemes more complicated than the simple Michelson interferometer, designed to maximize the amount of information extracted per input photon. These optical schemes are discussed in Section 1.4 and the implementation of one such optical scheme in the 40-m interferometer is the focus of this thesis.

Most of the noise characterization discussed in this thesis and carried out in the 40-m interferometer is in the frequency domain. Some work has been done to characterize the noise in the time domain. Because this thesis is focused on exploring an optical topology with the ultimate goal of improving the high frequency sensitivity of gravitational wave interferometers, it was only natural that the author's work in the time domain has focused on signals with high frequency components. Because this effort was otherwise unrelated to the focus of this thesis, these results are discussed in Appendix B.

1.4 Optical Topologies

The sensitivity of the Michelson interferometer can be improved by having the light make several round trips in each arm by inserting another mirror between the beam splitter

and the end mirror. The most conceptually simple way to do this is using an optical delay line, where the light strikes the mirrors in a different spot on each round trip. [5] This method will be used in arms of the GEO 600 effort to detect gravitational waves. [10] Another way to do this is to have the light return back to the same spot on both mirrors and form a Fabry-Perot resonant cavity. [11] Such a cavity is said to be resonant when the light entering through the partially transmitting front mirror interferes constructively with the light travelling back and forth inside it. Near resonance the phase of the light returning from the cavity is very sensitive to the deviation from resonance and thus the effect of a small displacement produced by a gravitational wave on the dark fringe at the antisymmetric port is amplified.

The shot noise limited sensitivity can be improved by increasing the amount of power incident on the beam splitter. Because the light returning from the two arms interferes destructively at the antisymmetric port, the light returning towards the laser must interfere constructively. By inserting a partially transmitting "recycling mirror" between the beam splitter and the laser, this power may be redirected into the interferometer and reused. Of course the recycling mirror must be positioned so that light it reflects back into the interferometer interferes constructively with the light transmitted through it from the laser. This technique which increases the effective laser power is known as power recycling. [12]

The optical topology chosen for LIGO and the French-Italian gravitational wave detector, VIRGO, [13] is a power recycled interferometer with Fabry-Perot arm cavities as shown in Figure 1-4. Various methods have been proposed to extract the signals necessary to maintain the optical elements in their optimal positions. The focus of this thesis work

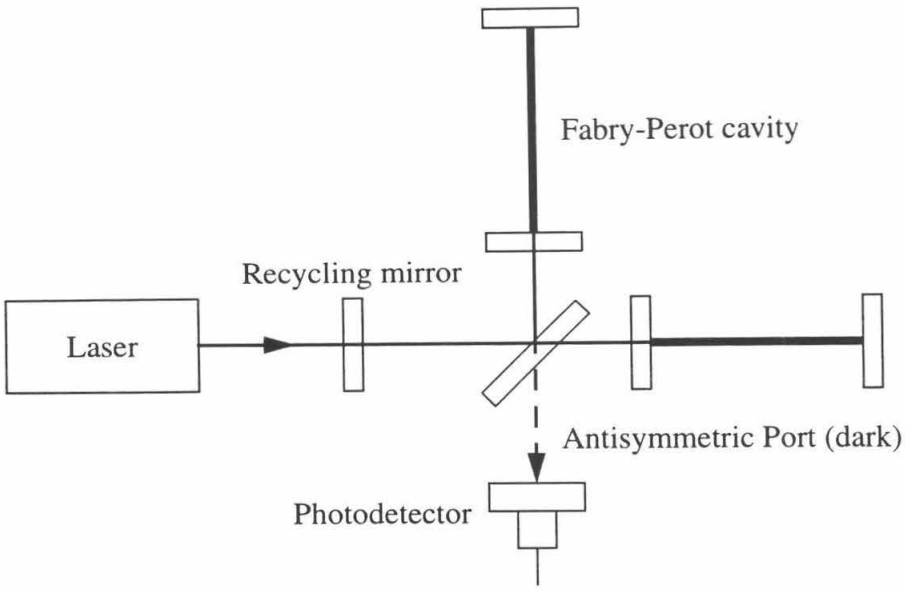

Figure 1-4: Power recycled interferometer with Fabry-Perot arm cavities.

was to implement one such scheme without the added complexity of the recycling mirror in the 40-m interferometer. This was the first time that a control scheme that was easily extensible to a power recycled interferometer has been demonstrated in a suspended interferometer.

The start of this work marked an important turning point for the research program of the 40-m interferometer. Previous work had concentrated almost entirely on improving the displacement sensitivity of the interferometer, primarily by understanding and reducing technical noise sources. By late 1994 it was believed that, except for the frequency band from 100-300 Hz, the 40-m interferometer sensitivity was limited only by the three fundamental noise sources expected for LIGO and that the scaling of these noise sources to LIGO sizes was understood. (See Figure 1-5.) At this point a decision was reached to move from improving the displacement sensitivity to demonstrating the technology

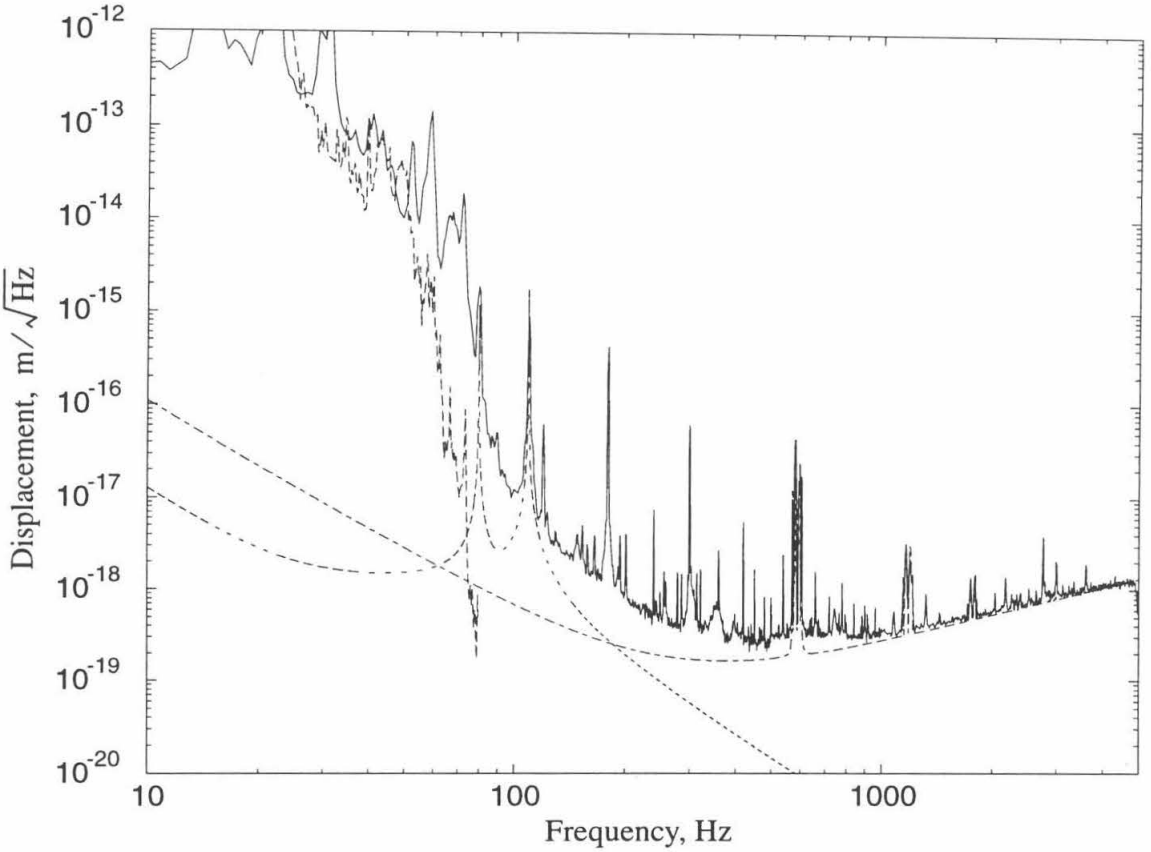

Figure 1-5: 40-m interferometer displacement noise spectrum on October 28, 1994, (solid) with estimated contribution from seismic noise (dashed), shot noise and thermal noise due to vibrations of the test mass and suspension wires (dot-dashed), and thermal noise in the test mass tilt resonances (dotted).

needed for LIGO before the final design for the various LIGO subsystems was frozen. The first step in this demonstration was the length sensing and control scheme which is described in this thesis.

Chapter 2: Recombination Theory

The initial interferometer design chosen for LIGO is an asymmetric power recycled Michelson with Fabry-Perot arm cavities as shown in Figure 2-1, hereafter referred to simply as a recycled interferometer. Four degrees of freedom need to be controlled. These are the recycling cavity length $(l_1 + l_2)$, the Michelson near-mirror difference $(l_1 - l_2)$, the common mode arm cavity length $(L_1 + L_2)$, and the arm cavity length difference $(L_1 - L_2)$ which gives the gravitational wave signal. Two schemes for extracting signals proportional to these degrees of freedom have been evaluated in previous theses. [15][16]

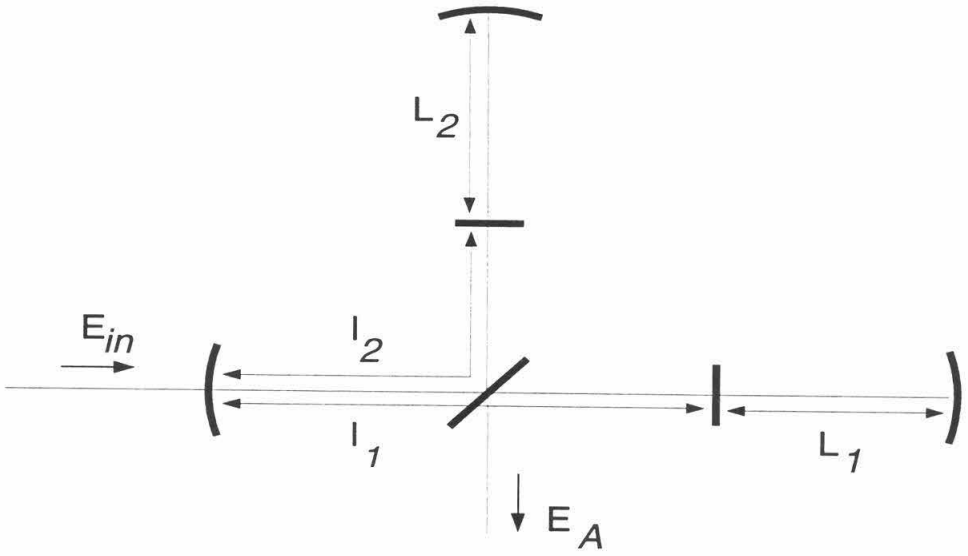

Figure 2-1: Asymmetric power recycled Michelson with Fabry-Perot cavities.

Since its original commissioning, until April 5, 1995, the 40-m interferometer was operated as a Fabry-Perot interferometer as shown in Figure 2-2.[1] In this configuration the

1. In this figure the demodulation phase is modulo 2π with respect to 0° demodulation defined by the phase of the sidebands as they are incident on the vertex test masses. The phases can be different for the two arms in general. In practice these phases are adjusted empirically to maximize the desired signal.

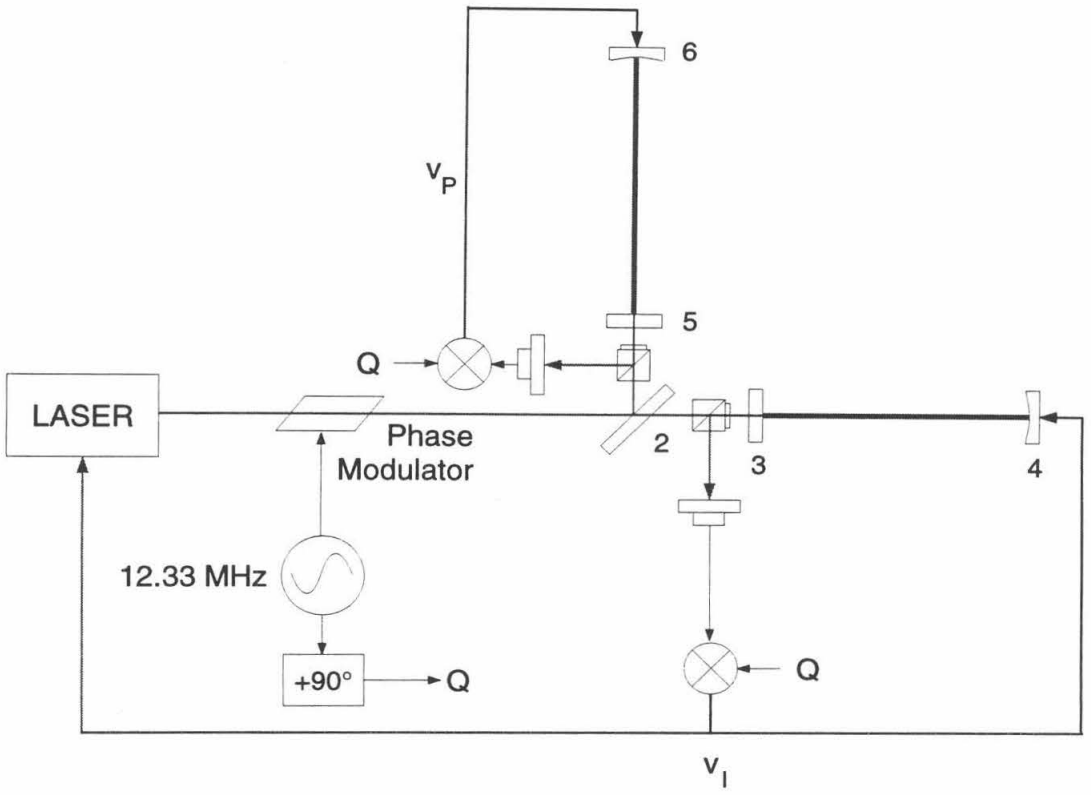

Figure 2-2: Fabry-Perot interferometer configuration.

light returning from the two arms was independently sensed by two photodiodes. As a result of the calculations described below, the decision was made to proceed in steps towards the goal of a recycled interferometer. The modification of the 40-m interferometer to a recombined optical topology using the asymmetry signal extraction scheme as shown in Figure 2-3 was the first step and is the focus of this thesis research. Preparations are currently underway to demonstrate a recycled optical topology in the 40-m interferometer.

The original plan adopted was to include both signal extraction schemes for sensing the auxiliary degrees of freedom[1] in the initial LIGO detectors. [17] This decision was

1. Auxiliary degrees of freedom are all degrees of freedom except for the arm cavity length difference which provides the gravitational wave signal.

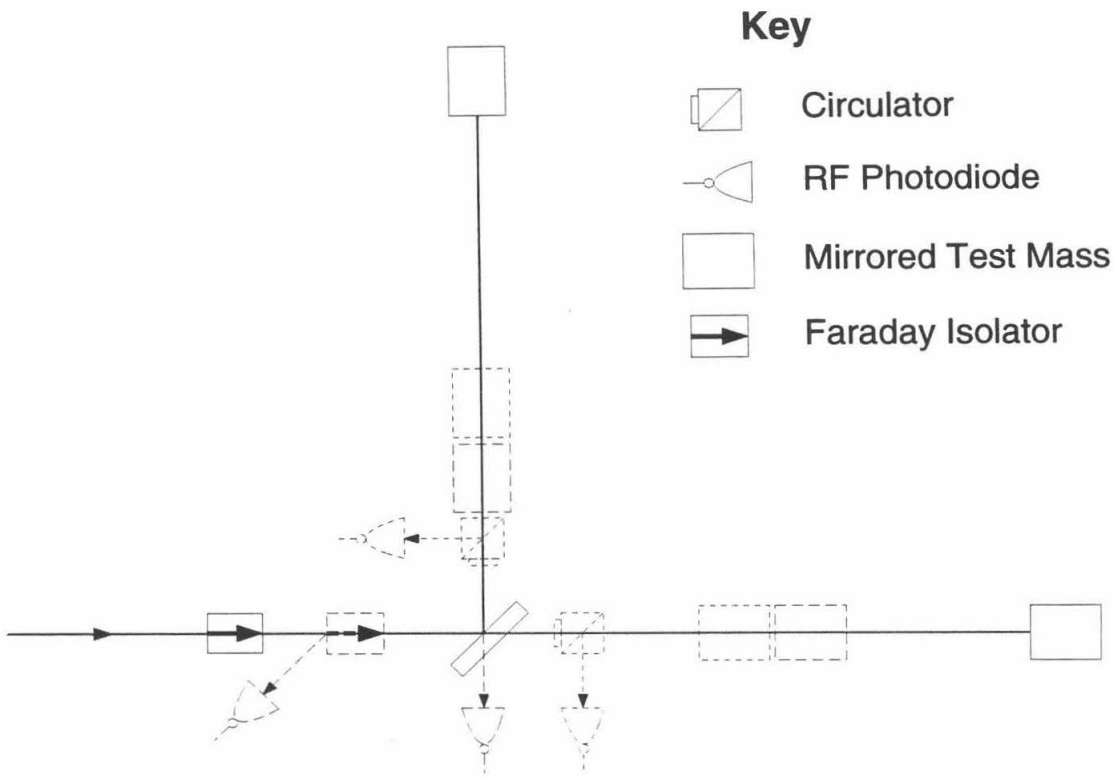

Figure 2-3: Physical modifications to the 40-m interferometer to change from a Fabry-Perot interferometer to recombined interferometer. Elements shown as dotted were moved or removed while the dashed elements show the new locations or elements that were added.

reached because of concerns about lock acquisition using the asymmetry signal extraction scheme. Partially as a result of this thesis work and its success in acquiring lock as described in Section 3.1, the decision has been made to only implement the asymmetry signal extraction scheme in the initial LIGO.

A diagram of the recombined optical topology with asymmetry scheme signal extraction is shown in Figure 2-4.[1] The beam splitter and arm cavity mirrors are labelled as mir-

1. In this figure the demodulation phase is modulo 2π with respect to 0° demodulation defined by the phase of the sidebands as they are incident on the beam splitter. In practice the demodulation phases are adjusted empirically as discussed in Section 3.3.

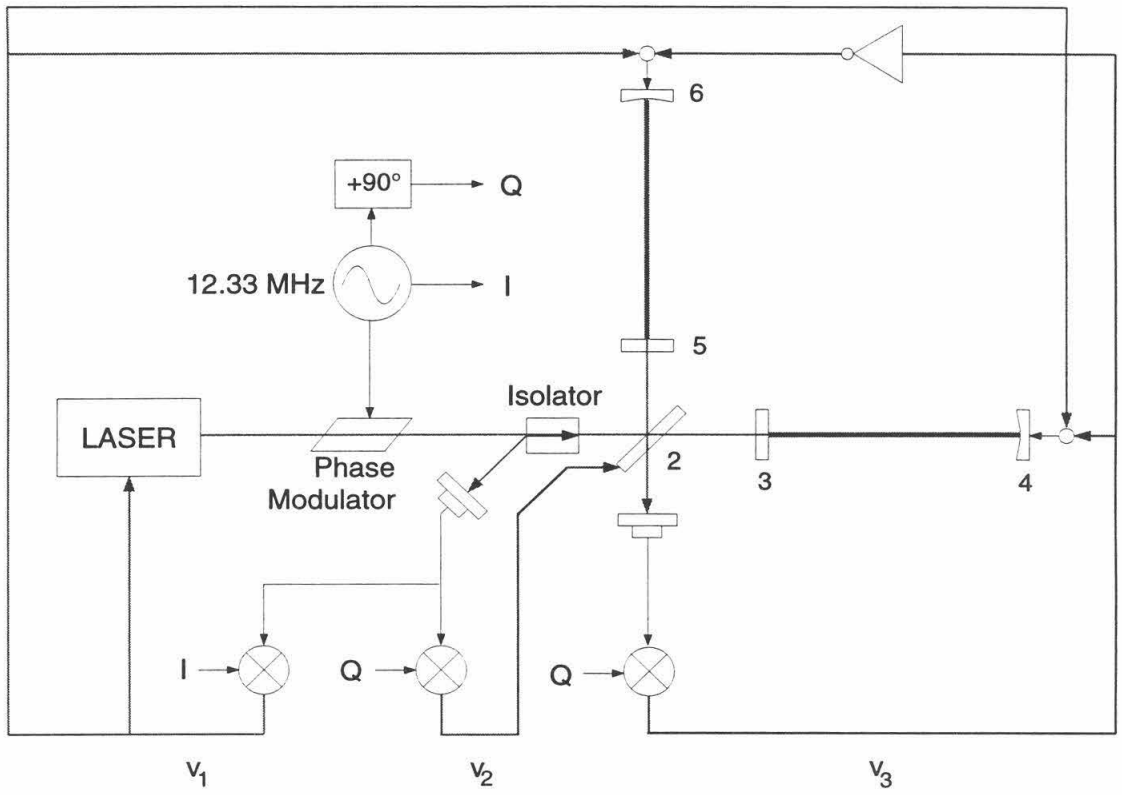

Figure 2-4: Recombined optical and servo topology.

rors 2 through 6.[1] For a non-recycled interferometer, the $l_1 + l_2$ degree of freedom is not important. The asymmetry is the DC value of $l_1 - l_2$.[2] The three extracted signals are v_1, v_2, and v_3. The signal v_1 is used to control the common mode arm cavity length and is fed back to the laser frequency servo. The signal v_2 is fed back to control the beam splitter position. And, the signal v_3 is used to control the differential arm cavity length. All three signals depend primarily on the degree of freedom they control, but also have some depen-

1. This convention is to maintain the same numbering scheme as papers on recycling where the recycling mirror would be mirror 1.
2. In a non-recycled interferometer these lengths are defined relative to the beam splitter instead of the recycling mirror.

dence on the other degrees of freedom.

2.1 Fabry-Perot Cavities

Here we consider the fields present in the Fabry-Perot arm cavities and derive their dependence on the round-trip phase. A Fabry-Perot cavity is formed in gravitational wave interferometers by aligning two mirrored test masses such that light can resonate in between them. In general the term applies to any two reflective surfaces which light can resonate between.

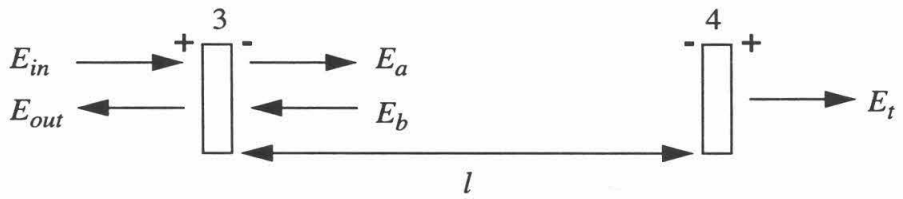

Figure 2-5: Fabry-Perot cavity.

Consider the Fabry-Perot cavity shown in Figure 2-5. The two mirrors, labelled 3 and 4, are separated by a distance l.[1] Mirror 3 has amplitude transmission t_3, reflectivity r_3, and scattering plus absorption loss l_3, and similarly for mirror 4. We shall denote the energy transmission, reflectivity and loss with capital letters: $T_3 = t_3^2$, $R_3 = r_3^2$, and $L_3 = l_3^2$. Of course,

$$T_3 + R_3 + L_3 = 1 \qquad 2\text{-}1$$

The amplitude transmission and reflectivity are in general complex numbers, but we

1. The mirrors are numbered 3 and 4 to use the same numbering scheme as used to describe the whole interferometer.

shall treat them as real without loss of generality. Any self-consistent sign convention for the reflectivities will yield the same results, except that the round-trip phase required for resonance will be different. We take the convention which is most physical: reflectivities from inside the cavity are negative.[1] This is because the mirrors are coated on the side facing into the cavity. The reflection occurs at the coating-glass interface and the coating has a lower index of refraction than the glass. Reflections going from a medium with a lower index of refraction to a higher index of refraction result in a phase change of $180°$.

The fields are related to one another by the following expressions:[2]

$$E_a = t_3 E_{in} - r_3 E_b \qquad 2\text{-}2$$

$$E_b = -r_4 e^{i\phi} E_a \qquad 2\text{-}3$$

$$E_{out} = r_3 E_{in} + t_3 E_b \qquad 2\text{-}4$$

$$E_t = t_4 e^{i\phi/2} E_a \qquad 2\text{-}5$$

where ϕ is the round-trip phase acquired by the laser beam in travelling from mirror 3 to 4 and back. $\phi = 2kl - 2\phi_{Guoy}$ where k is the wave number of the light and ϕ_{Guoy} is the Guoy phase discussed in more detail in Section 2.3. Solving these equations we get:

$$E_a = \frac{t_3}{1 - r_3 r_4 e^{i\phi}} E_{in} \qquad 2\text{-}6$$

---

1. This is not the convention used by M. Regehr in [20] for example, but his results are mathematically equivalent, if somewhat counter-intuitive physically.
2. Note that we use the phase convention from [14] that plane-wave fields traveling toward $z > 0$ are of the form

$$E(z, t) = E_0 e^{ikz - iwt}$$

$$E_b = -\frac{t_3 r_4 e^{i\phi}}{1 - r_3 r_4 e^{i\phi}} E_{in} \qquad 2\text{-}7$$

$$\begin{aligned} E_{out} &= \left(r_3 - \frac{T_3 r_4 e^{i\phi}}{1 - r_3 r_4 e^{i\phi}} \right) E_{in} \\ &= \frac{r_3 - (1 - L_3) r_4 e^{i\phi}}{1 - r_3 r_4 e^{i\phi}} E_{in} \end{aligned} \qquad 2\text{-}8$$

$$E_t = \frac{t_3 t_4 e^{i\phi/2}}{1 - r_3 r_4 e^{i\phi}} E_{in} \qquad 2\text{-}9$$

To achieve a resonance condition for the light in the cavity using the phase convention we have used here, $\phi = 0$, modulo 2π.

It is useful to consider these fields on resonance. Doing this we can define several important arm cavity parameters we will use in later calculations. The ratio between the power incident on a cavity and the power inside the cavity on resonance, travelling in the same direction as the incident light, is the cavity power gain, G_{arm}.

$$G_{arm} = \left| \frac{E_a}{E_{in}} \right|^2_{\phi = 0} = \frac{T_3}{(1 - r_3 r_4)^2} \qquad 2\text{-}10$$

The power transmitted through an arm cavity on resonance, divided by the input power, is $T_{arm} = T_4 G_{arm}$, as one would expect. The amplitude reflectivity of the compound mirror formed by a Fabry-Perot arm cavity on resonance we shall denote by r_{arm}.

$$r_{arm} = \left. \frac{E_{out}}{E_{in}} \right|_{\phi = 0} = \frac{r_3 - (1 - L_3) r_4}{1 - r_3 r_4} \qquad 2\text{-}11$$

We also will use the obvious notation for the power reflectivity on resonance, $R_{arm} = r_{arm}^2$.

The arm power reflectivity is related to an important parameter that is often measured in the lab, the visibility of a Fabry-Perot cavity. The visibility is defined as

$$V = \frac{P_{max} - P_{min}}{P_{max}} \qquad 2\text{-}12$$

where $P_{\max}$ is the maximum power reflected back from the arm cavity and $P_{\min}$ is the minimum power reflected back, which occurs when the cavity is on resonance. Note that for high reflectivity mirrors, as we will always be concerned with in this thesis, $P_{\max}$ is very nearly equal to the incident power. In this case the visibility is particularly useful because it is the fraction of the incident power that is coupled into the cavity on resonance. The maximum visibility that can be achieved in a Fabry-Perot cavity is

$$V_{max} \approx 1 - R_{arm} \qquad 2\text{-}13$$

In practice, mismatches between the spatial mode of the incident light and the TEM_{00} eigenmode of the cavity will limit the visibility actually achieved to be somewhat lower than this. The mode matching fraction, M, is the ratio of the visibility achieved to the maximum visibility that could have been achieved due to mirror reflectivities and loss.

The derivatives of the cavity fields with respect to the round-trip phase will also prove to be very useful. Let us first consider the derivative of the arm cavity reflectivity evaluated on resonance, which we shall denote by r_{arm}'.

$$r_{arm}' = \frac{\partial}{\partial \phi}\left(\frac{E_{out}}{E_{in}}\right)\bigg|_{\phi = 0} = \frac{-i\,T_3\,r_4}{(1 - r_3\,r_4)^2} \qquad 2\text{-}14$$

It is also instructive to calculate the derivative of the phase of this quantity as phase will prove to be the most important parameter of the light returning from the arm cavities. A useful relation to remember is that $\mathrm{Re}\left[\frac{1}{i\,A}\frac{\partial A}{\partial \phi}\right]$ is the derivative of the phase of A with respect to ϕ.[1] Consider,

$$N' \equiv \frac{E_{in}}{i\,E_{out}}\frac{\partial}{\partial \phi}\left(\frac{E_{out}}{E_{in}}\right) = \frac{-T_3\,r_4\,e^{i\phi}}{(1-r_3\,r_4\,e^{i\phi})[r_3-(1-L_3)\,r_4\,e^{i\phi}]} \qquad 2\text{-}15$$

$\mathrm{Re}[N']$ is the *phase gain* of the cavity.[2] It is the ratio of the rate at which the phase of the light returning from the cavity changes when moving one mirror, relative to the rate at which this phase would change if the other mirror were absent. Having a resonant arm cavity then amplifies the phase change seen in the light reflected from it when its length is changed by the factor $\mathrm{Re}[N']$. Similarly we can define,

$$N \equiv \frac{E_{in}}{i\,E_b}\frac{\partial}{\partial \phi}\left(\frac{E_b}{E_{in}}\right) = \frac{1}{1-r_3\,r_4\,e^{i\phi}} \qquad 2\text{-}16$$

$\mathrm{Re}[N]$ is known as the *bounce number.*[3] It is the ratio of the rate at which the phase of the light inside the cavity returning to the front mirror changes when the rear mirror moves,

---

1. This can be shown as follows:

$$\left[A = x + iy \;\; \arg A = \mathrm{atan}\left(\frac{y}{x}\right)\right] \quad \frac{\partial}{\partial \phi}(\arg A) = \frac{x\frac{\partial y}{\partial \phi} - y\frac{\partial x}{\partial \phi}}{x^2+y^2}$$

$$\frac{1}{A}\frac{\partial A}{\partial \phi} = \frac{\frac{\partial x}{\partial \phi} + i\frac{\partial y}{\partial \phi}}{x+iy} = \frac{x\frac{\partial x}{\partial \phi} + y\frac{\partial y}{\partial \phi} + i\left(x\frac{\partial y}{\partial \phi} + y\frac{\partial x}{\partial \phi}\right)}{x^2+y^2}$$

$$\therefore \; \mathrm{Re}\left[\frac{1}{i\,A}\frac{\partial A}{\partial \phi}\right] = \frac{\partial}{\partial \phi}(\arg A)$$

2. In [20] this quantity is called the augmented bounce number.
3. The term bounce number is historical and comes from the fact that it is directly analogous to the number of mirror reflections in a delay line interferometer.

relative to the rate this phase would change if the front mirror were absent. As we do not have access to this internal cavity field, this quantity is typically not as useful.

Another quantity that is traditionally defined is the finesse of a Fabry-Perot cavity,

$$F = \frac{\pi\sqrt{r_3 r_4}}{1 - r_3 r_4} \qquad 2\text{-}17$$

It is the ratio of the frequency separation between adjacent resonant transmission peaks to the width of the transmission peaks. The finesse is typically used as a measure of the frequency resolution of a Fabry-Perot, particularly in applications where the cavity is being used as a frequency analyzer.

It is sometimes useful to remember approximately how some of the quantities defined above are related. In the case that will always be considered here where r_3 and r_4 are very nearly equal to one, we have the following relations,

$$N'|_{\phi = 0} \approx \left|\frac{G_{arm}}{r_{arm}}\right| \qquad 2\text{-}18$$

$$N|_{\phi = 0} \approx \frac{F}{\pi} \qquad 2\text{-}19$$

2.2 Interferometer Parameters

The parameters used in the calculations discussed below are shown in Table 2-1. The losses quoted are representative of what is typically seen from in-situ measurements in the 40-m interferometer and are assumed to be split evenly between the mirrors.[1] Both arms appear to have a much higher loss than what was expected from measurements of individ-

1. For a high finesse Fabry-Perot cavity it is not important where the losses are distributed.

ual test masses in the optics lab. The mirror losses are important parameters and a reasonable estimate of the losses that could be expected were needed in considering the feasibility of a recombined topology before in-situ measurements were available. How these estimates were obtained is discussed in detail in Appendix A.

The arm cavity input couplers have regions of increased transmission by 4 - 9 ppm in their centers with FWHM of 5 mm.[1] The transmission values given are measured from in-situ measurements of the degree of overcoupling of the cavities. [18] These values are 20 ppm higher for both input mirrors than the transmissions measured in the optics lab before installation in the 40-m interferometer. This is likely due to a chemical cleaning process the test masses were subjected to before being installed, but after the optics lab measurements were taken.[2] This may also explain some of the increased losses. This process was tried as an alternative to drag wiping and as a potential method which could be used in-situ.

The asymmetry used was the maximum that could reasonably be accommodated in the 40-m interferometer vacuum system. The modulation frequency had been used since the lab was constructed. It was originally selected to be high enough so that the argon-ion laser's intensity noise was shot noise limited, to be away from other RF sources,[3] and to be

---

1. This defect is an artifact of the coating process.
2. The chemical cleaning process was recommended by H.A. Atwater and is known as SC1 in the electronics industry. It removes organics and group IB and IIB metals through reactions of H_2O_2, NH_4OH, and deionized H_2O. The process was to soak the optic in an ultrasonic bath of acetone for 5 minutes. The optic was next soaked in an ultrasonic bath of methanol for 5 minutes. Then the optic was immersed in a solution of H_2O_2 : NH4OH : H_2O (deionized) in a ratio of 1:1:5 at 80°C for 5 minutes. Finally the optic was rinsed in 18 MΩ deionized water. This process was originally developed to clean the surface of silicon wafers before coating them and etches away the surface layers of the material. It is likely that the resulting change in the thickness of the topmost silicon dioxide layer of the mirror coating was responsible for the transmission change.
3. Radio stations are the typical source of concern.

Table 2-1: Parameters for the 40-m Interferometer

Quantity	Symbol	Value
Mirror (power) transmissions	T_2	0.45
	T_3	280 ppm
	T_5	300 ppm
	T_4, T_6	12 ppm
Loss in each mirror	L_3, L_4	110 ppm
	L_5, L_6	56 ppm
Asymmetry	δ	50.8 cm
Modulation frequency	f_{mod}	12.33 MHz
Modulation index	Γ	1.49
Contrast defect	$1 - C$	0.03

a frequency for which a crystal reference can easily be purchased. The modulation index is selected for best performance acquiring lock as is discussed in Section 3.2.

For a laser interferometer with Fabry-Perot arms, the definition of contrast is somewhat ambiguous. The definition we shall use here is:

$$C \equiv \frac{P_B - P_D}{P_B + P_D} \qquad 2\text{-}20$$

where P_B and P_D are the maximum and minimum power in the carrier light measured at the antisymmetric port. P_B will be measured when both arm cavities are off resonance and there is constructive interference at the antisymmetric port,[1] while P_D will be measured

1. Effectively, P_B equals the incident power. One could also define P_B to be measured with the arm cavities held on resonance. In this case P_B would equal the incident power times the arm cavity visibility.

when both arm cavities are on resonance and there is destructive interference at the anti-symmetric port.

2.3 Matrix of Discriminants

For a recombined interferometer there are three degrees of freedom which need to be controlled. We shall find it useful to consider the deviation of these three degrees of freedom from their optimal operating point both in units of meters and round-trip phase at the laser frequency. We denote these distances by,

$$\Delta_+ = L_1 + L_2 - \Delta_+^{DC} \quad \delta_- = l_1 - l_2 - \delta_-^{DC} \quad \Delta_- = L_1 - L_2 - \Delta_-^{DC} \qquad 2\text{-}21$$

where Δ_+^{DC} and Δ_-^{DC} are the optimal static common and differential mode lengths and δ_-^{DC} is the optimal static Michelson near mirror difference (asymmetry). Note that the nominal value of δ_-^{DC} is δ. It will often prove useful to write the asymmetry in units of propagation phase at the modulation frequency, which we shall denote by

$$\alpha = \frac{2\pi f_{\mathrm{mod}} \delta}{c} \qquad 2\text{-}22$$

When expressing these distances in units of round-trip phase, we must remember the Guoy phase which is a phase deficit due to finite transverse size of the laser beam. The phase shift on axis of a laser beam that has traversed a distance, z, from its waist is: [19]

$$\Phi(z) = \frac{2\pi}{\lambda} z - (l + m + 1) \operatorname{atan}\left(\frac{z}{z_0}\right) \qquad 2\text{-}23$$

where,

$$z_0 = \frac{\pi w_0^2}{\lambda} \qquad 2\text{-}24$$

is the confocal beam parameter, and l and m are the x and y mode numbers of the TEM_{xy} mode. The 40-m interferometer is operated on a TEM_{00} mode. (l=m=0) The Guoy phase (second term on right of Eq. 2-23) is important in that it discriminates between the transverse resonances. The cavity can be designed so that if TEM_{00} mode is resonant, the only other modes to match the resonance condition in the cavity will be very high order. If the incident light contains negligible power in these very high order modes, the transverse mode resonating in the cavity will be purely TEM_{00}. In the calculations that follow we shall ignore the Guoy phase as it has a much smaller dependence on z than the propagation phase.

Writing the three degrees of freedom in units of round trip phase at the laser frequency, and ignoring the Guoy phase, we have,

$$\Phi_+ = \frac{4\pi}{\lambda}\Delta_+ \quad \phi_- = \frac{4\pi}{\lambda}\delta_- \quad \Phi_- = \frac{4\pi}{\lambda}\Delta_- \qquad 2\text{-}25$$

The optimal operating point for these degrees of freedom are that they equal zero, modulo 2π.

We can extract signals proportional to the three degrees of freedom by demodulating the light returning towards the laser at the symmetric port and the light emerging from the antisymmetric port.[1] The light at the symmetric port we demodulate with two different

1. The side of the beam splitter facing towards the laser is called the symmetric port because for equal arm lengths in a simple Michelson interferometer, the light at this port interferes constructively and carries a signal proportional to the average of the arm lengths, while the light at the antisymmetric port interferes destructively and carries a signal proportional to the difference of the arm lengths.

phases to give us two independent signals. Each of these signals is largely dependent only on one degree of freedom. The matrix which specifies the change in a particular signal induced by a change in a degree of freedom is the matrix of discriminants. It gives the relative sensitivity each extracted signal has to the three degrees of freedom that need to be controlled.

The matrix of discriminants can be calculated analytically in steady state by making simplifying approximations. In particular, the assumption was made that the beam splitter had equal transmission and reflectivity and that the arms had equal mirror transmissions and reflectivities.[1] This was done for the asymmetry signal extraction by M. Regehr [20] and the results for a recombined interferometer are shown below.

$$\frac{\partial v_1}{\partial \Phi_+} = E_l^2 J_0(\Gamma) J_1(\Gamma) \cos\alpha \left| r_{\text{arm}}' \right| \qquad 2\text{-}26$$

$$\frac{\partial v_2}{\partial \phi_-} = -E_l^2 J_0(\Gamma) J_1(\Gamma) \sin\alpha \, r_{\text{arm}} \qquad 2\text{-}27$$

$$\frac{\partial v_2}{\partial \Phi_-} = E_l^2 J_0(\Gamma) J_1(\Gamma) \sin\alpha \, r_{\text{arm}} \frac{T_3 \, r_4}{(1 - r_3 \, r_4)^2} \qquad 2\text{-}28$$

$$\frac{\partial v_3}{\partial \phi_-} = E_l^2 J_0(\Gamma) J_1(\Gamma) \sin\alpha \, r_{\text{arm}} \qquad 2\text{-}29$$

$$\frac{\partial v_3}{\partial \Phi_-} = -E_l^2 J_0(\Gamma) J_1(\Gamma) \sin\alpha \left| r_{\text{arm}}' \right| \qquad 2\text{-}30$$

The other matrix elements equal zero under the approximations used to generate these

1. The assumption of equal transmissions and reflectivities in the two arms is why Eq. 2-28 includes only a factor depending on mirrors 3 and 4 and not 5 and 6 as well.

expressions. Our current unbalanced beam splitter transmission and reflectivity and unequal arm cavity losses mix the common and differential modes which leads to all the matrix elements being non-zero in practice.

As the basis for most of our following calculations, we shall use the matrix of discriminants calculated by an improved version of the DC numerical model developed by Martin Regehr.[1] This program, written in Mathematica, starts with the expression for the light reflected from a Fabry-Perot cavity as shown in Eq. 2-8. Using this and the propagation phases, it finds symbolic expressions for all the fields in the interferometer. It then symbolically differentiates these expressions to find the derivatives of mixer outputs with respect to the propagation phases. These symbolic expressions are typically quite long as no approximations are made other than that of only considering the carrier, first and second order sidebands. Numerical values for the interferometer parameters as shown in Table 2-1 are substituted into these expressions by the program to give the matrix of discriminants.

The relative sensitivities of the signals to changes in the three degrees of freedom calculated with the numerical model is shown in Table 2-2, normalized so that the gravitational wave readout sensitivity is one.[2] Thus for example,

$$\frac{\partial v_1}{\partial \Phi_+} = -7.8 \qquad 2\text{-}31$$

Notice that the sensitivity to arm cavity common mode motion is higher than the sensitiv-

1. The program was improved by Jim Mason to increase its speed and fix a minor coding error, and the ability for it to treat light that is not correctly mode matched into the arm cavities was added by the author.
2. The matrix of discriminants calculated here were verified independently by R. Weiss using a different numerical model.

ity to differential motion. This is because the small 50-cm asymmetry provides poor transmission of the RF sidebands to the antisymmetric port and good transmission to the symmetric port.[1] The off-diagonal terms arise predominantly because of the unbalanced beam splitter and arm cavity reflectivities. These break the symmetry of the interferometer and cause mixing of the common and differential mode signals.

Table 2-2: Extracted Relative Signal Sensitivities

	∂v_1	∂v_2	∂v_3
$\partial\Phi_+$	−7.8	0	-2.2×10^{-1}
$\partial\phi_-$	2.3×10^{-4}	1.9×10^{-4}	-1.9×10^{-4}
$\partial\Phi_-$	2.5	1.6×10^{-8}	1.0

Numerical models also exist to calculate this matrix at DC and higher frequencies. [21] These results can easily be simplified to the case of the recombined interferometer. In fact, the frequency dependence of the matrix of discriminants has a very simple form in this case as we shall show in Section 2.6.

2.4 Shot Noise in the Gravitational Wave Signal

Photon shot noise is an important noise source at higher frequencies in gravitational wave interferometers. The motivation for more complicated optical layouts than a Michelson interferometer and the resulting increase in complexity of the control system is to improve the shot noise limited performance. Here we derive the differential mode displacement equivalent to shot noise in a recycled interferometer. [22] The addition of the

1. This will improve when the interferometer is recycled.

recycling mirror in this case does not add to the difficulty of the general analysis. The only specific case we shall consider is a recombined interferometer, by setting the recycling mirror transmission equal to one.

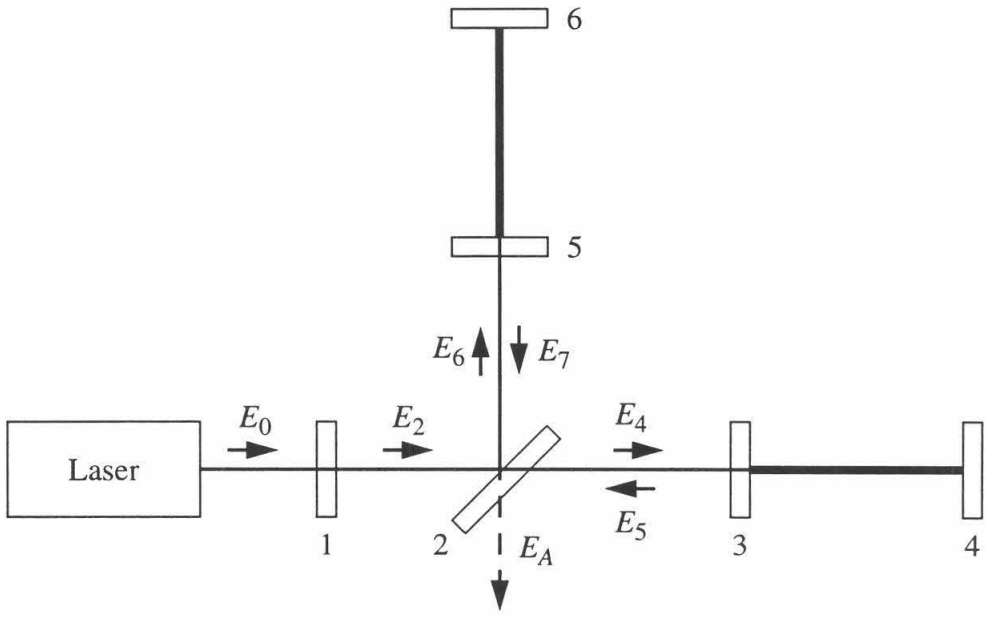

Figure 2-6: Recycled interferometer with mirrors and optical fields labelled.

A recycled interferometer with the mirrors and fields labelled is shown in Figure 2-6. The light incident from the laser is E_0. The light is phase modulated between the laser and the interferometer which impresses sidebands on the light which are shifted above and below the laser frequency (carrier) by the modulation frequency and multiples of it. The carrier light leaving the antisymmetric port is E_A which is typically very small in the absence of a signal because the antisymmetric port is held on a dark fringe for the carrier. Because of the asymmetry the sidebands are not on a dark fringe at the antisymmetric port. We adopt the phase convention that the first order sidebands have real amplitudes of opposite sign when incident on the beam splitter. The second order sidebands have equal

real amplitudes of the same sign. We will neglect terms in the calculation of order Γ^3 because the modulation depth is small. Thus, we will only need to consider up to second order sidebands. The transmission of the nth-order sideband from incidence on the beam splitter to the antisymmetric port is $\pm i \sin n\alpha$, where positive indicates the upper sideband and negative, the lower sideband.[1] The total complex field amplitude at the antisymmetric port is

$$E_{\text{anti}} = E_A + iE_+ e^{i\omega t} + iE_+ e^{-i\omega t} + iE_{2+} e^{2i\omega t} - iE_{2+} e^{-2i\omega t} \qquad 2\text{-}32$$

where ω is the angular modulation frequency, and E_+ and E_{2+} are the magnitudes of the first order and second order sideband fields at the antisymmetric port.

The detection system is modeled as a photodetector, a demodulator and a low-pass filter as shown in Figure 2-7. The low-pass filter may not be explicitly built as a separate element following the mixer output, but in practice all of the servo loops that derive their error signals from the mixer outputs have unity gain frequencies that are low compared to the modulation frequency. Thus we shall ignore in our analysis any signals at the mixer output that are at or above the modulation frequency.

A gravitational wave interacting with the detector will produce the same differential mode signal as shaking mirror 4 by some other means. If we displace mirror 4 such that

---

1. The nth-order sideband transmission to the anti-symmetric port is

$$t_{n\pm} = \frac{1}{2}(e^{2i(k \pm nK)l_1} - e^{2i(k \pm nK)l_2})$$

where K equals the wavenumber at the modulation frequency. Let $l = \frac{1}{2}(l_1 + l_2)$. Then, neglecting unimportant phase factors and accounting for the carrier being on a dark fringe,

$$\begin{aligned} t_{n\pm} &= \frac{1}{2}(e^{2i(k+nK)(l+\delta/2)} - e^{2i(k+nK)(l-\delta/2)}) \\ &= \frac{1}{2}(e^{\pm inK\delta} - e^{\mp inK\delta}) \\ &= \pm i \sin n\alpha \end{aligned}$$

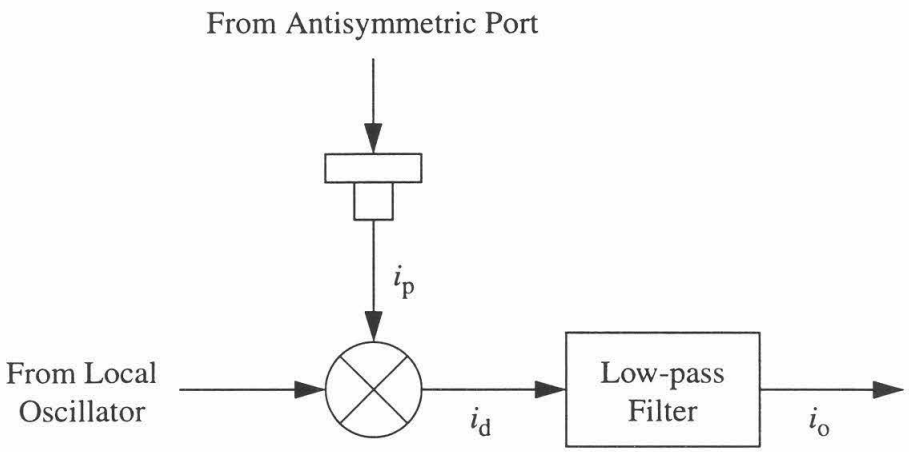

Figure 2-7: Detection system for the antisymmetric port light.

$x_4 = x_0 \sin \Omega t$, for sufficiently small x_0, this will produce a signal at the antisymmetric port given by:[1]

$$E_A = E_{DC} - i k E_2 \frac{T_3 r_4}{(1 - r_3 r_4)^2} \frac{x_0 \sin(\Omega t + \psi)}{\sqrt{1 + (\Omega/\omega_c)^2}} \qquad 2\text{-}33$$

where k is the wave number of the light, E_{DC} is the field due to the contrast defect which comes from any non-interfering light on the photodetector, ω_c is the cavity pole angular frequency,

$$\omega_c = \frac{c}{2l} \frac{1 - r_3 r_4}{r_3 r_4} \qquad 2\text{-}34$$

and ψ is a phase factor irrelevant to this analysis. The modulation sidebands do not enter the arm cavities and thus are not affected by the motion of mirror 4.

If we express the fields in units of $\sqrt{\text{photoelectrons/second}}$, the photocurrent, i_p, is[2]

1. This is derived in Appendix C.

$$\begin{aligned} i_p &= \left|E_A + iE_+ e^{i\omega t} + iE_+ e^{-i\omega t} + iE_{2+}e^{2i\omega t} - iE_{2+}e^{-2i\omega t}\right|^2 \\ &= |E_A|^2 + 2E_+{}^2 + 4E_+ \mathrm{Im}[E_A]\cos\omega t - 2E_+{}^2\cos 2\omega t - 4E_{2+}\mathrm{Re}[E_A]\sin 2\omega t \end{aligned} \qquad 2\text{-}35$$

The photocurrent has components at DC, ω and 2ω. The effect of the mixer and low pass filter is to pick out the ω component, which is

$$4kE_2E_+\frac{T_3 r_4}{(1-r_3 r_4)^2}\frac{x_0\sin(\Omega t+\psi)}{\sqrt{1+(\Omega/\omega_c)^2}}\cos\omega t \qquad 2\text{-}36$$

Because the photocurrent is modulated, it will be important to treat the shot noise as a nonstationary random process and to consider the actual demodulation waveform used. [23]

The effective demodulation waveform used in the 40-m interferometer is cosinusoidal demodulation. Square wave demodulation is used at the mixer, but the band-pass filter centered on the modulation frequency which is built into the photodiode makes this effectively cosinusoidal demodulation. This is because the square wave can be decomposed as a sum of sine waves at odd multiples of the modulation frequency, each of which mix with the corresponding component of the photocurrent to produce a signal after the low pass filter. The band-pass filter on the photodiode effectively eliminates all these higher frequency components in the photocurrent, so that only the pure sine wave demodulation term is important. Since the optimum demodulation phase is in quadrature, the demodulation is cosinusoidal.

So multiplying the component of the photocurrent at ω by cosω*t*, we find

---

2. Working in these units simplifies the formulas in our analysis.

$$i_d = 4kE_2E_+\frac{T_3 r_4}{(1-r_3 r_4)^2}\frac{x_0\sin(\Omega t+\psi)}{\sqrt{1+(\Omega/\omega_c)^2}}\cos^2\omega t \qquad 2\text{-}37$$

The low-pass filter has a corner frequency that is much less than the modulation frequency. Thus, the component of $\cos^2\omega t$ at DC will pass through, while the component at 2ω will not so that

$$i_o = 2kE_2E_+\frac{T_3 r_4}{(1-r_3 r_4)^2}\frac{x_0\sin(\Omega t+\psi)}{\sqrt{1+(\Omega/\omega_c)^2}} \qquad 2\text{-}38$$

We define *H(f)* as the transfer function from x_0 to i_o.

$$\begin{aligned}|H(f)| &\equiv \left|\frac{\tilde{i}_o(f)}{\tilde{x}_0(f)}\right| \\ &= 2k|E_2|E_+\frac{T_3 r_4}{(1-r_3 r_4)^2}\frac{1}{\sqrt{1+(\Omega/\omega_c)^2}}\end{aligned} \qquad 2\text{-}39$$

where $\tilde{i}_o$ and $\tilde{x}_0$ denote the Fourier transforms of i_o and x_0.

To quantify the noise performance of the interferometer, we must characterize the random process ***x(t)*** corresponding to the output in the absence of any signal.[1] Early treatments of the shot noise assumed it was stationary and ignored the effect of the modulation of the photocurrent. [24] Stationary noise is most conveniently represented using the one-sided power spectrum $S_{xx}(f)$ of ***x(t)***. $S_{xx}(f)$ is defined as the Fourier transform of the auto-correlation function $R_{xx}(\tau)$ of ***x(t)***:

1. We shall use boldfaced symbols in our notation here to mean random processes and $E\{\}$ to mean the expectation value or ensemble average.

$$R_{xx}(\tau) = E\{\boldsymbol{x}(t+\tau)\boldsymbol{x}(t)\}$$
$$S_{xx}(f) = 2\int_{-\infty}^{\infty} R_{xx}(\tau)e^{2\pi if\tau}d\tau \qquad 2\text{-}40$$

If $\boldsymbol{x}(t)$ is the input of a linear system, whose transfer function is $H(f)$, and $\boldsymbol{y}(t)$ is the output, then

$$S_{yy}(f) = |H(f)|^2 S_{xx}(f) \qquad 2\text{-}41$$

The output $\boldsymbol{i_o}(t)$ of our model, in the absence of a signal, is not stationary since it fluctuates at the modulation frequency. However, it is cyclostationary, which is to say that for any t, the statistics of $\boldsymbol{i_o}(t)$ are the same as those of $\boldsymbol{i_o}(t+T)$, where T is the period of modulation. Cyclostationary random processes have, for the most part, traditionally been treated as if they are stationary by simply averaging the statistical parameters over one cycle. Thus we can define the average autocorrelation and power spectrum:

$$\overline{R_{xx}}(\tau) = \frac{1}{T}\int_{t}^{t+T} R_{xx}(t'+\tau, t')dt'$$
$$\overline{S_{xx}}(f) = 2\int_{-\infty}^{\infty} \overline{R_{xx}}(\tau)\, e^{2\pi if\tau}\, d\tau \qquad 2\text{-}42$$

Averaging in this way is equivalent to modeling the time reference or phase of the cyclostationary process as a random variable which is uniformly distributed over one cycle. In this case the phase-randomized process is stationary. [25][26] This type of analysis is appropriate where the cyclostationary random process is not synchronized with the modulation. This is appropriate here as the shot noise is not synchronized with the modulation. In this situation all the concepts used for stationary random processes such as power spec-

tra are useful and the relation

$$\overline{S_{yy}}(f) = |H(f)|^2 \, \overline{S_{xx}}(f) \qquad 2\text{-}43$$

holds true.

Our goal then is to calculate $\overline{S_{i_o i_o}}(f)$, the average power spectrum of the interferometer output. We begin by finding $\overline{S_{i_d i_d}}(f)$. The details of the derivation are in Appendix D; the result is:

$$\begin{aligned}\overline{S_{i_d i_d}}(f) = {} & 3E_+^{\,2} + E_{DC}^{\,2} \\ & + (9E_+^{\,4} + 6E_{DC}^2 E_+^{\,2} + E_{DC}^{\,2} + 4E_{2+}^2 E_{DC}^2)\, \delta(2\pi f - \omega) \\ & + (E_+^4 + 4E_{2+}^2 E_{DC}^2)\, \delta(2\pi f - 3\omega)\end{aligned} \qquad 2\text{-}44$$

This power spectrum has two sharp components, one at the modulation frequency, and one at its third harmonic, as well as a broadband component. It is only the broadband component which interests us, since it falls into the gravitational wave frequency band. The low-pass filter in our model of the detection system will leave this part of the noise spectrum unaffected and will attenuate the very high frequency components. Therefore,

$$\overline{S_{i_o i_o}}(f) = 3E_+^{\,2} + E_{DC}^{\,2} \qquad 2\text{-}45$$

Finally, the displacement noise in one test mass equivalent to shot noise is found by substituting from Eq. 2-39 and Eq. 2-45:

$$\begin{aligned}\overline{S_{x_4 x_4}}(f)^{1/2} &= \frac{\overline{S_{i_o i_o}}(f)^{1/2}}{|H(f)|} \\ &= \frac{\sqrt{3E_+^{\,2} + E_{DC}^{\,2}}}{2k|E_2|E_+} \frac{(1 - r_3 r_4)^2}{T_3 r_4} \sqrt{1 + \left(\frac{2\pi f}{\omega_c}\right)^2}\end{aligned} \qquad 2\text{-}46$$

2.5 Shot Noise in the Auxiliary Signals

The signals which are used to control the common mode arm length and the beam splitter may also be shot noise limited at higher frequencies. An estimate of their shot noise limited sensitivity can be found in a relatively straightforward manner from the shot noise limit for the differential mode, given in Eq. 2-46. The shot noise limited sensitivity to common mode motion will have the same frequency dependence as the shot noise limit for the differential motion[1] while the beam splitter shot noise limit is flat. This is because the shape of the shot noise curves are the inverse of the sensitivity curves which are discussed in Section 2.6.

We can approximate the ratio between the DC sensitivities to common mode and differential mode motion by scaling by the powers falling on the two detectors and the sensitivity of each detector to phase variations in the sensed degree of freedom. P_S is the power of the light returning to the laser which is deflected by an optical isolator and P_A is the power of the light exiting the antisymmetric port. We also define η_S and η_A as the quantum efficiencies of the corresponding photodiodes. These quantum efficiencies include the effects of the attenuators and other optics placed before the photodiode. The signal sensing the Φ_+ degree of freedom is proportional to $\eta_S \, \partial v_1 / \partial \Phi_+$, and the signal sensing the ϕ_- degree of freedom is proportional to $\eta_S \, \partial v_3 / \partial \phi_-$. The shot noise on the symmetric port photodiode, which senses both the common mode and beam splitter motion, is proportional to $\sqrt{\eta_S P_S}$. Using the analogous relations for the differential mode degree of free-

1. That is, the single cavity pole from Eq. 2-34.

dom we find

$$\left(\frac{S_{\Phi_+}(0)}{S_{\Phi_-}(0)}\right)^{\frac{1}{2}} \approx \left(\frac{P_S}{P_A}\right)^{\frac{1}{2}} \left(\frac{\eta_A}{\eta_S}\right)^{\frac{1}{2}} \frac{\partial v_3/\partial \Phi_-}{\partial v_1/\partial \Phi_+} \qquad 2\text{-}47$$

$$\left(\frac{S_{\phi_-}(0)}{S_{\Phi_-}(0)}\right)^{\frac{1}{2}} \approx \left(\frac{P_S}{P_A}\right)^{\frac{1}{2}} \left(\frac{\eta_A}{\eta_S}\right)^{\frac{1}{2}} \frac{\partial v_3/\partial \Phi_-}{\partial v_2/\partial \phi_-} \qquad 2\text{-}48$$

where $S_{\Phi_+}^{1/2}$ is the shot noise limited sensitivity to the Φ_+ degree of freedom and similarly for $S_{\Phi_{-+}}^{1/2}$ and $S_{\phi_-}^{1/2}$.

Shot noise in the auxiliary signals sets a lower bound on the residual motion of the auxiliary degrees of freedom in the gravitational wave band. The feedthrough of motion in the auxiliary degrees of freedom to the v_3 signal sets a corresponding lower bound on the gravitational wave displacement sensitivity. This limit could in general be above or below the limit set by shot noise in the v_3 signal itself. Let us define $S_{\Phi_+ \to \Phi_-}(f)^{1/2}$ which is the shot noise limited sensitivity to differential mode motion due to shot noise in the common mode signal. Analogously, we define $S_{\phi_- \to \Phi_-}(f)^{1/2}$. Then,

$$\begin{aligned}\left(\frac{S_{\Phi_+ \to \Phi_-}(0)}{S_{\Phi_-}(0)}\right)^{\frac{1}{2}} &= \left(\frac{S_{\Phi_+}(0)}{S_{\Phi_-}(0)}\right)^{\frac{1}{2}} \frac{\partial v_3/\partial \Phi_+}{\partial v_3/\partial \Phi_-} \\ &\approx \left(\frac{P_S}{P_A}\right)^{\frac{1}{2}} \left(\frac{\eta_A}{\eta_S}\right)^{\frac{1}{2}} \frac{\partial v_3/\partial \Phi_+}{\partial v_1/\partial \Phi_+}\end{aligned} \qquad 2\text{-}49$$

$$\left(\frac{S_{\phi_-\to\Phi_-}(0)}{S_{\Phi_-}(0)}\right)^{\frac{1}{2}} = \left(\frac{S_{\phi_-}(0)}{S_{\Phi_-}(0)}\right)^{\frac{1}{2}} \frac{\partial\nu_3/\partial\phi_-}{\partial\nu_3/\partial\Phi_-} \approx \left(\frac{P_S}{P_A}\right)^{\frac{1}{2}} \left(\frac{\eta_A}{\eta_S}\right)^{\frac{1}{2}} \frac{\partial\nu_3/\partial\phi_-}{\partial\nu_2/\partial\phi_-} \qquad 2\text{-}50$$

2.6 Frequency Dependence of the Matrix of Discriminants

A recombined interferometer has substantially simpler frequency response than a recycled interferometer. The only parts of the 40-m interferometer with a characteristic response time in the gravitational wave band are the arm cavities which have typical energy storage times of 650 ms. The arm cavities act as integrators and are less sensitive to length changes at time scales shorter than their storage times. This is quantified in Eq. 2-39 which gives the transfer function between shaking an arm cavity end mirror and the ν_3 signal. Note that this equation reduces to Eq. 2-30 in the low frequency limit as expected.

Thus, the response of the differential mode signal rolls off as $1/f$ above the arm cavity pole,

$$f_c = \frac{\omega_c}{2\pi} = \frac{c}{4\pi l}\frac{1-r_3\,r_4}{r_3\,r_4} \qquad 2\text{-}51$$

This is the only frequency dependence to the signals from differential mode motion (the third row in Table 2-2) in the gravitational wave band as shown in Appendix C. The common mode signals (the first row in Table 2-2) which derive from the sum of the arm cavity lengths have the same frequency dependence. The Michelson signals (the second row in Table 2-2) have no frequency dependence from the effect calculated in Section 2.3, except at frequencies far beyond the gravitational wave band.[1] However, as is discussed in Sec-

tion 2.10, the Doppler shift of the light from the motion of the beam splitter is a frequency dependent effect which dominates the Michelson signals shown in Table 2-2 at frequencies much larger than 56 Hz.

2.7 Contrast Defect

The contrast defect is an important parameter in determining the interferometer performance, particularly the shot noise limited sensitivity. From our definition of contrast in Eq. 2-20, we can write the contrast defect,

$$1 - C = \frac{2P_D}{P_B + P_D} \approx \frac{2P_D}{P_B} \qquad 2\text{-}52$$

The contrast can be degraded by rms motion of the beam splitter, different visibilities in the two arms, alignment errors, wavefront distortion due to arm cavity mirror imperfections, and the asymmetry. Here we consider each of these effects in turn and use these results in Chapter 3 to set limits on the resulting contrast defect.

2.7.1 RMS Beam Splitter Motion

The contrast defect can be degraded by low frequency motion of the beam splitter if it is not sufficiently well controlled. With the arm cavities in perfect resonance, assuming negligible losses in all the optical elements, the power transmission from the laser input beam to the antisymmetric port is $\sin^2\left(\frac{\phi_-}{2}\right)$.[1] For small contrast defects, the contribution to contrast defect due the rms motion of the beam splitter is given by:

1. At frequencies above $c/(2\delta)$ (approximately 300 MHz) the different light travel times in the two arms of the Michelson due to the asymmetry will decrease the sensitivity to beam splitter motion, but this is clearly not of concern to us here.

$$\sin^2\left(\frac{\phi_-^{\rm rms}}{2}\right) \approx \frac{1}{2}(1-C) \qquad 2\text{-}53$$

In Section 2.8 a specification on $\phi_-^{\rm rms}$ is developed to assure tolerable contrast defect.

2.7.2 Different Arm Cavity Visibilities

If the arm cavities have different visibilities, the difference in the amount of light returning from the each arm will cause a contrast defect. The field returning from the in-line arm to the antisymmetric port is:[1]

$$E_5 = r_2\, t_2 \sqrt{1-V_1}\, E_0 \qquad 2\text{-}54$$

where V_1 is the visibility of the primary cavity in the limit of zero modulation[2] and E_0 is the field incident on the beam splitter. The field returning from the perpendicular arm is opposite in phase so that the field at the antisymmetric port is:

$$E_A = r_2\, t_2 (\sqrt{1-V_1} - \sqrt{1-V_2})\, E_0 \qquad 2\text{-}55$$

The contrast defect then is,[3]

---

1. The amplitude transmission of the carrier to the antisymmetric port is

$$t_A = \frac{1}{2}(e^{2ikl_1} - e^{2ikl_2})$$

$$= \frac{1}{2}\left\{ \exp\left[2ik\left(\bar{l} + \frac{\delta_- + \delta_-^{DC}}{2}\right)\right] - \exp\left[2ik\left(\bar{l} - \frac{\delta_- + \delta_-^{DC}}{2}\right)\right]\right\}$$

where $\bar{l} = \frac{1}{2}(l_1 + l_2)$, δ_-^{DC} is the optimal asymmetry and δ_- is the deviation from the optimum. We neglect the arbitrary phase factor, and note that $\exp(ik\delta_-^{DC}) = 1$, thus

$$t_A = \frac{1}{2}(e^{ik\delta_-} - e^{-ik\delta_-}) = i\sin k\delta_- = i\sin\left(\frac{\phi_-}{2}\right)$$

1. Using the notation of Section 2.4.
2. The phase modulation will decrease the measured arm cavity visibilities. Contrast defect is defined with respect to power in the carrier, so it is the zero modulation depth limit which is important here.

$$1 - C \approx 2\left|\frac{E_A}{E_0}\right|^2 = 2R_2T_2\left|\sqrt{1-V_1} - \sqrt{1-V_2}\right|^2 \qquad 2\text{-}56$$

2.7.3 Alignment Fluctuations

An angular tilt of the beam axis for the beam returning from one arm will cause imperfect interference at the beam splitter. This could be caused by orientation noise of the test masses or beam splitter. An angular tilt θ will cause the phase fronts of the interfering beams from the two arms to no longer be parallel and the spot positions to be shifted relative to each other. If we express the output mode of the cavity with the tilted beam axis in terms of the modes of the untilted, cavity we see that for small tilts we can approximate the output mode as being: [27]

$$E' \approx A\left[\mathrm{TEM}_{00} + i\frac{\pi\,\theta\,w_0}{\lambda}\,\mathrm{TEM}_{01}\right] \qquad 2\text{-}57$$

where A is the amplitude of the original TEM_{00} mode. This approximation is valid when $(2\pi\theta w_0)/\lambda \ll 1$, which says that the tilt angle is much less than the far-field divergence angle of the beam. Thus it is only the TEM_{01} piece which will not interfere destructively at the antisymmetric port. We define the fractional power of this non-interfering part due to the non-parallel phase fronts as

$$k_1 = \left(\frac{\theta\,\pi\,w_0}{\lambda}\right)^2 \qquad 2\text{-}58$$

The motion of the spot position also couples some of the light returning from the tilted arm into a higher order mode in the basis of the untilted arm. The fraction that does not

3. Note that the reflectivity and transmission of the beam splitter affects the resulting contrast defect but does not cause it. In fact, the greater the beam splitter unbalance between reflectivity and transmission, the smaller the contrast defect for a given arm cavity visibility mismatch.

interfere due to spot position movement is

$$k_2 = \left(\frac{l\,\theta}{w_0}\right)^2 \qquad 2\text{-}59$$

where l is the distance between the input test mass and the beam splitter. We assume that $l \ll R$, where R is the radius of curvature of the beam. The fraction of the light incident on the interferometer which returns to the beam splitter is $(1 - V)$ where V is the average arm cavity visibility. Thus the contrast defect induced by alignment errors in the beam returning from one arm is approximately,

$$1 - C \approx 2(1 - V)(k_1 + k_2) \qquad 2\text{-}60$$

2.7.4 Wavefront Distortion

The primary type of wavefront distortion that we are concerned with is due to surface deformations of the arm cavity mirrors with length scales the same as the beam spot diameter. As discussed in Appendix A, surface deformations on much smaller length scales scatter light out of the cavity mode and appear as loss on mirror reflection. The vertex test masses have λ/50 to λ/70 phase bumps in their centers with the FWHM of roughly the beam spot diameter.[1] To estimate the effect this has on the contrast defect, we shall calculate the contrast defect in the case where one arm cavity's vertex mirror has a surface that is deformed as shown in Figure 2-8.

The fields returning from the two arms at the beam splitter will have different waist sizes and thus will not interfere perfectly destructively at the antisymmetric port. If we express the output mode of the arm cavity with the surface deformation in terms of the

1. These phase bumps correspond to the regions of increased transmission mentioned in Section 2.2.

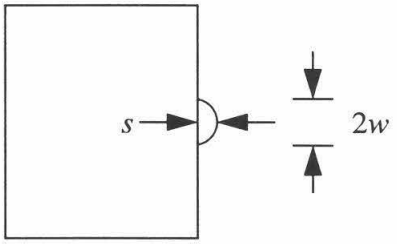

Figure 2-8: Vertex test mass with surface deformation. Sagitta is s over the beam spot diameter.

modes of the undeformed cavity, we find that for small differences in waist size we can approximate its output mode as being: [27]

$$E' \approx A\left[\mathrm{LG}_{00} + \left(\frac{w'}{w} - 1\right)\mathrm{LG}_{10}\right] \qquad 2\text{-}61$$

where LG_{00} and LG_{10} are the lowest order Laguerre-Gaussian radial modes[1]. This approximation is valid as long as $|w'/w - 1| \ll 1$. The LG_{10} term is the part of the light that will not interfere destructively at the anti-symmetric port. Thus the contrast defect due to the difference in waist sizes is

$$1 - C \approx 2(1 - V)\left(\frac{w'}{w} - 1\right)^2 \qquad 2\text{-}62$$

The sagitta due to the surface deformation on the vertex mirror makes this mirror have an effective radius of curvature of $w^2/(2s)$. The confocal parameter for an optical cavity is given by: [28]

1. It is most convenient to use polar coordinates and Laguerre-Gaussian modes when considering changes in waist size and position along the beam axis.

$$z_0^2 = \frac{l(-R_1 - l)(R_2 - l)(R_2 - R_1 - l)}{(R_2 - R_1 - 2l)^2} \qquad 2\text{-}63$$

where l is the length of the cavity, and R_1 and R_2 are the radii of curvature of the two mirrors (defined such that positive curvature is with the center of curvature to the left of the mirror). In this case, $R_1 = w^2/(2s)$ and $R_2 = R$, the radius of curvature of the end mirror. Thus,

$$z_0^2 = \frac{l(R - l)(-w^2 - 2sl)(2sR - w^2 - 2sl)}{(2sR - w^2 - 4sl)^2} \qquad 2\text{-}64$$

Expanding the numerator and neglecting all terms of order s^2 as negligible, we find

$$\begin{aligned} z_0^2 &\approx \frac{w^2 l(R - l)(-2sR + w^2 + 4sl)}{(2sR - w^2 - 4sl)^2} \\ &\approx \frac{w^2 l(R - l)}{w^2 + 4sl - 2sR} \end{aligned} \qquad 2\text{-}65$$

The waist size can be found simply from the confocal parameter, and substituted into Eq. 2-62 to find the contrast defect.

$$\begin{aligned} w' &= \left(\frac{\lambda z_0}{\pi}\right)^{\frac{1}{2}} \\ &\approx \left(\frac{\lambda w}{\pi}\right)^{\frac{1}{2}} \left(\frac{l(R - l)}{w^2 + 4sl - 2sR}\right)^{\frac{1}{4}} \end{aligned} \qquad 2\text{-}66$$

It is also useful to remember that the waist size of the undistorted arm is given by:

$$w = \left(\frac{\lambda}{\pi}\right)^{\frac{1}{2}} [l(R - l)]^{\frac{1}{4}} \qquad 2\text{-}67$$

2.7.5 Asymmetry

The asymmetry induces a contrast defect because the positions of the waists of the beams returning from the two arms are different. Thus at the beam splitter, the transverse size and curvature of the modes returning from the two arms are not identical. Expanding the modes of the farthest arm from the beam splitter in terms of the modes of the closest one, we can approximate that the light returning from it as: [27]

$$E' \approx A\left[\mathrm{LG}_{00} + \frac{\lambda\delta}{2\pi w_0^2}\mathrm{LG}_{10}\right] \qquad 2\text{-}68$$

which is valid in the limit that $(\lambda\delta)/(\pi w_0^2) \ll 1$. Thus the contrast defect due to the asymmetry is

$$1 - C \approx 2(1 - V)\left(\frac{\lambda\delta}{2\pi w_0^2}\right)^2 \qquad 2\text{-}69$$

2.8 Allowable Residual RMS Deviations

Before considering a control system for the recombined interferometer, we must derive reasonable specifications for the allowable rms deviations from resonance for the three degrees of freedom. [29] The interferometer output is generally not considered below 100 Hz, because it is dominated by seismic noise. However, low frequency, rms deviations can degrade the interferometer performance by causing other noise mechanisms to become important. The specifications given below are based on the need to maintain adequate power in the arm cavities, reject laser frequency or intensity noise, and keep the antisymmetric port dark.

2.8.1 Requirement to Maintain Power in the Arm Cavities

A deviation from resonance of the common mode arm cavity length will cause the power in the arm cavities to drop, decreasing the gravitational wave signal. We take the specification that the power in the arms must stay within 90% of maximum. From Eq. 2-6 we know that the power in a single arm cavity is

$$\begin{aligned} P_{arm} &\propto \left| \frac{1}{1 - r_3\, r_4\, e^{-i\Delta\phi}} \right|^2 \\ &\propto \frac{1}{1 + (r_3\, r_4)^2 - 2\, r_3\, r_4 \cos\Delta\phi} \end{aligned} \qquad 2\text{-}70$$

where $\Delta\phi$ is the phase deviation from resonance. Thus, to keep the arm cavity power to within a fraction, x, of its maximum power, we require that

$$\frac{1}{1 + (r_3\, r_4)^2 - 2\, r_3\, r_4 \cos\Delta\phi} > \frac{x}{1 + (r_3\, r_4)^2 - 2\, r_3\, r_4} \qquad 2\text{-}71$$

Thus,

$$\Delta\phi < \operatorname{acos}\left(\frac{1}{2}\left(1 - \frac{1}{x}\right)\frac{1 + (r_3\, r_4)^2}{r_3\, r_4} + \frac{1}{x} \right) \qquad 2\text{-}72$$

If we consider displacing both arm cavities from resonance equally, then the specification on the common mode length is

$$\Phi_+^{\mathrm{rms}} < 2\operatorname{acos}\left(\frac{1}{2}\left(1 - \frac{1}{x}\right)\frac{1 + (r_3\, r_4)^2}{r_3\, r_4} + \frac{1}{x} \right) \qquad 2\text{-}73$$

The specification for $x = 0.9$ then is $\Phi_+^{\mathrm{rms}} < 1.6\times10^{-4}$ or $\Delta_+^{\mathrm{rms}} < 7\times10^{-12}$ m.[1]

2.8.2 Requirement to Reject Laser Intensity Noise

The gravitational wave signal is proportional to the product of the laser power and the arm cavity length difference as can be seen from Eq. 2-30. Thus, low frequency deviations from resonance in Φ_- can enable laser intensity noise in the gravitational wave band to corrupt the gravitational wave signal. For example, the worst case relative intensity noise measured in the lab for the current laser (See Eq. 3-13) is

$$\frac{S_I^{1/2}}{I} \approx 4\times10^{-7}\ \mathrm{Hz}^{-1/2} \qquad 2\text{-}74$$

The contribution to the gravitational wave signal from intensity noise should be smaller than the contribution from the arm cavity difference. Thus,

$$\Phi_-^{\mathrm{rms}}\,\frac{S_I^{1/2}}{I}\,I < S_{\Phi_-}^{1/2}\,I \qquad 2\text{-}75$$

$$\Phi_-^{\mathrm{rms}} < \left(\frac{S_I^{1/2}}{I}\right)^{-1} S_{\Phi_-}^{1/2} \qquad 2\text{-}76$$

where $S_{\Phi_-}^{1/2}$ is the desired gravitational wave sensitivity. A target best sensitivity of 10^{-19} $\mathrm{m}/\sqrt{\mathrm{Hz}}$ would then correspond to $S_{\Phi_-}^{1/2} = 2.4\times10^{-12}/\sqrt{\mathrm{Hz}}$. Thus we require,

$$\Phi_-^{\mathrm{rms}} < 6.0\times10^{-6} \qquad 2\text{-}77$$

---

1. The simpler formula given in [29] is a very good approximation in this case and can be used instead whenever $\Delta\phi \ll 1$. Its general form (not shown in the reference) is:

$$\Phi_+^{\mathrm{rms}} < \sqrt{\frac{1}{x}-1}\;\frac{1-r_3\,r_4}{r_3\,r_4}$$

which corresponds to 2×10^{-13} m$/\sqrt{\text{Hz}}$.

2.8.3 Requirement to Reject Laser Frequency Noise

A recombined interferometer rejects frequency noise to some extent. If the arm cavities have the same storage time and are both on resonance, changing the laser frequency will cause the phase of the light reflected from both arms to change by the same amount. Thus the effect cancels and no signal can be seen upon recombination at the antisymmetric port. Various imperfections degrade this frequency noise rejection, although a recombined interferometer certainly provides more rejection than a Fabry-Perot interferometer. The apparent differential mode length change, $\Delta_{-}(f)$, is related to the change in frequency, $\delta\nu(f)$, as: [30][31]

$$\frac{\Delta_{-}(f)}{l} = \beta\frac{\delta\nu(f)}{\nu} \qquad 2\text{-}78$$

where l is the length of the arm cavities, ν is the laser frequency, and β is ratio of the difference of the arm cavity storage times to the average arm cavity storage time. For the 40-m interferometer $\beta \approx 0.2$, while the LIGO design calls for $\beta < 0.01$. If the arm cavity storage times are matched to 1%, M. Regehr has shown that to maintain this level of frequency noise rejection requires, $\Phi_{+}^{\text{rms}}\,\Phi_{-}^{\text{rms}} < 2\times10^{-6}$, [32] because deviations from arm cavity resonance can change the effective storage time of the cavity. However, for the current 20% static mismatch, the requirement is correspondingly less stringent,

$$\Phi_{+}^{\text{rms}}\,\Phi_{-}^{\text{rms}} < 4\times10^{-5} \qquad 2\text{-}79$$

Thus if Φ_{+}^{rms} satisfies Eq. 2-73 then $\Phi_{-}^{\text{rms}} < 0.29$. Φ_{-}^{rms} is more tightly constrained by

other considerations (Eq. 2-82), so the mismatch in arm cavity storage times with the current mirrors is the primary limitation to achieving good frequency noise rejection.

2.8.4 Requirements to Maintain the Dark Fringe

Deviations from resonance in ϕ_- or Φ_- degrade the dark fringe at the antisymmetric port and thereby increase the shot noise in the gravitational wave signal. As is discussed in Section 3.11, we typically achieve a contrast defect of 3%. We adopt the criteria that no more than an additional 0.2% of the incident power goes to the antisymmetric port (0.4% contrast defect) due to motion of the beam splitter and similarly for arm cavity differential motion.[1] From Eq. 2-53 we require,

$$\sin^2\left(\frac{\phi_-^{rms}}{2}\right) < 0.002 \qquad 2\text{-}80$$

$$\phi_-^{rms} < 8.9\times10^{-2} \qquad 2\text{-}81$$

equivalent to an rms Michelson near mirror difference $< 4\times10^{-9}$ m.

To derive the analogous specification for the arm cavity length difference, we note that the phase of the light returning to the beam splitter changes much faster for changes in Φ_- than for changes in ϕ_-. The ratio of the two rates of change of phase is exactly the phase gain, from Eq. 2-15. For the 40 m arm cavities on resonance, $N' = 30{,}000$. Thus the specification for Φ_- must be tighter by this factor, so that

$$\Phi_-^{rms} < 2.9\times10^{-6} \qquad 2\text{-}82$$

1. A 1% contrast defect must ultimately be achieved for desired interferometer performance. This criteria was set with achieving this goal in mind.

This corresponds to an rms arm cavity length difference of 1×10^{-13} m.

We adopt as our specification the strictest criteria for each of the three degrees of freedom. The final specifications are summarized in Table 2-3.

Table 2-3: Specifications for RMS Deviations

Phase	Distance, m	Explanation
$\Phi_+ < 1.6\times10^{-4}$	$\Delta_+ < 7\times10^{-12}$	arm cavity power
$\phi_- < 8.9\times10^{-2}$	$\delta_- < 4\times10^{-9}$	maintain dark fringe
$\Phi_- < 2.9\times10^{-6}$	$\Delta_- < 1\times10^{-13}$	maintain dark fringe

2.9 Effects of Demodulation Phase Error

The symmetric port photodiode provides error signals for two of the degrees of freedom. An error in the phase of the local oscillator signal used to demodulate the symmetric port signal and generate v_2 will allow some of the v_1 signal to leak into the beam splitter control loop. This can be a problem because v_2 is only weakly sensitive to beam splitter motion. The v_1 signal predominantly depends only on the common mode length and this extra dependence on this degree of freedom in the beam splitter servo could degrade its performance. The amount of phase error that can be tolerated depends on the degree to which the frequency stability servo can suppress error in the arm cavity common mode length.

To analyze the effect of mixer phase error, we model the beam splitter servo as a single input, single output (SISO) servo with uncorrelated sensor noise due to the common

mode error, as shown in Figure 2-9.[1] $K(\beta)$ is the coefficient which determines how much

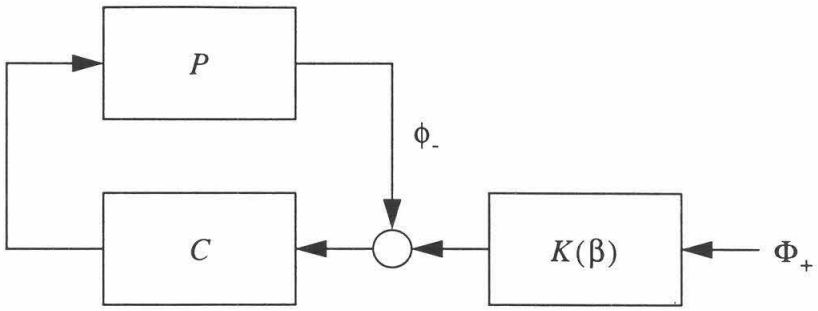

Figure 2-9: Model of beam splitter servo: β is the mixer phase error, C represents the electronic controller and P is the optical response of the plant.

uncorrelated sensor noise feeds through from the common mode, in units of the beam splitter phase. It is given by,

$$K(\beta) = \frac{\partial v_1 / \partial \Phi_+}{\partial v_2 / \partial \phi_-} \sin\beta \qquad 2\text{-}83$$

The transfer function from Φ_+ to ϕ_- is

$$\mathrm{TF}(\Phi_+ \rightarrow \phi_-) = \frac{CP}{1 - CP} K(\beta) \qquad 2\text{-}84$$

There are two ways that this common mode to beam splitter coupling can degrade the gravitational wave sensitivity. The first is that large in-band fluctuations of the beam splitter are sensed by the v_3 signal and can be confused with differential motion of the arm cavities. Secondly, low frequency variations in the beam splitter position can degrade the

1. A more theoretically complete treatment of this problem would be to model the full interferometer as a multi-input, multi-output (MIMO) system and consider the performance costs associated with varying the common mode to beam splitter cross coupling because of the mixer phase error. However, since the coupling from beam splitter motion to the common mode servo is very small, we can safely neglect it and the model we use here is a good approximation.

contrast so that the shot noise of the gravitational wave signal is increased. In both cases we will specify the maximum tolerable mixer phase error as that which gives a 3 dB degradation in the gravitational wave sensitivity.

2.9.1 Effect at Signal Frequencies

In the gravitational wave band $CP < 1$,[1] and thus

$$\left|\frac{CP}{1-CP}\right| < \frac{1}{2} \qquad f > 100 \text{ Hz} \tag{2-85}$$

The error in ϕ_- from cross coupling of Φ_+ due to mixer phase error is then

$$e(\phi_-) < \frac{1}{2}\frac{\partial v_1/\partial \Phi_+}{\partial v_2/\partial \phi_-}\,\beta\,\Phi_+ \tag{2-86}$$

where we have approximate for small phase errors, $\sin\beta \approx \beta$. Because v_3 depends weakly on ϕ_-, this excess beam splitter motion will produce an error in the gravitational wave signal equivalent to Φ_- of

$$\begin{aligned} e(\Phi_-) &< \frac{1}{2}\frac{\partial v_1/\partial \Phi_+}{\partial v_2/\partial \phi_-}\,\beta\,\Phi_+\,\frac{\partial v_3/\partial \phi_-}{\partial v_3/\partial \Phi_-} \\ &< \frac{1}{2}\frac{\partial v_1/\partial \Phi_+}{\partial v_3/\partial \Phi_-}\,\beta\,\Phi_+ \end{aligned} \tag{2-87}$$

For a 3 dB degradation in gravitational wave sensitivity, this error would equal the differential arm cavity error due to other sources. In this case,

$$\frac{1}{2}\frac{\partial v_1/\partial \Phi_+}{\partial v_3/\partial \Phi_-}\,\beta\,\Phi_+ = \Phi_- \tag{2-88}$$

---

1. Why this is required is discussed in Appendix F.

The gain of the common mode servo is larger than the differential mode servo at all frequencies and the disturbance spectra for the two are basically identical. Thus, we can safely expect that at any given frequency $\Phi_+ \approx \Phi_-$.

$$\begin{aligned} \beta &< 2\,\frac{\partial v_3/\partial \Phi_-}{\partial v_1/\partial \Phi_+} \\ &< 15^\circ \end{aligned} \qquad \text{2-89}$$

2.9.2 Effect on Contrast Defect

Common mode feedthrough to the beam splitter position at frequencies below 100 Hz can increase ϕ_-^{rms} and lead to poor control of the contrast defect. A contrast defect of 5% will degrade the shot noise limited sensitivity by 3 dB over that for a 1% contrast defect. We take as our specification then that mixer phase error must not account for more than 5% contrast defect. From Eq. 2-53,

$$\sin^2\left(\frac{\phi_-^{rms}}{2}\right) < 0.025 \qquad \text{2-90}$$

$$\phi_-^{rms} < 0.318 \qquad \text{2-91}$$

At the low frequencies we are concerned with $|CP| \gg 1$, and so

$$\left|\frac{CP}{1-CP}\right| \approx 1 \qquad f \ll 100 \text{ Hz} \qquad \text{2-92}$$

Thus, we require that the rms error in ϕ_- from Φ_+ satisfies,

$$e(\phi_-^{rms}) = \frac{\partial v_1/\partial \Phi_+}{\partial v_2/\partial \phi_-}\,\beta\,\Phi_+^{rms} < 0.318 \qquad \text{2-93}$$

$$\beta < \frac{0.318}{\Phi_+^{rms}} \frac{\partial \nu_2 / \partial \phi_-}{\partial \nu_1 / \partial \Phi_+} \qquad 2\text{-}94$$

Using the specification on Φ_+^{rms} from Table 2-3, we see that this corresponds to

$$\beta < 11° \qquad 2\text{-}95$$

This provides a more stringent requirement on the mixer phase error so we will adopt it as a criterion.

2.10 Sensitivity to Beam Splitter Motion

The sensitivity to beam splitter motion in the gravitational wave signal is increased relative to the Fabry-Perot interferometer. Both the recombined and Fabry-Perot interferometers are sensitive to the Doppler shift of the light reflected from the beam splitter. But the recombined interferometer has an additional sensitivity due to the fact that moving the beam splitter will disturb the destructive interference at the antisymmetric port. The relative sizes of these two mechanisms for beam splitter motion affecting ν_3 are discussed below.

In a recombined interferometer, when ϕ_- deviates from zero, the extra carrier light at the antisymmetric port beats against the sidebands and produces a signal at the mixer output. The ratio of sensitivity to Φ_- and ϕ_- in the gravitational wave signal is (combining Eq. 2-29, Eq. 2-30, Eq. 2-11, and Eq. 2-14)

$$\left|\frac{\frac{\partial v_3}{\partial \Phi_-}}{\frac{\partial v_3}{\partial \phi_-}}\right| = \frac{|r_{arm}'|}{r_{arm}} = \frac{\frac{T_3\ r_4}{(1-r_3\ r_4)^2}}{\frac{r_3-(1-L_3)\ r_4}{1-r_3\ r_4}}$$
$$= \frac{t_3^2\ r_4}{[r_3 - r_4\ (1-L_3)](1-r_3\ r_4)} \qquad 2\text{-}96$$
$$= N'|_{\phi=0}$$

This is the phase gain of the arm cavities. For the 40m interferometer $N' \approx 30,000$. This mechanism for sensitivity to beam splitter motion is obviously absent in the Fabry-Perot interferometer.

In the other mechanism, the frequency of the light reflected off the beam splitter is Doppler shifted by its motion. This frequency shift is converted to a large phase shift by the arm cavity which is then detected as a gravitational wave signal. In both the recombined and Fabry-Perot interferometers, only one arm cavity sees light that has been Doppler shifted by the beam splitter. The small additional bit of phase change that is induced by the Doppler shift of the light returning from the in-line arm upon recombination is negligible compared to the effect of the perpendicular arm cavity. Thus the sensitivity to the Doppler shift mechanism should be the same for both interferometer configurations. Note that this mechanism for sensitivity to beam splitter motion is not included in the discriminant matrix.

To compare the importance of the Doppler shift mechanism, we calculate

$$\frac{\partial v_3}{\partial \phi_-} = \frac{\partial v_3}{\partial f}\frac{\partial f}{\partial \phi_-} \qquad 2\text{-}97$$

Now, $\partial f / \partial \phi_-$ can be derived from the Doppler shift formula:

$$f = f_0\left(1 - \frac{v}{c}\cos\theta\right) \qquad 2\text{-}98$$

where f is the frequency of the light reflected off the moving beam splitter, $\theta = 45°$ is the angle of incidence of the laser light, and v is the velocity of the beam splitter. Decomposing the motion of the beam splitter into its Fourier frequency components and using the standard exponential notation, we can write

$$\delta_- = \delta_{-0}\, e^{i\omega t} \qquad 2\text{-}99$$

$$\begin{aligned} v &= i\omega\delta_{-0}\, e^{i\omega t} \\ &= i\omega\delta_- \\ &= i\omega\frac{\lambda}{4\pi}\phi_- \end{aligned} \qquad 2\text{-}100$$

Thus,

$$f = f_0\left(1 - \frac{i\omega\lambda\phi_-}{4\pi\sqrt{2}\,c}\right) \qquad 2\text{-}101$$

and

$$\frac{\partial f}{\partial \phi_-} = -i\frac{\omega}{4\pi\sqrt{2}} \qquad 2\text{-}102$$

To calculate $\partial v_3/\partial f$ we expand in terms of the three degrees of freedom and find,

$$\frac{\partial v_3}{\partial f} = \frac{\partial v_3}{\partial \Phi_+}\frac{\partial \Phi_+}{\partial f} + \frac{\partial v_3}{\partial \Phi_-}\frac{\partial \Phi_-}{\partial f} + \frac{\partial v_3}{\partial \phi_-}\frac{\partial \phi_-}{\partial f} \qquad 2\text{-}103$$

where f is the frequency of the light going into the secondary arm only which is Doppler shifted by the beam splitter.[1] Changing the frequency of the light going into one arm

effects the common and differential mode equally so that $\partial\Phi_+/\partial f = \partial\Phi_-/\partial f$. From the matrix of discriminants, we can then see that the second term in Eq. 2-103 will be the dominant term by at least an order of magnitude and so we neglect the others.

$$\Phi_- = \frac{4\pi}{c}(L_1 f_0 - L_2 f) \qquad 2\text{-}104$$

$$\frac{\partial\Phi_-}{\partial f} = -\frac{4\pi}{c} L_2 \qquad 2\text{-}105$$

Therefore, we have

$$\frac{\partial v_3}{\partial\phi_-} = \frac{\partial v_3}{\partial\Phi_-}\frac{\partial\Phi_-}{\partial f}\frac{\partial f}{\partial\phi_-} \qquad 2\text{-}106$$

and we can write, for the Doppler shift mechanism,

$$\frac{\dfrac{\partial v_3}{\partial\Phi_-}}{\dfrac{\partial v_3}{\partial\phi_-}} = \frac{1}{\dfrac{4\pi}{c} L_2 \left(i\dfrac{\omega}{4\pi\sqrt{2}} \right)} \qquad 2\text{-}107$$

$$\left| \frac{\dfrac{\partial v_3}{\partial\Phi_-}}{\dfrac{\partial v_3}{\partial\phi_-}} \right| = \frac{\sqrt{2}\, c}{\omega\, L_2} \qquad 2\text{-}108$$

Thus we can see the size of the signal due to the Doppler shift is growing in frequency and

---

1. Please note that

$$\frac{\partial f}{\partial\phi_-} \neq \left(\frac{\partial\phi_-}{\partial f}\right)^{-1}$$

$\partial f/\partial\phi_-$ in Eq. 2-102 is the change due to the Doppler shift in the frequency of the light reflected off the beam splitter with respect to a change in the Michelson phase at a particular frequency. $\partial\phi_-/\partial f$ in Eq. 2-103 on the other hand, is the change in the Michelson phase with respect to a change in the frequency of the light going to the second arm.

is 90° out of phase with the signal due to the imperfect interference at the dark port.[1] At some frequency the two signals will become equal in magnitude. For 40 m long arm cavities, this frequency is

$$f_{Dop} = \frac{\sqrt{2}\ c}{2\pi\ N'\ l_2} = 56\ \text{Hz} \qquad \text{2-109}$$

Because the Doppler shift and imperfect interference signals are 90° out of phase, they will add in quadrature in contributing a noise term to the gravitational wave signal. Thus, at 56 Hz the recombined interferometer will have a contribution to the gravitational wave signal due to beam splitter motion which is $\sqrt{2}$ greater than the Fabry-Perot interferometer. At frequencies well above 56 Hz, the Doppler shift mechanism will dominate and the response of both configurations is essentially the same.

1. This is to be expected as one signal derives from the position of the beam splitter and the other from its velocity.

Chapter 3: Recombination Experiment

The primary goals of the experimental program with the recombined interferometer were to demonstrate and study lock acquisition in a suspended interferometer using the asymmetry signal extraction scheme, to understand the noise sources limiting interferometer performance, to provide further validation of the asymmetry signal extraction scheme model, and to give information useful for modification of the 40-m interferometer to a recycled configuration. All of these goals, with the exception of a complete characterization of the noise, were met and are discussed below. Because the noise limiting the gravitational wave signal is not fully understood, complete descriptions of the noise sources eliminated as candidates are given.

A block diagram of the servo loops used to control the longitudinal degrees of freedom of the recombined interferometer is shown in Figure 3-1. A complete description of this diagram and the design of the various servo loops can be found in Appendix E.

The extra sensitivity to beam splitter motion in the gravitational wave signal (See Section 2.10.) makes understanding the noise sources affecting the beam splitter position more critical. The performance of the beam splitter servo is discussed and found to be adequate. Several sources of displacement noise affecting the test masses have been well studied in the Fabry-Perot interferometer and have been shown not to limit the gravitational wave signal. [33][34] Since these sources of noise are not increased in a recombined configuration, we shall not consider them here.

One expects that the sensitivity to various sensing noise sources could change in the recombined configuration. Thus, careful attention is paid to shot noise, intensity noise and frequency noise of the light. The investigation of these noise sources was complicated by

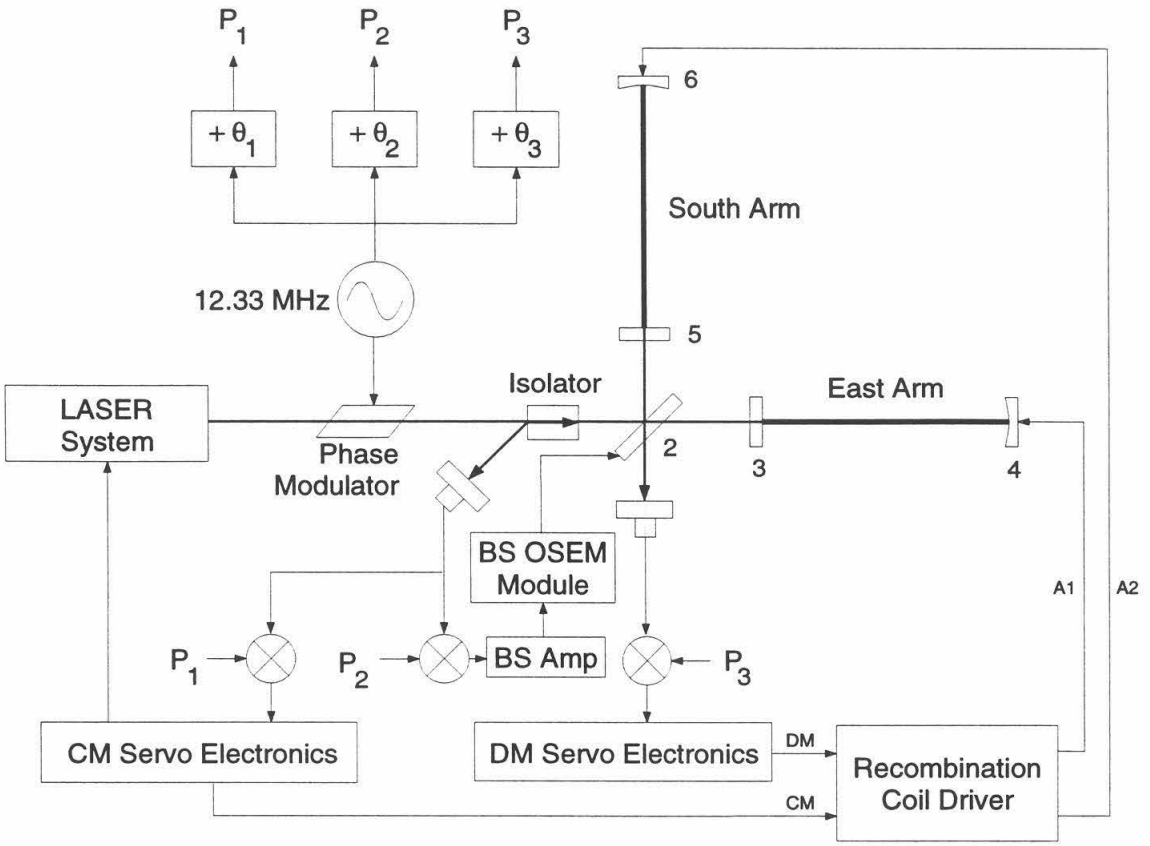

Figure 3-1: Block diagram of the servos used to control the longitudinal degrees of freedom in the recombined 40-m interferometer.

the fact that laser system was replaced during the recombination task. When the gas tube in the original laser reached the end of its service life, it was decided to replace the entire laser system with another system with improved automation and operator control features.[1] The intensity noise of the replacement laser system was later shown to be higher than the original system. With the original laser system the interferometer noise was not limited by shot noise, intensity noise or frequency noise. With the replacement laser sys-

1. The laser used as part of the original laser system was an Innova 100 manufactured by Coherent, while the later version used a Spectra Physics model 2040E. The performance of both of these lasers operating alone was reasonably equivalent.

tem, the interferometer was limited by intensity noise above 500 Hz.

3.1 Lock Acquisition

The largest concern before the operation of the recombined interferometer was the undefined mechanism for acquiring lock. When the interferometer is in a stable situation, where both of its arm cavities are being held very close to resonance by the common and differential mode servos and the beam splitter is being held such that there is a dark fringe at the antisymmetric port, we say the interferometer is "in lock." The states the interferometer passes through in going from all the optics swinging freely to being in lock are part of the lock acquisition process. The fundamental problem is that the Fabry-Perot cavities using RF reflection locking techniques only provide a signal which is linearly proportional to their length for very small deviations from resonance. In a suspended interferometer where the mirrors are swinging through many fringes at the pendulum resonance frequency, the signal used to adjust these mirror positions will often be zero or of the wrong sign.

Time domain models which include the nonlinear dynamics of the lock acquisition process have been developed by others in parallel with this work. The understanding gained from the model of a single Fabry-Perot cavity was complete enough, in fact, for a computer controller to decrease the lock acquisition time of a single cavity by an order of magnitude. [35] The model for a recombined or more complicated interferometer, however, was not far enough along to be useful in predicting the lock acquisition behavior of the 40-m interferometer, prior to commencement of this experimental program.

The lock acquisition sequence observed was that the beam splitter acquired lock first,

because of its very broad range of linear operation, and held the antisymmetric port on a dark fringe. The common mode servo would then acquire lock and hold one of the arm cavities on resonance. Because this servo has a very high bandwidth, we expect it to acquire before the differential mode. With one arm cavity on resonance and one off resonance, the signal read by the common mode servo was almost entirely due to the arm on resonance. The arm that was swinging freely would pass through a resonant condition several times a second. While passing through resonance the out of lock arm would contribute to the common mode signal comparably to the in lock arm. It was a pleasant surprise that this typically did not disrupt the resonance of the arm in lock. When the relative velocity of the test masses in the out of lock arm was low enough as this arm passed through resonance, the differential mode servo was able to lock onto that fringe. This was in fact very similar to the situation we had with the Fabry-Perot interferometer where one arm would acquire lock easily and we would have to wait an average of several minutes for the feedback to the mirror positions of the other arm to catch and hold it on a resonance condition.

Although it would seem that both arms should have been selected with equal probability to be the initial arm in lock, in fact it was much more commonly the south arm that locked first. This is most likely due to the fact that the beam splitter is unbalanced such that 20% more light goes to the south arm than the east arm, and that the south arm has higher optical gain because its losses are lower. This may also help explain why the east arm passing through resonance would not disturb the lock of the south arm. In the cases where the east arm did acquire lock first, the south arm was often successful in "stealing" the common mode lock when it later passed through resonance.

3.2 Beam Splitter Signal Sign Reversal

A problem with the lock acquisition sequence described above is that the signal to control the beam splitter can reverse sign in going from the case of one arm and the beam splitter in lock to the entire interferometer in lock. This is because the overcoupled Fabry-Perot arm cavities switch the phase of the carrier light reflected from them by 180° in going from out of lock to in lock. In the low modulation depth limit where we can neglect the second order sidebands, we can use Eq. 2-28:

$$\frac{\partial v_2}{\partial \phi_-} = -E_l^2 \, J_0(\Gamma) \, J_1(\Gamma) \sin\alpha \; r_{\text{arm}} \qquad 3\text{-}1$$

Here we can see that the sign of the beam splitter error signal will reverse when the reflectivity of the arm cavities for the carrier (r_{arm}) reverses. To consider the case of one arm in lock, see Figure 3-2. From the diagram we can see that the carrier field at the symmetric port has the same phase with either one or no arms in lock, but reverses when both arms are in lock. Thus in the low modulation depth limit, we expect that if the phase of the beam splitter error signal is originally adjusted to hold the antisymmetric port on a dark fringe with neither arm in lock, then it will of the wrong sign once both arms acquire lock.

In practice this was not observed originally because the mode matching into the arm cavities was poor. The non-mode matched light is reflected directly from the vertex mirrors and does not get phase reversed when the cavity goes into resonance. The non-mode matched fraction of the light was large enough that the phase of all the carrier light reflected from the cavities did not reverse its sign. After improving the mode matching, however, the interferometer was unable to acquire lock at low modulation depth for this

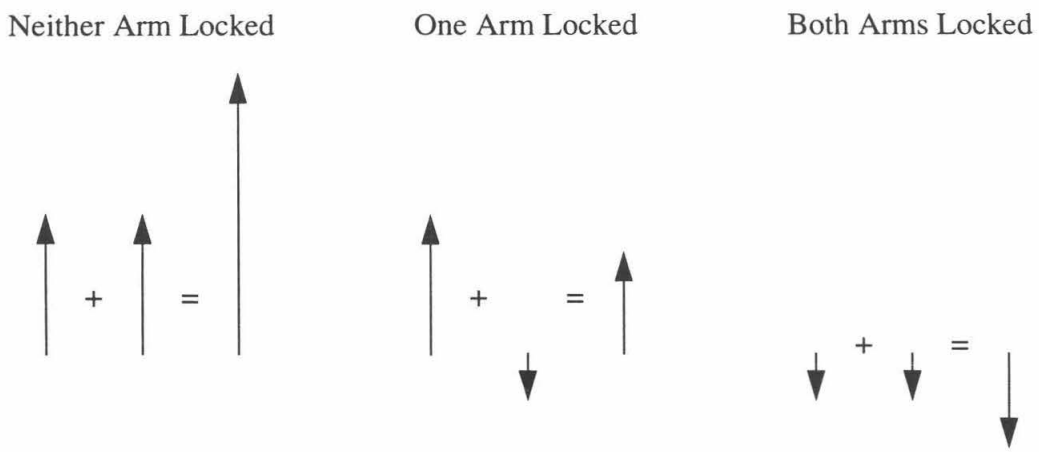

Figure 3-2: Phasor diagrams of light returning to the symmetric port. The two fields shown adding are the reflected carrier fields from the arm cavities and their sum is the field at the symmetric port.

reason.

Two schemes for solving this problem were explored. The most straightforward approach is to trigger a sign reversal of the beam splitter feedback signal when both arms go into resonance. After being careful to null out all the offsets in the beam splitter servo, this method was successful. Another method is to increase the modulation depth well above the optimal depth for shot noise limited sensitivity in the gravitational wave signal. As can be seen from Table 3-1, increasing the modulation depth changed the sign of the beam splitter error signal (v_2) and increased its sensitivity to beam splitter motion without changing the other matrix elements. This is due to a beating between the first and second order sidebands, neither of which experience a phase reversal when the arm cavities go into resonance. In this case the beam splitter has the same sign for its error signal with neither arm in lock and both arms in lock. The method of increasing the modulation depth was the one adopted for most of the tests described here as it worked much more reliably and eliminated some of the noise problems we saw because the sensitivity to beam splitter

motion was so small. Because shot noise was not limiting our noise spectrum, running at a non-optimal modulation depth was not a problem.

Table 3-1: Extracted Signal Sensitivities at Different Γ

	$\partial\nu_1$		$\partial\nu_2$		$\partial\nu_3$	
Γ	0.7	1.49	0.7	1.49	0.7	1.49
$\partial\Phi_+$	−7.8	−7.8	0	0	-2.2×10^{-1}	-2.2×10^{-1}
$\partial\phi_-$	2.3×10^{-4}	2.3×10^{-4}	-1.3×10^{-5}	1.9×10^{-4}	-1.0×10^{-5}	-1.9×10^{-4}
$\partial\Phi_-$	2.5	2.5	-2.5×10^{-9}	1.6×10^{-8}	1.0	1.0

3.3 Mixer Phase Settings

The demodulation phases of the three mixers must be set correctly for proper operation of the interferometer. As discussed in Section 2.9, the phase used to demodulate the beam splitter signal is particularly critical. The phases used to demodulate the common mode and differential mode signals are not as critical and mainly lower the gain of each servo loop if they are detuned from their optimal settings.

Previous experience with the asymmetry signal extraction scheme on a table top was that the gains and demodulation phases of the servos were very difficult to set accurately enough to acquire lock, but once set properly, lock acquisition was fairly robust. [36] For the recombined 40-m interferometer, the gains of the common mode and differential mode were much easier to set correctly by scaling appropriately from our experience with the Fabry-Perot configuration. The beam splitter gain was set by trial and error, but with the end test masses misaligned, the beam splitter servo would function independently of the

other servos which made its adjustment fairly straightforward.

Two methods were used to set the demodulation phases and they gave very similar results. One method was to inject a monochromatic signal into a test input of the common or differential mode and observe the size of the resulting peak in the feedback signal. Adjusting the demodulation to minimize this peak effectively maximizes the gain of this servo as desired for optimal demodulation phase. The common mode mixer phase was adjusted first with one arm misaligned and the other held on resonance by the common mode servo. The differential mode mixer phase was then set with both arms in lock. The mixer phase of the beam splitter was set by injecting a monochromatic signal into the common mode servo and minimizing the height of the resulting peak in the beam splitter feedback. In this way the beam splitter phase is set to minimize common mode to beam splitter feedthrough.

Another method suggested by S. Whitcomb gave very similar mixer phase settings but had the advantage that it did not require any of the servos to be operational. The end masses were both misaligned so that only a Michelson interferometer was formed with the beam splitter and the vertex test masses. A monochromatic signal was used to drive the position of the beam splitter at 200 Hz.[1] The demodulation phase for the common mode was adjusted to minimize the height of the resulting peak while the height of the differential mode was adjusted to maximize it. The beam splitter demodulation phase was set 90° away from the phase used for the common mode.

Both of these methods suffered from the fact that the maxima and minima in the heights of the peaks were rather broad and slowly varying with the demodulation phase.

1. Any frequency where it is easy to excite the beam splitter well above the ambient seismic motion would work.

The beam splitter mixer phase was adjusted most frequently and the optimal setting was found to drift by 10° or more over week time scales. These drifts are primarily electronic, and their stability will be improved in future designs now that this is understood as an important effect.

3.4 Calibration

The differential mode feedback voltage must be calibrated in units of actual displacement to be useful. The procedure for doing this is described below and compared with that used with the Fabry-Perot interferometer.

The idea is to drive the east end mass of the interferometer a known amount at a specific frequency such that the resulting signal at that frequency appears in the interferometer output far above the ambient background due to other noise sources. By dividing the peak height in the interferometer output by the known amount of drive at that frequency and then sweeping the frequency of measurement downwards in discrete steps, a transfer function from displacement of the east end mass to the interferometer output can be measured.

The east end mass is used because the drive voltage to displacement conversion is best known for this mass. There is a history of careful measurements of the conversion for the east end mass because it provided an unambiguous way to do this calibration with the Fabry-Perot interferometer. The east end mass position in that case was not actively controlled by the servos at frequencies of interest, and thus this was a straightforward method of measuring the interferometer response to a known differential motion of its arms. Of course driving the east end mass alone also provides an equal common mode motion, but

this was completely decoupled from the gravitational wave readout in the Fabry-Perot configuration.

In a recombined interferometer there is the concern that because of the relatively strong common mode to differential mode coupling, the response at the interferometer output to purely differential mode motion would be different from the combination of differential and common mode motion used in our calibration procedure. To alleviate this concern, the calibration procedure was also performed by driving both end masses differentially. The drive voltage to each end mass was the same as the drive used when calibrating with the east end mass alone. Because both masses were used and the conversion between drive voltage and displacement for the south end mass is close to the value for the east end mass, we expect the interferometer response to be increased by approximately a factor of two. In fact, as shown in Figure 3-3, the transfer functions for both arms driven differentially versus driving only the east arm differed by 7 dB.[1]

All of these measurements depend on knowing the conversion from drive voltage to the test mass and displacement of the test mass. The standard method of measuring this is to drive the test mass at some frequency around 10 Hz such that the motion induced at this frequency is far above the ambient motion at this frequency. The motion induced must also be large enough to move the test mass through more than one arm cavity resonance. By monitoring the reflected light from the arm cavity, the times when it passes through resonance can be seen. The difference between adjacent resonant lengths is one-half of the laser wavelength. By measuring the differences in the drive voltages on a storage scope between successive resonances and averaging over many such measurements, one can

1. This is within the uncertainty present because of the slightly different voltage to displacement conversion for the two end test masses.

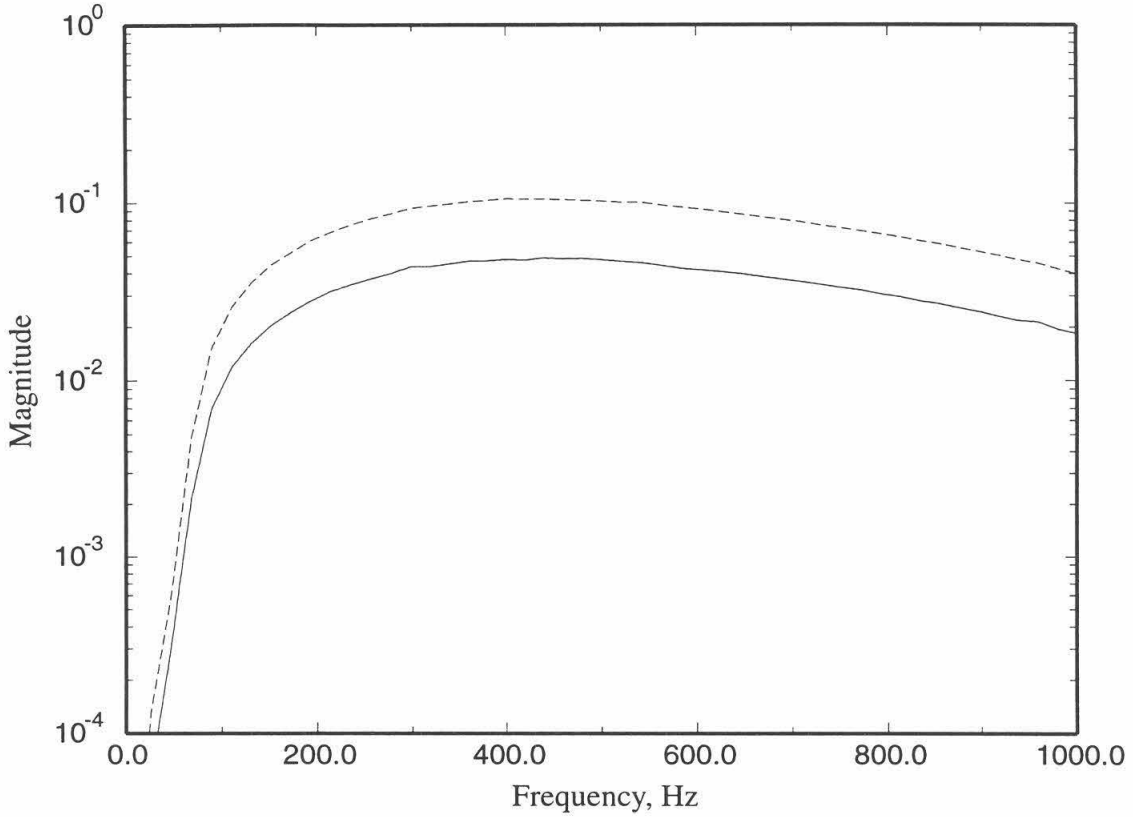

Figure 3-3: Transfer function from driving the east end test mass (solid) or both end masses differentially (dotted) to the interferometer output.

determine the voltage necessary to push the test mass $\lambda/2$ at the drive frequency.[1] Because the test mass is suspended as a pendulum, this calibration rolls off as f^{-2}. The voltage to displacement calibration used here is[2]

$$x(f) = \left(3.14\times10^{-8}\ \frac{\text{m Hz}^2}{\text{V}}\right)\frac{V_{\text{source}}}{f^2} \qquad 3\text{-}2$$

1. An alternate method used in the Fabry-Perot configuration was to measure the displacement induced by a given drive voltage using an auxiliary Michelson interferometer. Both methods gave comparable results.
2. The uncertainty in this calibration is approximately 20%.

where V_{source} is the source voltage fed into the calibration input for the east end mass, as read on an HP 3563A spectrum analyzer used to do the calibrations.

3.5 Shot Noise in the Gravitational Wave Signal

The displacement noise in the differential degree of freedom equivalent to shot noise in the gravitational wave signal is derived in Section 2.4. It is derived by holding three of the masses fixed and moving only one end mass, which is equivalent to differential mode motion. The reflectivities and transmissions can be obtained from in-situ measurements, summarized on Table 2-1.[1]

We do not, however, directly measure the fields in the lab. What we instead measure is the DC voltage obtained by passing the antisymmetric port photocurrent through a known resistor.[2] We record the minimum voltage when the interferometer is in lock (V_{min}) and the maximum voltage observed when the arms cavities are out of lock and the beam splitter is allowed to swing freely (V_{max}). Additionally we must make an independent measurement of the modulation depth (Γ). To include the effect of light that is not mode matched properly into the arm cavities, we also measure the mode matching fraction, M. The fields are then found from

$$E_2 = \sqrt{\frac{V_{max}}{Re}}\, J_0(\Gamma) \qquad 3\text{-}3$$

$$E_+ = \sqrt{\frac{V_{max}}{Re}}\, J_1(\Gamma)\sin\alpha \qquad 3\text{-}4$$

1. Note that we take the case of the worst arm in terms of transmission and losses.
2. Note that for both simplifying the expressions in Section 2.4, and for comparison with experiment, it is convenient to write the fields in units of $\sqrt{\text{photoelectrons/second}}$ as we have done.

$$E_{DC} = \sqrt{\frac{V_{min}}{Re} - 2E_+^2} \qquad 3\text{-}5$$

where R is the resistance in series with the photodiode and e is the charge of the electron in Coulombs.

The mode matching fraction affects the shot noise limit because only the light that could mode match into the cavities produces the signal. Mode matching does not affect the noise except as already accounted for in E_{DC}. Thus the effective magnitude of E_2 and E_+ in the denominator of the shot noise expression (Eq. 2-46) are reduced by $\sqrt{M}$. So,

$$\overline{S_\Delta}(f)^{1/2} = \frac{\sqrt{3E_+^{\,2} + E_{DC}^{\,2}}}{2kM|E_2|E_+} \frac{(1 - r_3 r_4)^2}{T_3 r_4} \sqrt{1 + \left(\frac{2\pi f}{\omega_c}\right)^2} \qquad 3\text{-}6$$

Table 3-2: Parameters Used in Shot Noise Prediction

Name	Value
V_{max}	1.1 V
V_{min}	20 mV
R	50 Ω
Γ	0.705
M	0.77
α	0.132
T_3	280 ppm
r_3	0.999805
r_4	0.999938

The parameters used in the shot noise calculation are collected in Table 3-2. The resulting curve is shown in Figure 3-4. This is compared to an empirical measurement of

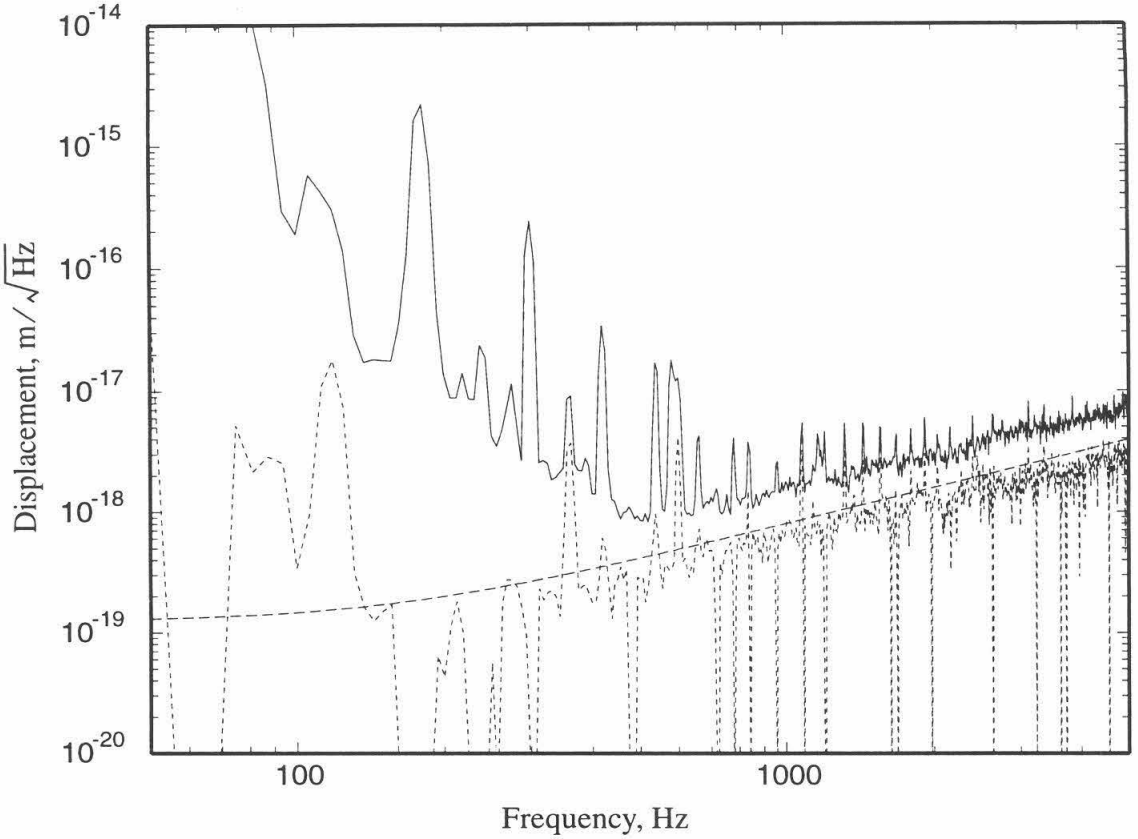

Figure 3-4: Calculated shot noise contribution to interferometer displacement spectrum (dashed), with empirical measurement of shot noise contribution (dotted) and interferometer displacement spectrum taken shortly before on January 10, 1996 (solid).

the shot noise contribution to the gravitational wave signal (discussed below) and to the interferometer displacement spectrum taken at the time these measurements were done. The empirical measurement of the shot noise contribution agrees with the calculation to within the uncertainties of the parameters in the calculation and in the calibration. Note that the interferometer was not limited by shot noise at any frequency. This was confirmed by attenuating the light leaving the antisymmetric port by 37.5% and adding incandescent

light onto the photodiode to raise the incident power by a factor of 3.2. We would expect a 7 dB increase in the interferometer displacement spectrum if it were limited by shot noise, but the largest increase seen anywhere in this frequency band was 4 dB.

The empirical measurement of the shot noise contribution to the gravitational wave signal was accomplished by blocking the laser light and shining incandescent light on the antisymmetric photodiode such that the photocurrent was the same as in normal operation. The gravitational wave readout can then be calibrated normally, once the effect of the loop gain is properly taken into account. With the interferometer in lock, this shot noise signal is suppressed by the differential mode loop gain.

The differential mode servo loop with the places where shot noise, dark noise of the photodiode and readout noise would sum in is shown in Figure 3-5. The transfer functions from the noise inputs to the gravitational wave readout in the open loop case where the laser light is blocked are:

$$\left.\frac{x}{s}\right|_{\text{open loop}} = ABC \qquad \left.\frac{x}{n}\right|_{\text{open loop}} = C \tag{3-7}$$

With the loop closed during normal interferometer operation,

$$\left.\frac{x}{s}\right|_{\text{closed loop}} = \frac{ABC}{1-L} \qquad \left.\frac{x}{n}\right|_{\text{closed loop}} = C \tag{3-8}$$

where the open loop gain, $L = ABP$. Thus with the loop closed, shot noise and the dark noise of the photodiode are suppressed by $1/(1-L)$ relative to the open loop measurement while the readout noise is unaffected.

The complete measurement procedure for the empirical measurement of the shot noise limit shown in Figure 3-4 follows. The laser light is blocked after taking an interfer-

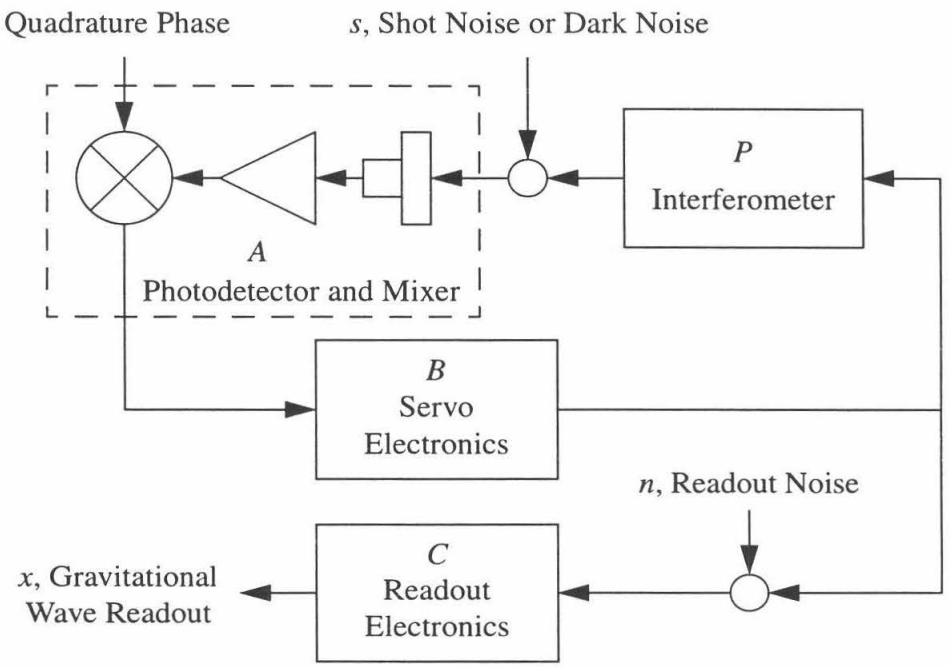

Figure 3-5: Differential mode servo loop with shot noise, dark noise and readout noise inputs.

ometer displacement spectrum and the transfer function necessary for calibration. As a check of the readout noise, the input to the readout electronics is terminated in 50 Ω and the power spectrum of the gravitational wave readout is recorded. After reconnecting the readout electronics, the power spectrum of the gravitational wave readout is recorded with no light on the antisymmetric photodiode. This is the dark noise spectrum and should be well above the level due to noise in the readout electronics, as it was in every case. Finally incandescent light was shone on the photodiode to achieve the same photocurrent as is present during normal interferometer operation. The resulting power spectrum is the shot plus dark noise spectrum. The power spectrum of shot noise alone is recovered by subtracting dark noise in quadrature.[1] This spectrum is then divided by $1/(1-L)$, to account

for the differential mode loop gain, and calibrated as usual to convert it into an equivalent amount of displacement noise.

The shot noise power spectrum should be above the dark noise spectrum by a reasonable margin. In fact, for the measurement shown in the figure, there was only approximately a 3 dB margin which is why the resulting estimate for shot noise alone is so noisy.[1]

3.6 Shot Noise in the Auxiliary Signals

In Section 2.5 formulas were derived to estimate the gravitational wave sensitivity limit due to shot noise in these auxiliary degrees of freedom. Rewriting Eq. 2-49 and Eq. 2-50,

$$\left(\frac{S_{\Phi_+ \to \Phi_-}(0)}{S_{\Phi_-}(0)}\right)^{\frac{1}{2}} \approx \left(\frac{P_S}{P_A}\right)^{\frac{1}{2}} \left(\frac{\eta_A}{\eta_S}\right)^{\frac{1}{2}} \frac{\partial v_3/\partial \Phi_+}{\partial v_1/\partial \Phi_+} \qquad 3\text{-}9$$

$$\left(\frac{S_{\phi_- \to \Phi_-}(0)}{S_{\Phi_-}(0)}\right)^{\frac{1}{2}} \approx \left(\frac{P_S}{P_A}\right)^{\frac{1}{2}} \left(\frac{\eta_A}{\eta_S}\right)^{\frac{1}{2}} \frac{\partial v_3/\partial \phi_-}{\partial v_2/\partial \phi_-} \qquad 3\text{-}10$$

The ratio between the power on the symmetric port and the power on the antisymmetric port was typically around 5. As discussed in Section 3.12 (Eq. 3-35), the ratio of the quantum efficiencies of the antisymmetric port photodiode to the symmetric port photodiode was approximately 2.[2] Using the matrix elements from Table 2-2, we estimate

---

1. This is further adjusted by increasing the shot noise power spectrum by 1 dB to reflect the fact that the measured fluctuations in photocurrent are 1 dB greater for green laser light than for incandescent light. The origin of this is not understood.
1. In some later measurements at this power level, shot noise could not be seen above the dark noise. The dark noise level seemed to depend on fine details of the grounding of the photodiodes and their power supplies and the routing of cables on the optical table.

$$\left(\frac{S_{\Phi_+ \to \Phi_-}(0)}{S_{\Phi_-}(0)}\right)^{\frac{1}{2}} \approx 0.09 \qquad 3\text{-}11$$

$$\left(\frac{S_{\phi_- \to \Phi_-}(0)}{S_{\Phi_-}(0)}\right)^{\frac{1}{2}} \approx 3.2 \qquad 3\text{-}12$$

Therefore, we do not expect the shot noise on the common mode signal to limit the gravitational wave sensitivity at any frequency. The shot noise on the beam splitter signal is more problematic, however, and we have to ensure that the open loop gain of the beam splitter servo is less than one in the gravitational wave band. This was considered in designing the loop shape of the beam splitter servo as is discussed in Appendix F.

To confirm that shot noise on neither of these two signals was limiting the gravitational wave sensitivity, we placed an attenuator before the symmetric photodiode to halve the laser light and then used an incandescent light source to increase the power on the photodiode a factor of four. We saw no observable change in the gravitational wave spectrum.

3.7 Frequency Noise

The imbalance of the arm cavities in the 40-m interferometer greatly reduces its frequency noise rejection over that specified for LIGO. Nonetheless, in the previous Fabry-Perot interferometer, where there is no frequency noise rejection, frequency noise was shown not to limit the gravitational wave signal. Because the servo system controlling the frequency is largely identical in the recombined interferometer, we expected that the

2. These quantum efficiencies include the relative efficiencies of the optical paths to the photodiodes.

recombined interferometer would not be limited by frequency noise. However, since switching to a recombined configuration, the prestabilized laser system was replaced with another system with improved automation and operator control features. Tests to set limits on the frequency noise contribution to the gravitational wave signal were performed both before and after the laser was replaced and were in reasonable agreement.

Since the common mode signal senses laser frequency variations, the test for frequency noise was to inject a monochromatic signal into the common mode servo and observe the resulting peak in both the ν_1 signal and in the interferometer output. This test would reveal any form of common mode to differential mode feedthrough, but we expect that frequency noise would dominate. We also expect any common mode to differential mode feedthrough to be essentially constant over some small region around the injected peak. By matching the peak heights and comparing the levels of the ambient backgrounds, we can estimate the common mode contribution to the interferometer output. If frequency noise was actually limiting the interferometer spectrum, the peak-to-valley ratio of common and differential mode signals will be the same. An example of one such measurement is shown in Figure 3-6.

With the original prestabilized laser, the estimated frequency noise contribution to the interferometer output at 250 Hz was less than 1×10^{-19} m/$\sqrt{\text{Hz}}$ and at 750 Hz was less than 7×10^{-20} m/$\sqrt{\text{Hz}}$.[1] This gives more than 35 dB of margin relative to the interferometer noise. With the new prestabilized laser system, there was also more than 35 dB margin between the estimated frequency noise contribution and the interferometer noise.

---

1. These numbers are upper bounds because the background noise measured in these measurements was limited by readout noise and not the true servo signal.

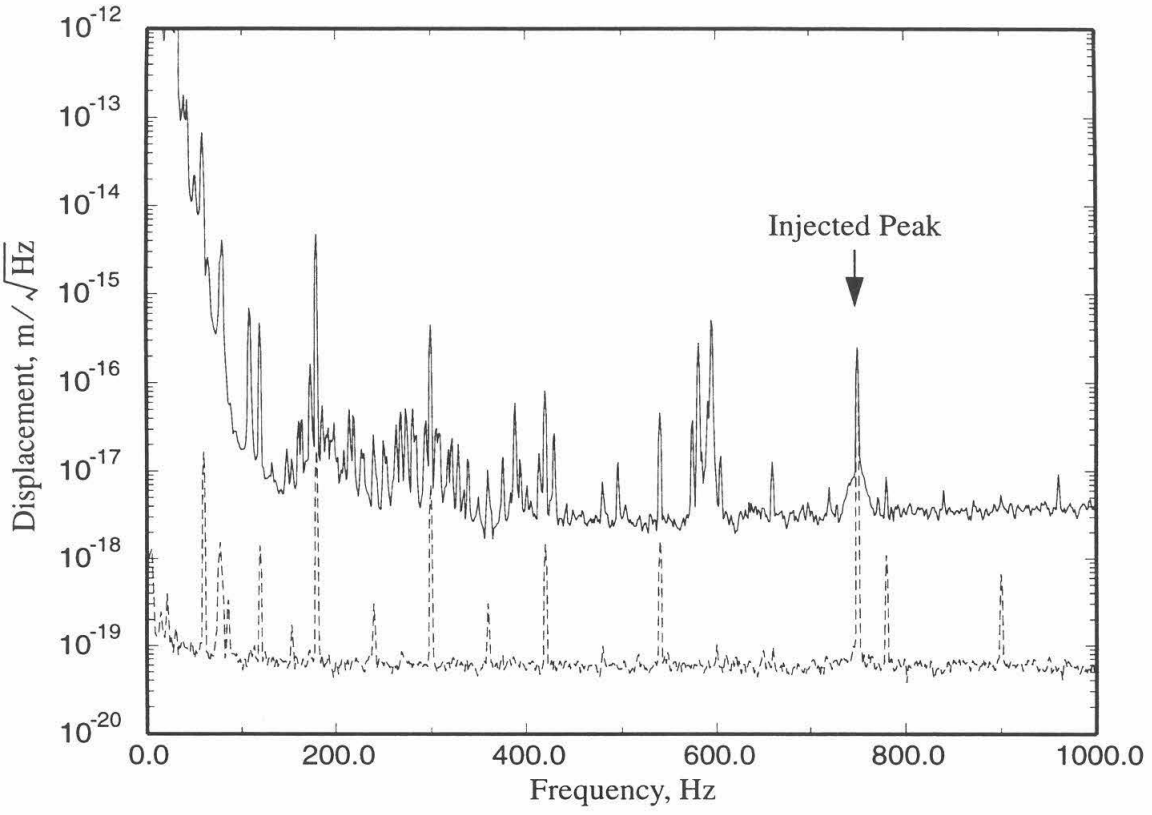

Figure 3-6: Estimated frequency noise contribution (dotted) valid only in a small region around the 750 Hz injected peak to the interferometer output (solid) on November 30, 1995.

3.8 Intensity Noise

Intensity noise on the light incident on the interferometer can appear as noise in the gravitational wave readout. Deviations from the arm cavity resonance length increase sensitivity in the gravitational wave signal to intensity fluctuations in the signal band. RF intensity fluctuations can occur even when the arm cavity is exactly in resonance and can be seen directly after being demodulated by the mixers. A number of measurements were performed to show that noise due to in-band and RF intensity fluctuations were not limit-

ing the gravitational wave sensitivity.

There are three ways to estimate the in-band contribution of intensity noise to the gravitational wave signal. The most straightforward is to do the transfer function measurement from the intensity noise to the interferometer output as shown in Figure 3-7. A signal is fed into the test input of the intensity stabilization servo and the transfer functions from this point to the interferometer output (G) and to an independent monitor photodiode (H) are measured. The so-called Z1 photodiode is a low noise photodiode which is not part of the intensity stabilization loop. The ratio of these two transfer functions allows us to infer a transfer function from the noise observed by the Z1 photodiode to the interferometer output (G/H). The observed intensity noise is multiplied by this transfer function to derive an estimated contribution to the interferometer output due to intensity noise. The estimated contribution from intensity noise with the original prestabilized laser is shown in Figure 3-8.

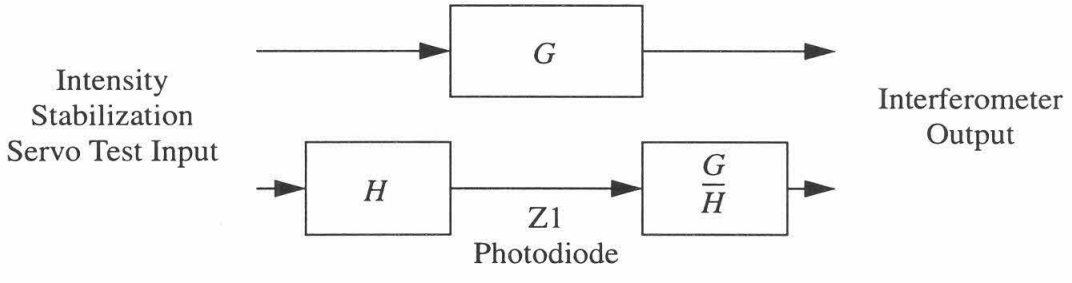

Figure 3-7: Transfer function method of measuring intensity noise contribution to interferometer output.

A problem with this method of measuring the intensity noise contribution to the interferometer output is that it requires long integration times at each frequency point. This is because the intensity noise feeds into the gravitational wave signal via deviations from the

arm cavity fringe which are time varying around near perfect resonance. In a transfer function measurement, the phase is important and excursions on either side of the fringe give opposite phases in the measurement of G above. Averaged over sufficiently long times, the transfer function measured is that due to the very small static offset from the fringe.

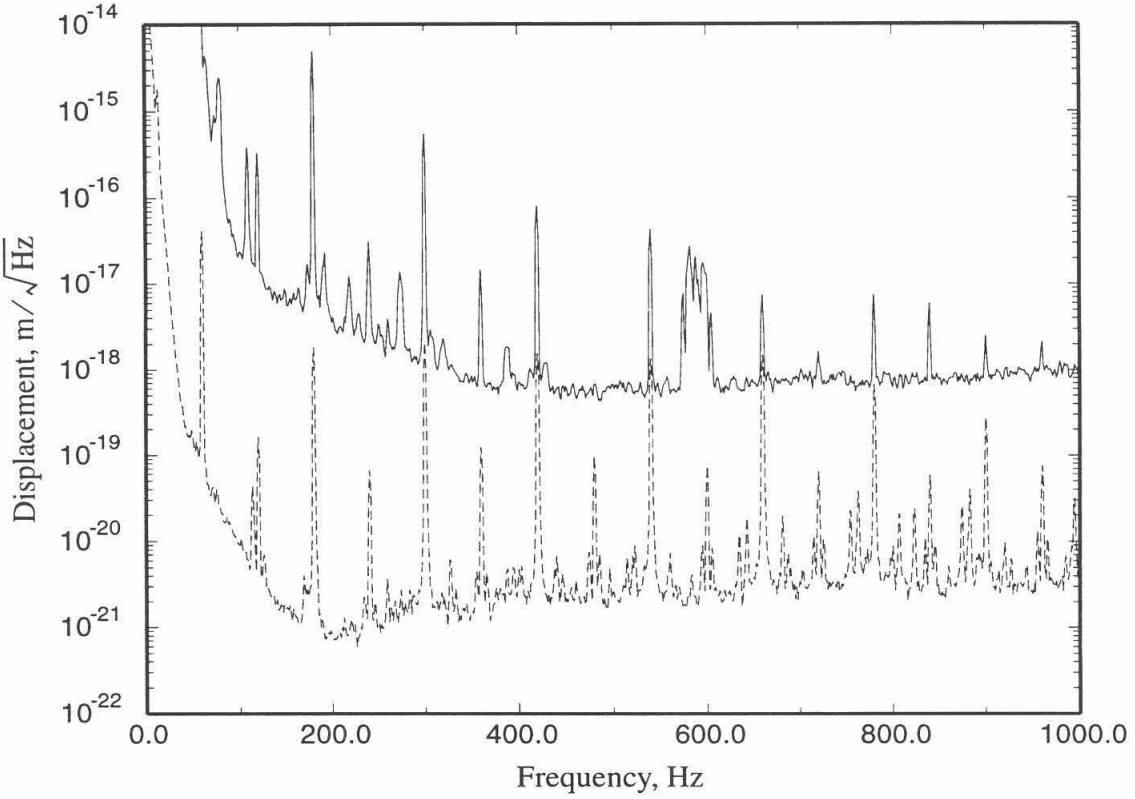

Figure 3-8: Estimated intensity noise contribution (dashed) to interferometer output (solid) on January 9, 1996, using the transfer function method.

A second method of measuring the contribution of intensity noise to the interferometer output is to inject a monochromatic intensity signal at a level sufficient to increase the noise in the interferometer output at this frequency. By comparing the peak-to-valley ratios of the peak in the interferometer output and in the light measured by the Z1 photo-

diode, we can set a limit on the intensity noise contribution near the frequency of the peak. This has the advantage that the measurements taken are power spectra and thus what is important is the rms deviation from the arm cavity fringe and not the average.[1] An example of one such measurement using the original prestabilized laser is shown in Figure 3-9. Notice that the injected peak is broadened in the interferometer output. Depending on the broadening mechanism, this could lead to a falsely low estimation of the intensity noise contribution. The estimated intensity noise contribution using this method at 850 Hz is 3×10^{-19} m$/\sqrt{\text{Hz}}$.

A final method for estimating the intensity noise contribution to the interferometer output, which does not suffer from the ambiguity of the broadened peaks, is to inject white intensity noise. White intensity noise was injected at a level to clearly show up in the interferometer output above the ambient noise background. The drive level was then doubled to check for linearity which did produce a 6 dB increase in the interferometer noise level. Using this method, the intensity noise contribution was 3×10^{-19} m$/\sqrt{\text{Hz}}$ at 850 Hz and was relatively flat from 500 - 1000 Hz.

The estimated intensity noise contribution to the interferometer output from the peak-to-valley and white noise methods are in good agreement and set a level of 3×10^{-19} m$/\sqrt{\text{Hz}}$ from 500 - 1000 Hz. The estimate for the intensity noise contribution purely from static offsets of the arm cavity fringes (using the transfer function method) is 60 times lower. Thus we can conclude that it was the rms deviation from the fringe that was important for intensity noise.

---

1. RMS excursions enable intensity noise to couple into the interferometer output even when the static offset is zero.

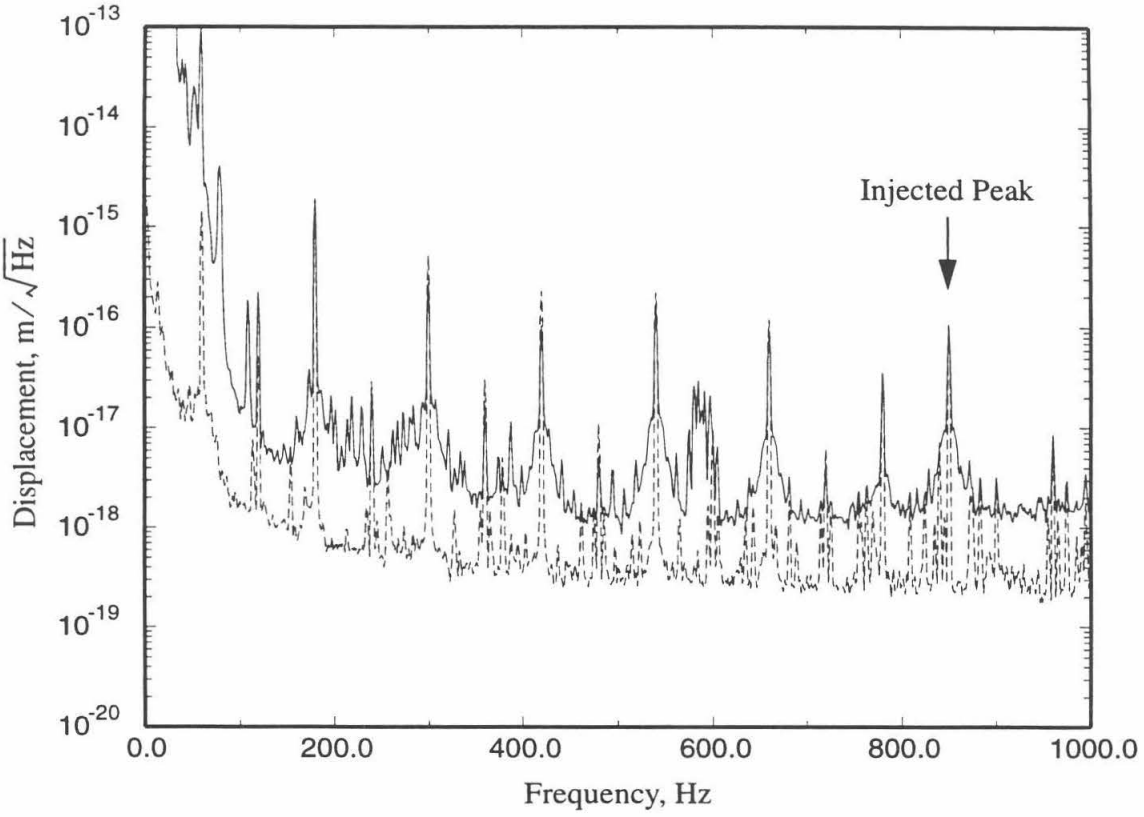

Figure 3-9: Estimated intensity noise contribution (dotted) valid only in a small region around the 850 Hz injected peak to the interferometer output (solid) on October 31, 1995.

As part of the characterization of the new prestabilized laser system, the relative intensity noise was measured at 500 Hz and compared to the original system. The original prestabilized laser had a relative intensity noise of 7×10^{-8} $\mathrm{Hz}^{-1/2}$ while the new system has been measured to have

$$\frac{S_I^{1/2}}{I} \approx 4\times10^{-7}\ \mathrm{Hz}^{-1/2} \qquad 3\text{-}13$$

This factor of 6 degradation in performance suggests that the intensity noise should now be limiting the gravitational wave sensitivity at some frequencies. A check of this with the

new laser system using the white noise method showed that the gravitational wave sensitivity is limited by intensity noise above approximately 500 Hz. This was verified with a peak-to-valley measurement at 750 Hz.

A test for RF intensity noise is to misalign all the masses except for one vertex mass so that the light incident on the interferometer is reflected straight back along the same path to the photodiodes. After measuring the demodulated signal at one photodiode (typically the symmetric photodiode), the laser light is blocked and the same amount of power is put on the photodiode with a flashlight. If the intensity noise of the light is shot noise limited around 12 MHz as desired, then the flashlight demodulated signal will be identical to the laser light signal. For both prestabilized laser systems, this was true above 200 Hz. The excess noise that was occasionally seen on the green light spectrum below 200 Hz was most likely due to a spurious interference path formed between optics in the beam splitter chamber.

3.9 Beam Splitter Motion

Beam splitter motion can affect the interferometer output in two ways. The low frequency (less than 10 Hz) rms motion of the beam splitter can degrade the dark fringe at the antisymmetric port as discussed in Section 2.8. Motions of the beam splitter in the gravitational wave band can also limit the interferometer sensitivity. Both of these effects are discussed below.

To compare with the specification given in Section 2.8 and to understand the effects of low frequency beam splitter motion, the power spectrum of the residual beam splitter motion was measured and calibrated. An analogous calibration method to that described in

Section 3.4 could not easily be used here because there was no convenient way to sum a signal into the beam splitter position directly at the drive coils.[1] Instead, the power spectrum of the feedback to the beam splitter drive coils was recorded, and this was converted to the actual residual motion of the beam splitter by measuring the beam splitter open loop gain and making some assumptions about where the noise terms that dominate the beam splitter motion sum into the servo loop.

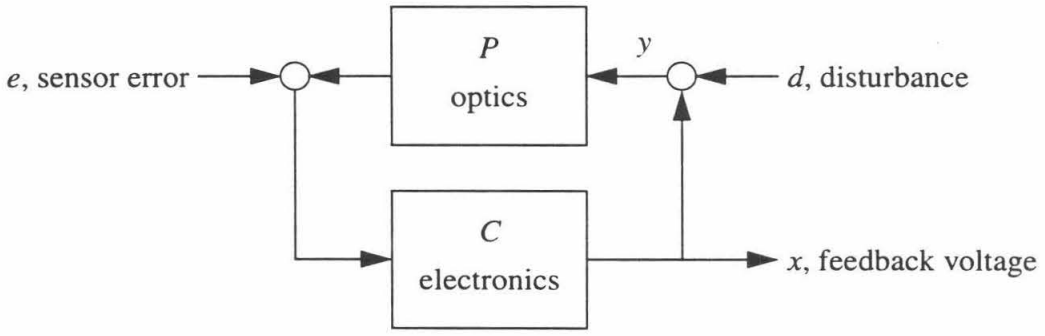

Figure 3-10: Diagram of beam splitter servo loop, showing various noise sources driving the beam splitter motion (y).

A schematic diagram of the beam splitter servo loop is shown in Figure 3-10. The transfer functions from the two types of noise sources are:

$$\frac{x}{d} = \frac{PC}{1-PC} \qquad \frac{y}{d} = \frac{1}{1-PC} \tag{3-14}$$

$$\frac{x}{e} = \frac{C}{1-PC} \qquad \frac{y}{e} = \frac{C}{1-PC} \tag{3-15}$$

If the noise source dominating the beam splitter motion is a disturbance (primarily seismic motion), then we can use Eq. 3-14 to find the relation between the feedback and the actual

1. With the new test mass suspensions that are being installed in the 40-m interferometer, this will change as it will be possible to drive the vertex test masses.

beam splitter motion,

$$\frac{y}{x} = \frac{1}{PC} \qquad 3\text{-}16$$

However, if the noise source dominating the beam splitter motion in a particular frequency band is a sensor error (shot noise or electronic noise), then we use Eq. 3-15 instead to find

$$\frac{y}{x} = 1 \qquad 3\text{-}17$$

We shall assume that the seismic disturbance dominates. This is certainly true in the frequency region below 10 Hz that we are concerned about, which accounts for most of the beam splitter rms motion. Thus we measure the feedback voltage, divide this by the open loop gain of the servo, and then multiply by the conversion from voltage to displacement for the beam splitter drive.

The beam splitter drive voltage to displacement conversion was done in the same way as for the end masses. The beam splitter was driven with a signal at 9 Hz far above its natural motion due to seismic noise, and the voltage required to move the beam splitter through two fringes (a total displacement of λ) was recorded on successive measurements. The calibration measured was

$$x(f) = \left(4.28\times10^{-6}\ \frac{\text{m Hz}^2}{\text{V}}\right)\frac{V_{\text{fb}}}{f^2} \qquad 3\text{-}18$$

where V_{fb} is the voltage fed back to the beam splitter OSEM module position input.

The estimated residual beam splitter motion is shown in Figure 3-11.[1] The rms

1. As discussed above we expect the low frequency part of this data to be accurately calibrated, although closer to 100 Hz the figure may be in error by as much as the open loop gain of the servo at those frequencies. For this measurement this would correspond to overestimating the motion at 100 Hz by less than a factor of three.

motion obtained by integrating this data is 1.34 nm which meets the specification on Table 2-3 of less than 4 nm.

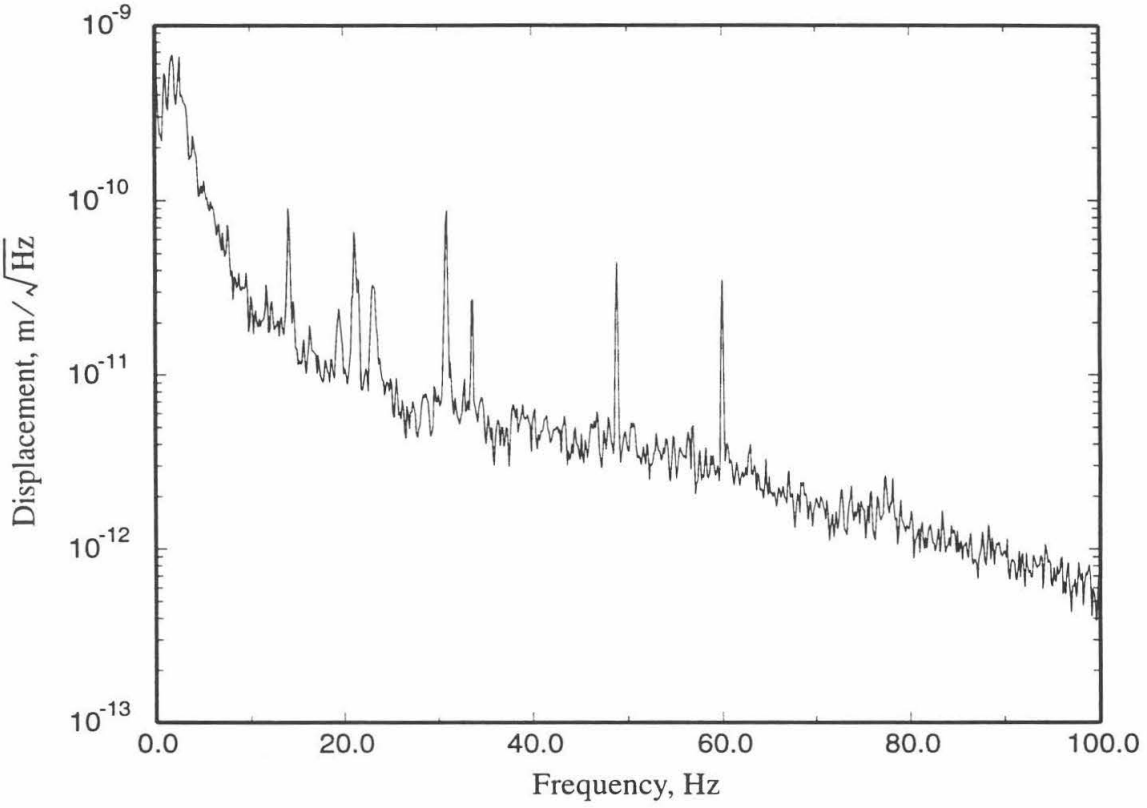

Figure 3-11: Residual beam splitter motion.

The fluctuations in the beam splitter position at frequencies above 100 Hz can also limit the gravitational wave sensitivity. A check of the beam splitter contribution to the interferometer output revealed that the beam splitter does not limit the gravitational wave sensitivity. The beam splitter motion contribution is measured using a transfer function method as shown in Figure 3-12. The transfer function from the beam splitter servo test input to the interferometer output (G) is measured first. The transfer function from this test input to the beam splitter feedback signal (H) is also measured. From this the transfer

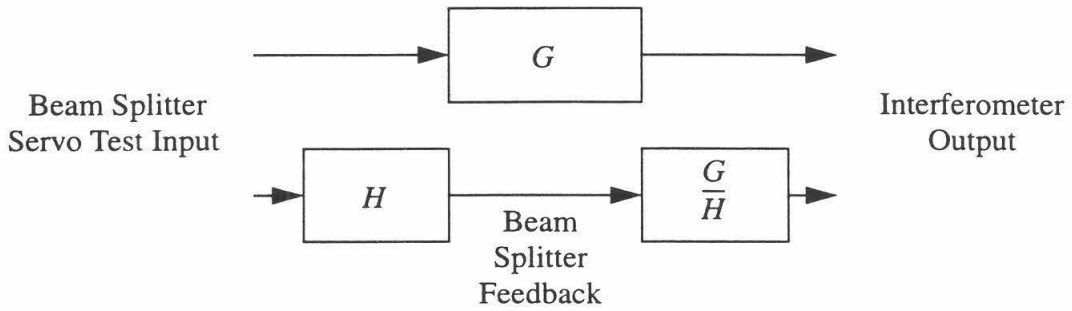

Figure 3-12: Transfer function method of measuring the beam splitter motion contribution to interferometer output.

function from the beam splitter feedback to the interferometer output can be inferred by calculating *G/H*. The ambient power spectrum measured at the beam splitter feedback is then multiplied by this transfer function to find its contribution to the interferometer output. The results of this measurement are shown in Figure 3-13, plotted for comparison with the best interferometer output sensitivity achieved during operation in the recombined configuration.

3.10 Output Noise in the Beam Splitter Coil Driver

The coils controlling the beam splitter are driven by two circuits which sum together through a resistive network immediately before the coil. One drive circuit provides orientation control to maintain stable alignment of the beam splitter while the other controls the longitudinal motion of the beam splitter and derives its signal from v_2. If the output noise of either of these drive circuits is too high, this could corrupt the gravitational wave readout.

The output noise of the orientation drive circuit at 100 Hz has been measured to be 30

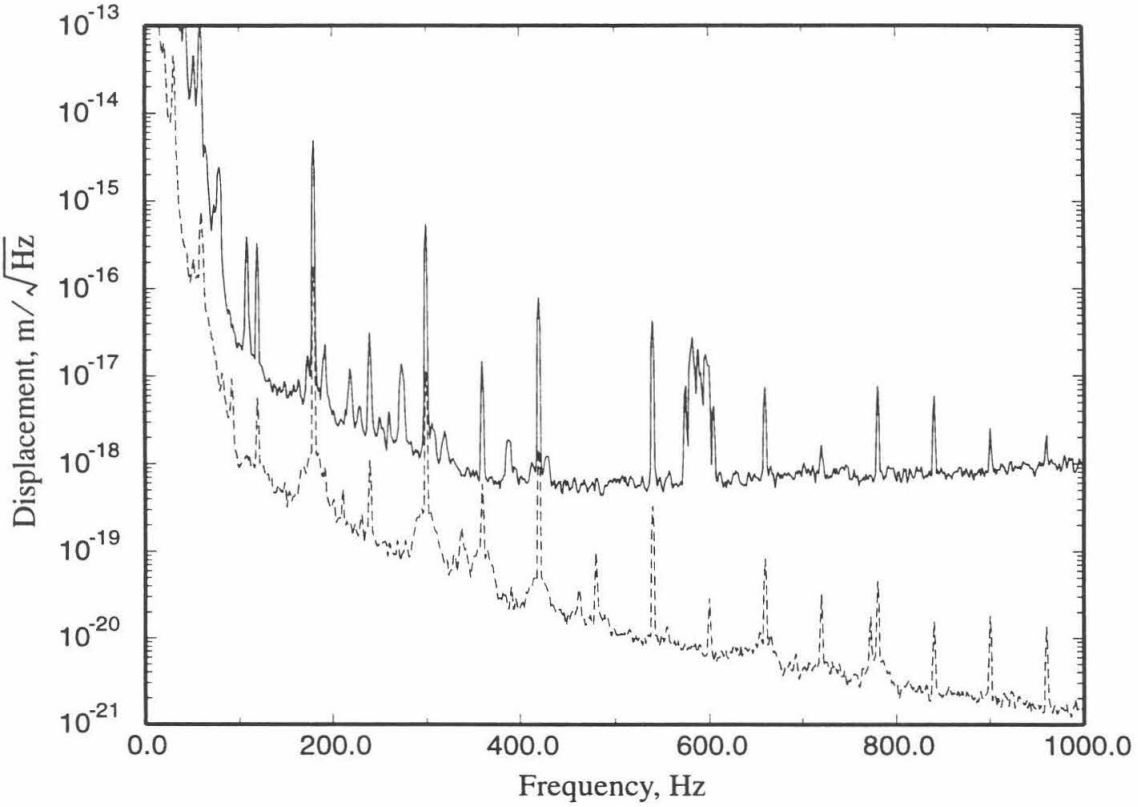

Figure 3-13: Beam splitter motion contribution to interferometer output (dotted) shown for comparison with the best interferometer noise spectrum (solid), taken on January 9, 1996.

$\mathrm{nV}/\sqrt{\mathrm{Hz}}$. The conversion to beam splitter displacement is on the order of 1 mm/V at DC. Thus, accounting for the pendulum suspension, at 100 Hz the output noise is

$$S_o^{\frac{1}{2}} \sim 3\times10^{-15}\ \mathrm{m}/\sqrt{\mathrm{Hz}} \qquad 3\text{-}19$$

The arm cavity differential motion equivalent to this beam splitter motion in the gravitational wave signal is

$$S_{arm}^{\frac{1}{2}} = \frac{\partial v_3/\partial \phi_-}{\partial v_3/\partial \Phi_-} S_o^{\frac{1}{2}} \qquad 3\text{-}20$$
$$\sim 2\times10^{-19}\ \mathrm{m}/\sqrt{\mathrm{Hz}}$$

The electronic noise of the longitudinal drive circuit measured with the laser light blocked at 100 Hz is 14 $\mu V/\sqrt{Hz}$. The conversion to displacement of the beam splitter at 100 Hz is 4.28×10^{-10} m/V because of the resistive divider network where this signal sums in with the orientation signal. Thus, the displacement of the beam splitter due to all forms of electronic noise in the longitudinal drive servo is 6×10^{-15} $m/\sqrt{Hz}$. This is equivalent to an arm cavity differential motion in the gravitational wave signal of 4×10^{-19} $m/\sqrt{Hz}$.

3.11 Contrast Defect

We typically observed 3% contrast defects after careful alignment, with fluctuations as low as 2%. Using the results of Section 2.7 and measured parameters, the various contributions to this are discussed below. The sources of contrast defect considered are rms motion of the beam splitter, differing arm cavity visibilities, alignment fluctuations, wavefront distortion due to mirror imperfections, and the asymmetry. The budget for the various contributions of contrast defect is summarized at the end of this section in Table 3-3.[1]

The rms motion of the beam splitter was shown in Section 3.9 to be 1.3 nm, thus $\phi_-^{rms} = 3.3\times10^{-2}$. Using Eq. 2-53 we find that this rms beam splitter motion will give 0.05% contrast defect which easily meets the rms contrast fluctuation requirements of Sec-

1. These summarized measurements are taken after the mode matching of carrier light into the arm cavities was optimized.

tion 2.8.

The visibilities observed in the two arms at low modulation depth when the arms were aligned for maximum transmitted light (and hence maximum circulating power) were 88% for the east arm and 74% for the south arm. This difference is primarily due to the lower mirror losses of the south arm. For the east arm it was noted that in aligning to maximize the visibility, one could achieve a visibility of 91%. This is believed to be due to non-uniform losses across the surface of the mirrors. Because the arm cavities are over coupled, aligning for peak visibility may lead to slightly misaligning the cavity so that the resonant spot is on an area of higher loss. For comparison the energy storage time of the east arm aligned for maximum visibility on one particular day was 447 μs while it was 508 μs when aligned shortly afterwards for maximum transmitted light. For this reason the cavities were routinely aligned for maximum transmitted light in normal operation. Using Eq. 2-56 the contrast defect due to the unequal arm cavity visibilities is 1.3%.

The contrast defect due to alignment fluctuations is given by Eq. 2-60. As a worst case estimate for the angular tilt in the returning beam axis, we use the orientation noise of the test masses. Thus $\theta_{rms} \approx 5\times10^{-6}$ rad, or 0.2 mm of spot motion over 40 m. Note that for the 2.2 mm waist size in the 40-m interferometer, the approximations made in deriving Eq. 2-58 and Eq. 2-59 are valid. Thus, we calculate the fraction of the light returning from the arms that does not interfere due to the non-parallel phase fronts, $k_1 = 0.45\,\%$, and the fraction that does not interfere due to motion of the beam spot, $k_2 = 0.83\,\%$. The average arm cavity visibility is 81%; therefore, the contrast defect due to angular fluctuations is 0.49%.

The phase bumps in the middle of the vertex test masses of both arms may be a source of contrast defect. As an estimate of the size of this effect, we consider the contrast defect induced by one such bump in an otherwise perfect interferometer. In Eq. 2-66 the waist size of the arm with the distorted vertex test mass is given. The height of the phase bump, s, has been measured to be approximately $\lambda/50$ to $\lambda/70$. The length of the arm cavities, l = 38.5 m and the radius of curvature of the end mirrors, R = 61 m. From Eq. 2-66 and Eq. 2-67 we see w = 2.171 mm and w' = 2.132 mm. Therefore, from Eq. 2-62, the contrast defect from a worst case $\lambda/50$ phase bump is 0.01%.

The contrast defect arising from the different size and curvature of the modes returning from the two arms due to the asymmetry is given by Eq. 2-69. For the 50.8 cm asymmetry used, the additional contrast defect is 0.33%.

Table 3-3: Contrast Defect Contribution Budget

Mechanism	Contribution
RMS beam splitter motion	0.05%
Arm cavity visibilities	1.3%
Alignment fluctuations	0.49%
Wavefront distortion	0.01%
Asymmetry	0.33%
Total	2.18%

3.12 Validation of the Matrix of Discriminants

A goal of recombination was to provide further validation of the models developed for the asymmetric signal extraction scheme. In particular, we wish to verify experimentally the matrix of discriminants shown in Table 2-2. This is quite difficult in practice

because the matrix of discriminants which describes the optical response of the interferometer can only be measured when the interferometer is being actively controlled by servo loops to keep it in a linear region of operation. Because there is a large degree of cross coupling between the various extracted signals and degrees of freedom, we must treat the interferometer as a MIMO system in calculating the effect of the servo loops on our measurement.

3.12.1 Closed Loop Measurements

We made the closed-loop response measurements shown in Figure 3-14. Note that the block elements representing electrical or optical transfer functions are matrices and that the signals shown are vectors containing information on all three servo loops.[1] The interferometer response, P, is the matrix of discriminants we wish to verify. The other matrices are various parts of the servo loops and are diagonal or very nearly diagonal. We injected a signal into the servo loops one at a time at 132.5 Hz at summing point d, and observed the disturbance actually present in the loop at point x, immediately before the transducer which converts the servo signal to displacement of that degree of freedom. We also observe the signals induced at our drive frequency in all three servos at the outputs of the three mixers, y_i. 132.5 Hz was chosen because it was a relatively quiet area of the noise spectrum for all three degrees of freedom. The power spectrum of the x and y signals were measured using an HP 3563A Spectrum Analyzer and the values at 132.5 Hz were divided to compute the magnitude of the transfer function from x to y at this frequency.

The closed loop response to driving the common mode had to be corrected by a mea-

1. We use the same notation as previously: the first element of a vector is the common mode signal, the second is the beam splitter signal and the third is the differential mode signal.

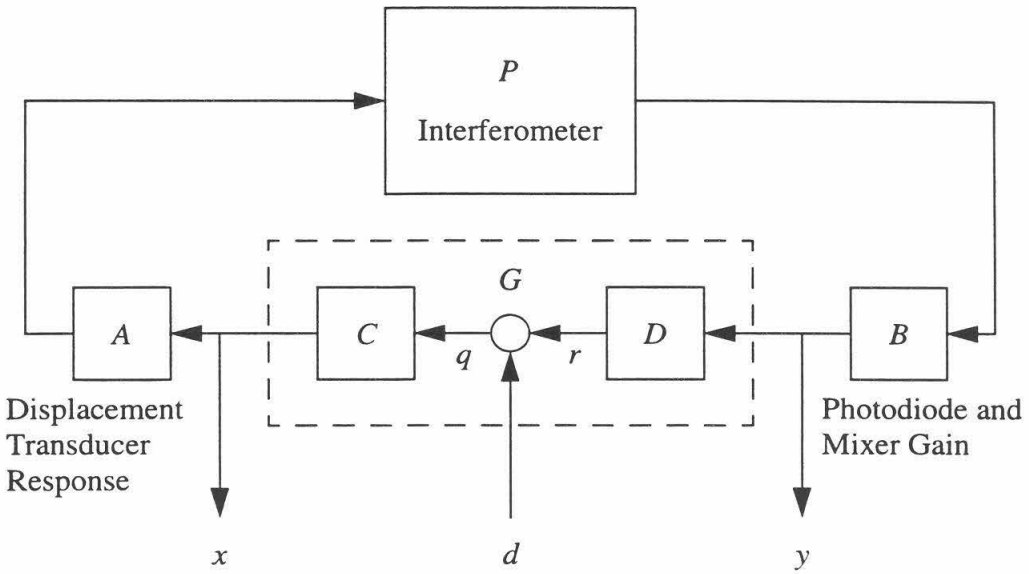

Figure 3-14: Block diagram of closed-loop interferometer showing signals extracted for interferometer response measurements.

sured loop gain factor. This is because unlike the beam splitter and differential mode servos, the common mode has three different feedback paths as discussed in more detail in Appendix E. At very low frequencies below a few Hz, it drives the test masses directly. At higher frequencies the drive to the test masses is inactive and the feedback is applied to the laser frequency instead, through the remaining two feedback paths. Unfortunately the only feedback path in the common mode servo where we have a solid calibration of voltage to displacement is the drive to the test masses. It is not practical to make the measurements described here at frequencies where this is the dominant feedback path because they would be swamped by seismic noise. Thus we are forced to account for the effects of the other feedback paths in the measurements that involve driving the common mode degree of freedom.

Consider the simplified block diagram of the common mode servo shown in Figure 3-

15. Here we have modeled the common mode servo as being composed of only two feedback paths, one fast and one slow, but our results will easily generalize. Consider first that we remove C_1 and look at the transfer function from q to x. In this case the combinations of P and C_2 will look like a new effective optical transfer function.

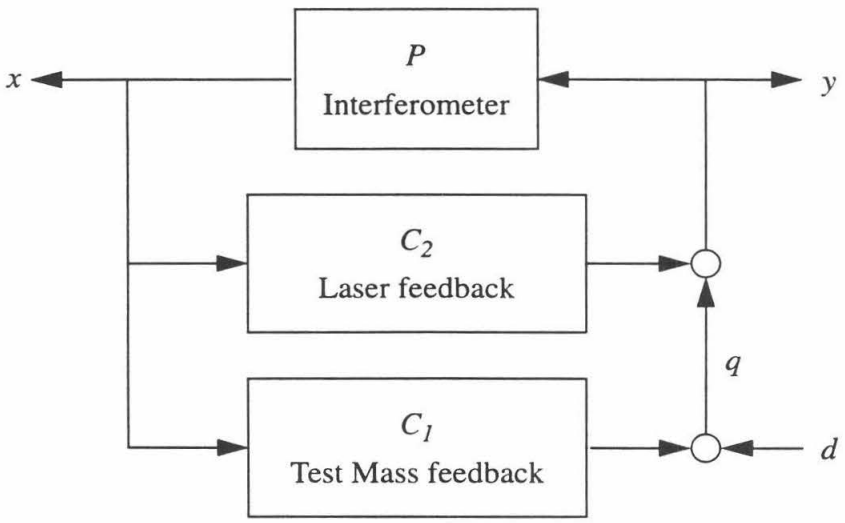

Figure 3-15: Simplified block diagram of common mode servo with two feedback paths.

$$\left.\frac{x}{q}\right|_{C_1 \text{ removed}} = \frac{P}{1 - PC_2} \qquad 3\text{-}21$$

The transfer functions with all feedback paths active then are

$$\frac{x}{d} = \frac{\left.\frac{x}{q}\right|_{C_1 \text{ removed}}}{1 - \left(\left.\frac{x}{q}\right|_{C_1 \text{ removed}}\right) C_1} = \frac{P}{1 - PC_1 - PC_2} \qquad 3\text{-}22$$

$$\frac{q}{d} = \frac{1}{1-\left(\frac{x}{q}\Big|_{C_1 \text{ removed}}\right)C_1} = \frac{1-PC_2}{1-PC_1-PC_2} \qquad 3\text{-}23$$

Thus the open loop gains of each of the feedback paths add to form the open loop gain of the entire servo as we might have expected. The transfer function we measured in determining the common mode to common mode response was from q to x.

$$\frac{x}{q} = \frac{x}{d}\left(\frac{q}{d}\right)^{-1} = \frac{P}{1-PC_2} \qquad 3\text{-}24$$

We wanted to measure P, but it is suppressed by the gain of the faster part of the servo loop. This is true for the off-diagonal matrix element measurements as well because the real common mode change induced is much less than that measured by looking at the drive to the test masses because the servo suppresses this motion by changing the frequency of the light to compensate. Thus we had to correct all the measured interferometer responses to driving the common mode by multiplying them by $1-PC_2 \approx 1-L_1$, where L_1 is the common mode open loop gain.

3.12.2 Calculated Closed Loop Response

Referring back to Figure 3-14, we can calculate the expected interferometer response by considering the closed-loop matrix equations:

$$y = BPACq \qquad q = r+d \qquad r = Dy \qquad 3\text{-}25$$

$$y = BPACDy + BPACd \qquad 3\text{-}26$$

$$y = (I-BPAG)^{-1}BPACd \qquad 3\text{-}27$$

where I is the identity matrix and $G = CD$. Now to solve for x in terms of d, we note

$$y = BPAx \rightarrow x = (BPA)^{-1} y \tag{3-28}$$

$$x = (BPA)^{-1}(I - BPAG)^{-1} BPACd \tag{3-29}$$

Now for a particular response measurement from loop j to loop k, we consider[1]

$$\begin{aligned} y_k &= [(I - BPAG)^{-1}]_{\text{row } k}\, BPACd \\ x_j &= [(BPA)^{-1}\,(I - BPAG)^{-1}]_{\text{row } j}\, BPACd \end{aligned} \tag{3-30}$$

For each measurement where we observe x_j, we inject a signal at 132.5 Hz only into that servo. Thus, only the jth element of d will be non-zero and this will pick out the jth column of $BPAC$.

$$\frac{y_k}{x_j} = \frac{[(I - BPAG)^{-1}]_{\text{row } k}\, [BPAC]_{\text{col } j}}{[(BPA)^{-1}\,(I - BPAG)^{-1}]_{\text{row } j}\, [\,BPAC]_{\text{col } j}} \tag{3-31}$$

Now we exploit the fact that C is a diagonal matrix and the identity which is true for any matrix M and diagonal matrix C:

$$[MC]_{\text{col } j} = M_{\text{col } j}\, C_{j,\,j} \tag{3-32}$$

$$\begin{aligned} \therefore \frac{y_k}{x_j} &= \frac{[(I - BPAG)^{-1}]_{\text{row } k}\, [BPA]_{\text{col } j}}{[(BPA)^{-1}\,(I - BPAG)^{-1}]_{\text{row } j}\, [BPA]_{\text{col } j}} \\ &= \frac{[(I - BPAG)^{-1}\, BPA]_{k,\,j}}{[(BPA)^{-1}\,(I - BPAG)^{-1}\, BPA]_{j,\,j}} \end{aligned} \tag{3-33}$$

---

1. We make use of the following matrix identities which are true for any matrices A and B and vector x:

$$[AB]_{\text{row } j} = A_{\text{row } j}\, B \qquad [Ax]_{\text{row } j} = A_{\text{row } j}\, x$$

This gives us a way to relate our calculated matrix of discriminants to experiment.[1] We first measure y_k/x_j for all combinations as shown in Figure 3-14. Then we measure *A*, *B* and *BPAG* and use Eq. 3-33 to calculate the effect of the servo loops in converting the theoretical matrix of discriminants, *P*, to expected values for y_k/x_j. We ultimately renormalize all our y_k/x_j such that the differential mode drive to differential mode mixer output is 1.0, just at we did for the matrix of discriminants. Thus what is important for all the matrices is the ratio of the various elements and not their absolute size in any particular units.

3.12.3 Measuring the Gain Matrices

The *A* matrix gives the displacement transducer responses. We assume the response for the common mode and differential mode are equal as they drive the same coils at the two end test masses. The common mode drive voltage was measured by summing together the signals from the recombination coil driver going to each end test mass. Similarly the differential mode drive voltage was measured by taking a difference of these signals. The voltage to displacement into the calibration input for the east end test mass is known and its measurement is described in Section 3.4. The ratio between the source voltage level setting on the HP 3563A spectrum analyzer into this calibration input and the equivalent common mode drive voltage is 171.5. Thus, the conversion from the common mode drive voltage to displacement is 3.06×10^{-10} m/V_{rms} at 132.5 Hz.The cross coupling of the common and differential mode inputs of the recombination coil driver was also measured and

1. Note that in [37], Eq. 3-33 is given incorrectly and without derivation. The analytic expression given there, however, was never used to compare the model with experiment as a numerical method of calculating the effect of the servos was used instead.

included as off-diagonal elements in the A matrix. From Section 3.9, the beam splitter drive voltage to displacement calibration is 2.44×10^{-10} m/V_{rms} at 132.5 Hz. After renormalizing,

$$A = \begin{bmatrix} 1.0 & 0 & 1.3\times10^{-3} \\ 0 & 1.3 & 0 \\ 7.1\times10^{-3} & 0 & 1.0 \end{bmatrix} \qquad 3\text{-}34$$

Matrix B is the product of the transmission of the optical path from the beam splitter to the antisymmetric or symmetric port photodiode, the efficiency of the photodiodes and the gains of the mixers. The transmission from the beam splitter to the antisymmetric port is 1.769 times higher than the transmission to the symmetric port. This is because the symmetric port light travels back through a number of small aperture optics including the Faraday isolator before reaching the photodiode. To measure the efficiency of the photodiodes and the mixer gains together, a sine wave at very close to the 12.33 MHz modulation frequency was injected into the photodiodes' test inputs as shown in Figure 3-16. This adds the signal in directly across the photodiode and is equivalent to light producing a photocurrent at this frequency.[1] Each photodiode output is demodulated at a mixer as usual and the resulting peak height in the spectrum of the mixer output is compared with the heights from the other mixers. The frequency of the injected signal is adjusted to give a demodulated peak close to the frequency of interest. The mixer outputs had peak heights at the same injected signal level of -73.614 dBV_{rms} for the ν_1 signal, -75.0 dBV_{rms} for the

1. The photodiodes have different efficiencies primarily because the photodiode itself is part of an LC circuit which is tuned for 12.33 MHz. The electrical gain from this circuit can vary by up to an order of magnitude from photodiode to photodiode.

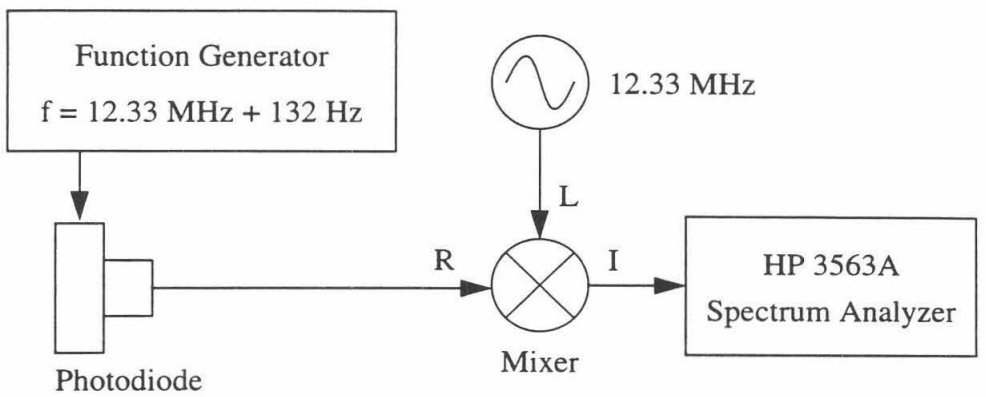

Figure 3-16: Procedure for measuring relative photodiode and mixer efficiencies.

v_2 signal, and -63.139 dBV_{rms} for the v_3 signal. Thus, multiplying these relative gains together and renormalizing,

$$B = \begin{bmatrix} 1.17 & 0 & 0 \\ 0 & 1.0 & 0 \\ 0 & 0 & 6.93 \end{bmatrix} \qquad 3\text{-}35$$

To form the matrix product *BPAG*, we need to measure *G*. *G* is a diagonal matrix representing the electronic gain of each servo loop not included in *A* or *B*. Instead of measuring *G* directly, we measure the open loop gain of each servo loop at 132.5 Hz and form

$$G_{ij} = \begin{cases} \dfrac{L_i}{B_{ii} P_{ii} A_{ii}} & i = j \\ 0 & i \neq j \end{cases} \qquad 3\text{-}36$$

where L_i are the open loop gains of the three servo loops. In this way we automatically preserve the correct phase relationships that we may have ignored in only considering the magnitude of the *A* and *B* matrices.

Measuring the open loop gains of the servos controlling the three degrees of freedom is complicated by the fact that the optical part of the servo loops is only linear in its response when the servo loops are closed. Thus to measure the open loop gain of each particular loop, we need to make a closed loop measurement and calculate the effective open loop gain. As shown in Figure 3-17, we feed a test signal into d and measure the transfer

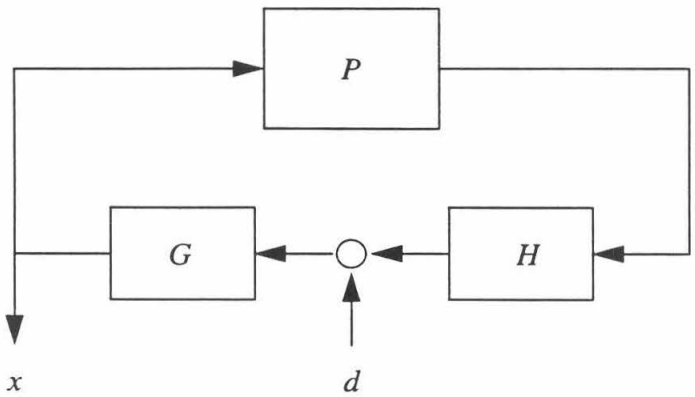

Figure 3-17: Block diagram of open loop gain measurement.

function to x. In the diagram P is the optical part of the gain, while H and G are the parts of the electronic gain before and after the summing junction respectively. Any convenient summing junction and monitor point that is buffered from it and later in the electronic path may be used, but in practice there are limited choices of test inputs and outputs in the electronic modules. With the loop closed the transfer function from d to x is

$$\left.\frac{x}{d}\right|_{\text{closed loop}} = \frac{G}{1 - GPH} \qquad 3\text{-}37$$

After measuring the closed loop response, we break the servo loop somewhere before the summing junction and after the monitor point, typically by blocking the laser light. Then

we remeasure the transfer function from d to x,

$$\left.\frac{x}{d}\right|_{\text{open loop}} = G \qquad 3\text{-}38$$

We can then find the open loop gain of the servo loop by calculating

$$GPH = 1 - \left.\frac{x}{d}\right|_{\text{open loop}} / \left.\frac{x}{d}\right|_{\text{closed loop}} \qquad 3\text{-}39$$

Using this procedure we find that at 132.5 Hz,

$$\begin{aligned} L_1 &= 9.368\times10^{4} + i\ 2.168\times10^{5} \\ L_2 &= 1.592\times10^{-1} - i\ 4.626\times10^{-2} \\ L_3 &= 2.936\times10^{1} - i\ 6.903\times10^{-1} \end{aligned} \qquad 3\text{-}40$$

3.12.4 Comparison of Calculated and Measured Interferometer Response

For this calculation we will not use the matrix of discriminants from Table 2-2 because, as discussed in Section 3.3, we can not reasonably expect the beam splitter demodulation phase to be set more accurately than within 10°. For comparison with our data, we will use a matrix of discriminants calculated assuming a 10° beam splitter mixer phase error,[1] which we write as[2]

---

1. Note that the choice of 10° is not critical. The amount of common mode feedthrough depends linearly on the phase error for small phase errors such as these. Negative phase errors give a dependence on the common mode length of equal magnitude to positive errors. Thus, the common mode and differential mode feedthrough to the beam splitter signal which are derived from a 10° phase error are probably good estimates to within an order of magnitude.
2. Note that in matrix form this is transposed from how it appears in Table 2-2 because in the table the inputs (degrees of freedom) appeared as rows and the outputs (extracted signals) appeared as columns for readability.

$$P = \begin{bmatrix} 7.8 & 2.3\times10^{-4} & 2.5 \\ 1.3 & 1.5\times10^{-4} & 4.0\times10^{-1} \\ 2.2\times10^{-1} & 1.9\times10^{-4} & 1.0 \end{bmatrix} \qquad 3\text{-}41$$

Using this we can calculate the expected interferometer response measurements (y_k/x_j).

The calculated interferometer response is shown in Table 3-4 along with the values measured in the lab. The agreement is within the errors of the measurement except for the upper right block of values.[1] These discrepancies are discussed below.

Table 3-4: Comparison of Calculated (shaded) and Measured (normal) Interferometer Response

Loop Driven	Loop in which Response Measured					
	Common mode (1)		Beam splitter (2)		Differential mode (3)	
1	1.3	1.4	2.0×10^{-1}	1.6	1.9×10^{-2}	2.7×10^{2}
2	2.8×10^{-10}	0	2.2×10^{-5}	1.1×10^{-5}	9.5×10^{-6}	3.8×10^{-6}
3	1.9×10^{-6}	1.9×10^{-6}	2.9×10^{-3}	3.0×10^{-3}	1.0	1.0

The interferometer response to a beam splitter drive was a factor 2 to 2.5 lower than predicted for both beam splitter and differential mode degrees of freedom.[2] Part of the uncertainty in the magnitude of all the elements on this row of Table 3-4 is the relative voltage to displacement calibration for the beam splitter versus the test masses which is described by the *A* matrix. Since the common mode and differential mode both drive the test masses, there is little uncertainty associated with the relative sizes of the first and third

1. Most of the measurement uncertainty, in fact, comes from the measurement of *G*, *A* and *B* and not from the interferometer response measurements.
2. The beam splitter to common mode is given as 0 because the beam splitter could not be excited enough to give a signal in the common mode loop without disrupting the lock. This is consistent with the very weak response predicted by the theory.

rows. An additional uncertainty is that the measurement was taken near the unity gain frequency of the beam splitter and so small gain fluctuations in that servo could yield substantially larger fluctuations in its closed loop response.[1]

The factor of 10 to 10^4 difference in the common mode to beam splitter and common mode to differential mode measurement have to do with imperfections in the electronics which exploit the unique features of the common mode servo. The problem is that some small amount of the signal injected into the common mode leaks into the differential mode before being suppressed by the common mode servo. As shown in Eq. 3-34, the fractional common mode to differential mode cross coupling that occurs in the recombination coil driver module is 7.1×10^{-3}.[2] The cross coupling between the test input, which is used to inject the signal into the common mode servo, and the differential mode is 1.1×10^{-2}. Thus, our assumption in deriving Eq. 3-33 that we were driving only one servo at a time is not strictly true. In most cases this is not significant, but for the common mode drive (where we have to compensate for the additional feedback paths by multiplying by the common mode loop gain which is 2.4×10^5 at 132 Hz) this can be a significant source of error.

As an example of the size of this effect, we consider the common mode to differential mode term. A 1 V_{rms} drive into the common mode test input generated a 55.8 mV_{rms} signal in the common mode drive to the masses. Because of the direct cross coupling, the dif-

---

1. The effect of the Doppler shift described in Section 2.10 is only a factor of two correction at 132.5 Hz. Nonetheless, this correction would only serve to increase the predicted interferometer response to beam splitter motion, and thus we are still left with an order of magnitude discrepancy which is believed to be due to the uncertainties mentioned.
2. This is the as good as can be expected with 1% resistors.

ferential mode would have seen an 11 mV_{rms} drive. A 500 mV_{rms} drive produced 60.0 mV_{rms} signal in the differential mode drive to the masses, thus we would expect the cross coupling to produce a 0.13 mV_{rms} drive differentially. Thus purely from the electronic cross coupling in the recombination coil driver we would measure an interferometer differential mode response to common mode drive of 2.37×10^{-2}. After multiplying by the common mode loop gain and normalizing by the differential mode to differential mode response, this would give a common mode to differential mode element in Table 3-4 of 2.1×10^{2}. This is in reasonable agreement with the number measured, and thus it appears that the signal we are trying to measure is hidden by the much larger effect of leakage into the differential mode.

A similar argument can be constructed for the common mode to beam splitter term. The magnitude of the effect of the common mode test input signal leaking into the differential mode and then being seen at the beam splitter mixer due to differential mode to beam splitter coupling in the interferometer can be estimated by multiplying the common mode to differential mode term in Table 3-4 by the differential mode to beam splitter term. This gives 8.1×10^{-1} which together with the predicted common mode to beam splitter term gives an improved prediction of 1.0 which is reasonably close to the value observed. Thus we conclude that both of the common mode drive cross terms are dominated by cross coupling from the common mode test input to the differential mode in the recombination coil driver.

Chapter 4: Conclusion

This thesis describes the first demonstration of an optical topology in a suspended interferometer which is extensible to the initial LIGO and VIRGO gravitational wave interferometers. Previous efforts at operating a suspended, recombined interferometer did not include Fabry-Perot arm cavities [38] or used hybrid signal extraction schemes where light from each arm was still detected independently [39][40]. The hybrid schemes are closer in similarity to the previous configuration of the 40-m interferometer than to this work. In the recombined configuration described here, three of the four degrees of freedom that will ultimately be needed were shown to be controllable, near the level of precision required in these interferometers. Lock acquisition was shown experimentally to be a tractable problem.

The emphasis of this work was quite different from earlier tabletop demonstrations of recycled interferometers. Rather than demonstrating the general feasibility of the asymmetric control scheme, the focus here was on understanding and accurately modeling the limitations to interferometer performance. To do this, some additional formalism was developed to treat shot noise, contrast defect, and demodulation phase errors. This formalism has since been used in designing a recycled configuration for the 40-m interferometer in addition to recombination. It was also realized that previous calculations of the interferometer response to beam splitter motion did not include the effect of the Doppler shift of reflected light, although this effect did not prove to be particularly important.

Most of the experimental results were well described by the initial modeling of the recombined interferometer, although there were surprises. Following our expectations, the interferometer sensitivity was not limited by shot noise on the symmetric photodiode, by

frequency and intensity noise of the light or by beam splitter motion. The empirical estimate of the effect of shot noise on the antisymmetric port photodiode was consistent with our calculations. The reasonable agreement between calculated and measured interferometer response functions confirmed our theoretical understanding of the asymmetry signal extraction scheme.

There is still room for improvement in reducing the uncertainty of these experimental results to provide a finer test of the theory. The calibration of the beam splitter drive voltage to displacement may be improved to give a better measurement of the beam splitter rms motion, and to enable a better comparison with theory for the interferometer response to beam splitter motion. There will soon be an opportunity to do this as the east vertex test mass suspension has been replaced with an improved version which allows longitudinal drive of this mass.

The major limitation to the comparison between measured and calculated interferometer response functions was that the common mode feedback signal was measured at the drive to the test masses which had a gain far less than unity at the frequency of the measurement. This prevented us from accurately measuring the differential mode response to a common mode drive. However, an independent measurement of the common mode contribution to the differential mode noise showed that it was at least 35 dB less than the observed noise. Thus we conclude that despite our inability to accurately measure this matrix element, it is not large enough to limit the performance of the interferometer.

The measurement of the interferometer response to common mode motion could be improved by measuring the common mode feedback signal in a high gain feedback path. (The feedback paths of the common mode servo are described in detail in Appendix E.)

This was not done because a voltage to displacement calibration was only available for feedback to the test masses, but with some effort a calibration could be obtained either for the feedback path to the reference cavity piezoelectric transducers or to the laser loop directly. The voltage to displacement calibration of the reference cavity transducers is available. This calibration can be converted to an equivalent frequency shift of the light as the laser loop ensures the laser light is always on resonance in this cavity. This frequency shift can then be converted to an equivalent amount of test mass displacement. As a check of this calculation, or to calibrate the signal to the laser loop directly, the following experiment could be performed. With one arm of the interferometer misaligned and the common mode servo disabled, the other arm could be locked with the differential mode servo. Then by driving either the reference cavity transducers or the laser loop directly and comparing with the differential mode feedback signal to the test mass (to maintain the arm on resonance), the calibration can be obtained.

Perhaps the largest surprise of the experimental program, and certainly the most pleasant, was the ease of lock acquisition. The fact that the beam splitter and common mode servo could adequately control the beam splitter and one arm of the interferometer while the other arm was swinging through resonance was not anticipated and made the task much easier. It was fortuitous that our initial attempts at lock acquisition were in a state of poor mode matching into the arms. The sign reversal of the beam splitter control signal at lower modulation depths when moving from one arm in lock to both arms in lock was not appreciated before the experiment. This might have significantly complicated the process of lock acquisition initially, had the mode matching been better.

Another issue that was not fully appreciated before the experimental program began

was the difficulty with alignment for good contrast defect. Interferometer imperfections (including spatially nonuniform mirror losses, unbalanced losses in the two arms and scattering into very high order resonant modes) made it impossible to independently optimize the power circulating in the two arm cavities and minimize the light at the antisymmetric port. Valuable experience was gained in how to align the interferometer, since the quality of the interference at the antisymmetric port was important for the first time in this configuration. A scheme developed at MIT to sense the phase gradient of the wavefront may make this easier in the future. Although average contrast defects of 3% were achieved with careful alignment, this was higher than the 1% contrast defect that was projected before the experiment. After more careful consideration of all the imperfections in the interferometer that contribute to contrast defect, most of this discrepancy was explained.

A large concern before the start of the recombination program was the very large off-diagonal elements in the matrix of discriminants. The imbalance in beam splitter reflectivity and transmission and unequal losses in the two arms mixed the common and differential mode signals to a larger extent than in the tabletop prototype. The responses of the arm cavities in the tabletop prototype was dominated by the large (3%) transmission of the input mirrors, while in the recombined 40-m interferometer they were dominated by the losses in the arms which showed more variability.[1] In addition, the low sensitivity to beam splitter motion in the signal used to control it raised serious concerns about the effects of shot noise and cross coupling with the common mode signal. All of these effects were carefully treated in calculations beforehand, and the prediction that these effects would not seriously degrade the interferometer performance was generally confirmed.

---

1. When the 40-m interferometer is converted to a recycled configuration, this will no longer be true as larger transmissions will be used for the vertex test masses.

There is one outstanding unresolved issue: what was limiting the interferometer sensitivity above 500 Hz with the original laser system? The fact that the interferometer was not shot noise limited was a mystery as no other noise source was found at the time to explain it. The interferometer noise was shown to be approximately a factor of two above the limit from shot noise on the antisymmetric photodiode. It was unfortunate that further work on this part of the frequency band was hampered by the replacement laser system whose higher intensity noise limited the interferometer sensitivity above 500 Hz. A prime candidate to explain this excess noise is scattered light, most likely in the vertex area. For instance, additional light that is scattered onto the antisymmetric photodiode and provides a spurious interferometer path may be one possible mechanism to explain the noise. There is circumstantial evidence to support this view. In laying out the optical paths to the photodiodes, it was found that the interferometer noise was raised by the insertion of a lens in front of the antisymmetric port photodiode, and that additional steering mirrors to these diodes could similarly affect the noise. Also, in measuring the amplitude of the modulation sidebands at the antisymmetric port with a Fabry-Perot optical spectrum analyzer, it was found that reflecting light back into the interferometer raised the overall noise level significantly with a spectral shape similar to the observed noise at high frequencies. In fact, any white noise source at the antisymmetric port photodiode would have this spectral shape after being filtered by the servo loop and readout filters.

Further work on this issue will occur as part of the program to convert the 40-m interferometer to a recycled configuration which is underway. The recycled interferometer will have a very different optical configuration in the vertex area to make room for the recycling mirror. If scattering is providing a mechanism for the additional interferometer

noise, we expect that this effect should be changed significantly in the new configuration.

In addition to the unresolved question of the excess noise, the recycled interferometer will provide exciting opportunities to answer new questions. Understanding the lock acquisition process in this configuration presents the largest problem. The sign reversal of the beam splitter control signal is a particular concern which was only appreciated due to our experience from recombination. A suspended, recycled interferometer will also provide the first chance to compare the frequency dependence of the matrix of discriminants with that expected from theory in a frequency region where there is interesting behavior expected. In the recombined interferometer the frequency dependence was fairly simple, but the addition of the recycling mirror adds the complication of multiply-coupled cavities.

It could be said that the primary goal of this work was to establish that many of the problems of operating an interferometer similar to the proposed initial LIGO detectors were tractable. It is the author's belief that in this we have succeeded.

Appendix A: Mirror Losses

An important input for optical design of any interferometer is a reasonable estimate of the test mass mirror losses as used in the 40-m interferometer. In many of the calculations to follow, this will be an important parameter. Measurements of the losses can be made on the table top before installing the test masses into the interferometer, but some allowance must be made for the larger spot size with 40-m cavity lengths and for the potential of optical contamination in the 40-m interferometer vacuum system. Using data taken on the table top to estimate the performance of the test masses once installed in the 40-m interferometer is the focus of this chapter.

The method by which mirror losses are typically determined in a high finesse Fabry-Perot cavity is by measuring the storage time for light injected into the cavity using the "ringdown" technique. [42] This technique consists of building up a resonant field inside the cavity and then shutting off the power incident on the cavity and observing the time scale of the exponential decay of the light leaking out of the cavity. The time it takes the leakage power to decay to 1/e of its initial value is the energy storage time of the cavity given by

$$\tau_e \approx \frac{2l}{cL_{cav}} \qquad \text{A-1}$$

where l is the length of the cavity, c is the speed of light and L_{cav} is the (small) cavity round-trip loss including absorption and scattering as well as transmission. With an independent measurement of the transmissions of both cavity mirrors, the total losses for the two mirrors can be found. By using a mirror whose loss is known as one mirror of the Fabry-Perot cavity, losses of individual mirrors can be measured.

A.1 Scaling Scattering with Size

Using the ringdown technique on one inch mirrors on the table top, total mirror losses, including scattering and absorption, of less than 10 ppm have been measured. For test masses, total mirror losses of 18-45 ppm have been achieved. The only mirror loss mechanism which one expects to scale with spot size is scattering. The importance of very small angle scattering increases with cavity length. The excess scattering losses expected when these mirrors are used in a 40 m length cavity is discussed below.

Surface profile data on a coated monolithic test mass has been taken by Zygo. Some representative data from the center of one of the vertex test masses is shown in Figure A-1. Notice that the amplitude of deviations with longer length scales is much larger than the smaller scale deviations. This data was compiled by R. Weiss into the surface height power spectral density (PSD). Here we decompose the surface profile into a sum of sinusoidal surfaces so that the PSD gives the squared amplitude of the sinusoidal surface at each wavenumber.[1] By assuming that the surface is isotropic, we can transform our one-dimensional picture of a sum of sinusoidal surfaces into the equivalent two-dimensional PSD. Each sinusoidal surface component of the two-dimensional PSD we treat as a phase grating which scatters into its first order spot. By integrating over all appropriate wavevectors, one can determine the scattering losses.

A.2 Surface Height PSD

From interferometric data we have a surface height profile, $h(x,y)$, giving us the sur-

1. Note that for the scattering discussion to follow in this chapter, we shall use the non-standard definition that $k = 1/\lambda$, where k is the wavenumber and λ is the wavelength.

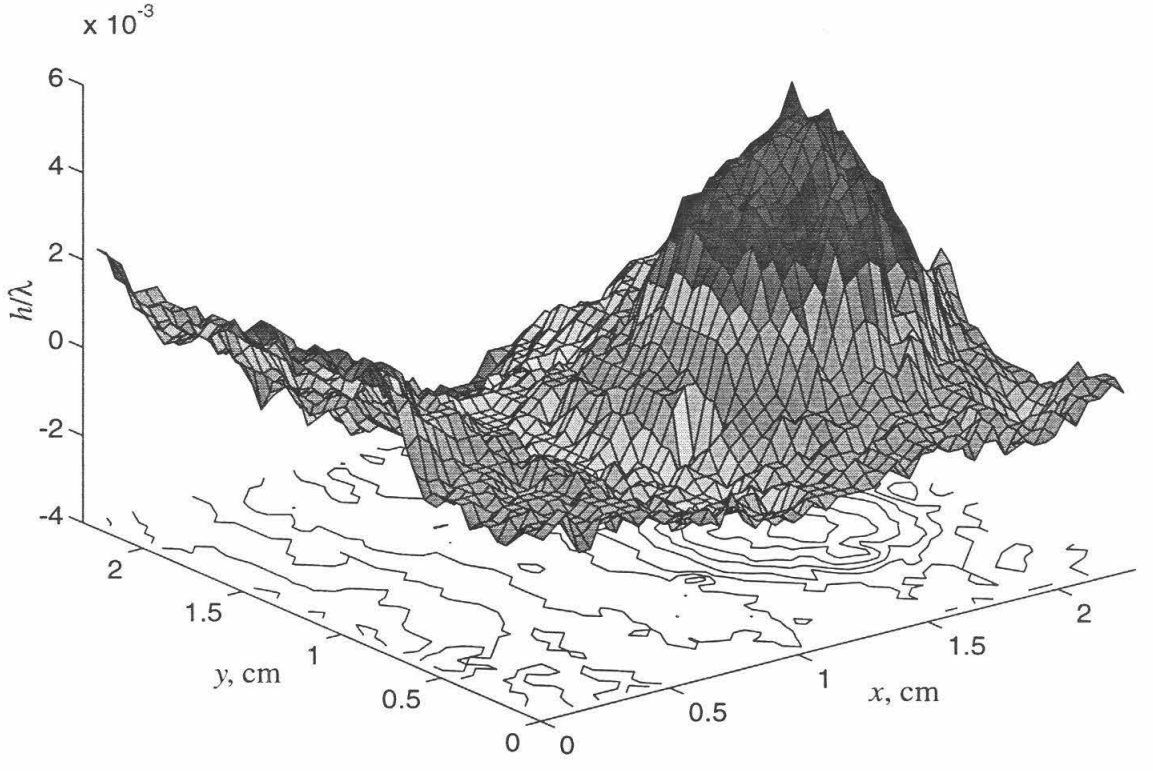

Figure A-1: Surface height profile of center of vertex test mass.

face height at points along the mirrored surface of the test mass. For each value of y we decompose this into it a collection of sinusoidal surfaces in x by finding the one-sided, one-dimensional PSD,[1]

$$H_1(k_x, y) = \frac{2}{L}\left|\int_{-L/2}^{L/2} h(x, y)\, e^{-i2\pi(k_x x)}\, dx\right|^2 \qquad \text{A-2}$$

Averaging over all such slices, we get $\overline{H_1}(k_x)$. This gives us the squared amplitude of

1. The two-sided PSD used by some authors is symmetric about zero and defined for positive and negative frequencies. Here we use the one-sided PSD which is defined only for positive frequencies and is a factor of two larger than the two-sided PSD.

each sinusoidal surface, with spatial frequency k_x, per unit of k_x.

Of course the two-sided, two-dimensional PSD,

$$H_2(k_x, k_y) = \frac{1}{L^2}\left|\int_{-L/2}^{L/2}\int_{-L/2}^{L/2} h(x, y)\, e^{-i2\pi(k_x x + k_y y)}\, dxdy\right|^2 \qquad \text{A-3}$$

is probably a more natural way to characterize the surface. Unfortunately the two-dimensional PSD is rather clumsy to deal with computationally. It turns out, as we shall see, that the one-dimensional PSD is equivalent and contains the same information as the two-dimensional PSD in the special case that the surface is isotropic. This is the assumption that we make here.

Measurements were made to find the surface height PSD for the test mass and for a Zygo reference flat. These are plotted in Figure A-2. Since the PSD for the test mass and Zygo reference flat are very nearly the same, we can only treat these values as an upper bound. In fact, in data taken sequentially with the same test flat, the repeatability was worse than 10^{-6} (waves at 514.5 nm)^2/cm^{-1} at $k_x = 0.5$ cm^{-1} and 10^{-7} (waves at 514.5 nm)^2/cm^{-1} at $k_x \geq 6$ cm^{-1}. Nonetheless, we can set a useful upper bound on the surface scattering from these data.

To use the surface height PSD data in calculations, it is easiest to approximate it with a fitted curve. The K-correlation model is commonly used for this purpose. For a one-dimensional PSD it is given in terms of the fitted parameters A, B and C by

$$H_1(k_x) = \frac{A}{[1 + (Bk_x)^2]^{C/2}} \qquad \text{A-4}$$

Fitting by eyeball, I have approximated the data to a K-correlation in two sections. These

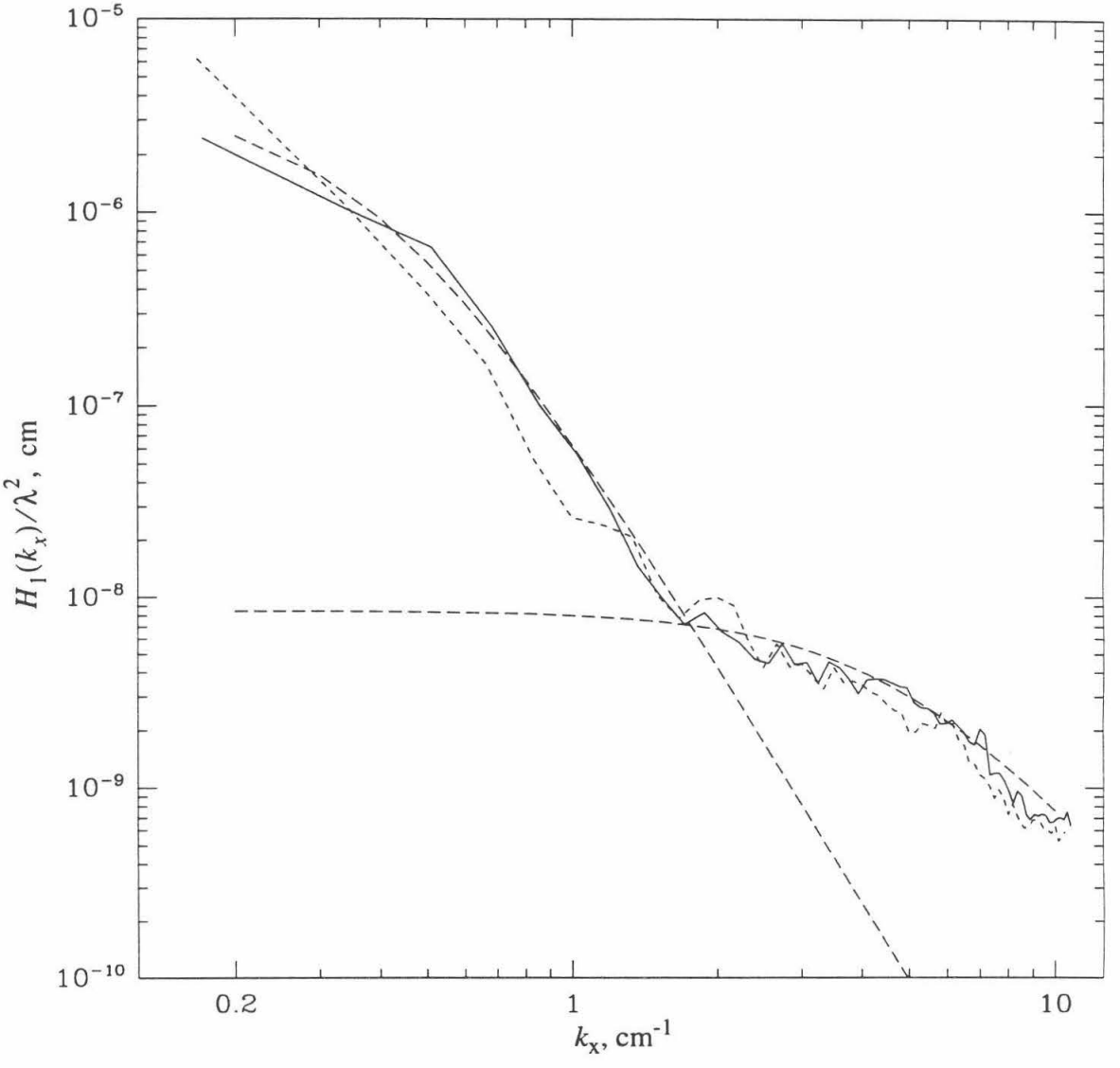

Figure A-2: PSD of surface heights measured for test masses (solid) and reference flat (dotted) with K-correlation fits (dashed).

fitted functions are shown on Figure A-2. The parameters for the fits are shown in

Table A-1.

Table A-1: Parameters for K-correlation Fits

Section	A, cm	B, cm	C
$k_x < 1.7$ cm^{-1}	8.0×10^{-6}	2.5	4.2
$k_x > 1.7$ cm^{-1}	1.7×10^{-8}	0.2	3.0

A.3 Scattering Angular Dependence

The fraction of the incident power (from direction i) scattered through solid angle $d\Omega_s$ in direction s is: [44]

$$\frac{1}{P_i}\frac{dP}{d\Omega_s}d\Omega_s = \frac{16\pi^2}{\lambda^4}\cos\theta_i\cos^2\theta_s\, Q\, H_2(k_x, k_y)\, d\Omega_s \qquad \text{A-5}$$

where Q is a function of the surface's dielectric constant and the angles of incidence and scatter which takes on different forms depending on the incident and scattered polarization states. [45] At normal incidence and small scattering angles, if we are insensitive to the polarization of the scattered light, $Q \approx 1$. (Light scattered outside the beam is lost whatever its final polarization state.) Thus scattering in the s direction (specified by θ_s and ϕ_s) is proportional to $H_2(k_x, k_y)$ evaluated at

$$k_x = \frac{\sin\theta_s\cos\phi_s - \sin\phi_i}{\lambda}$$
$$k_y = \frac{\sin\theta_s\sin\phi_s}{\lambda} \qquad \text{A-6}$$

There is a one-to-one relationship between spatial frequencies and scattering direction.

Eq. A-5 is essentially independent of the model used to describe the interaction between light and the surface as long as the surface profile measurements are made at the same wavelength as the predicted scattering. [43] This is because the surface profile was generated by measuring the optical phase of light reflected from the surface directly and converting it to the surface roughness. It is actually the phase and not the surface profile which is relevant in scattering calculations. So at the wavelength which the phase is measured, we can apply Eq. A-5 with high confidence.

To find the scattering from a general surface, we must have the two-dimensional PSD. Since we have expressed our mirror surfaces in terms of one-dimensional PSD's, we need to be able to convert these to two-dimensional PSD's. In general this is not possible, since the one-dimensional PSD does not contain all the information of the two-dimensional PSD. In particular,

$$H_1(k_x) = 4 \int_0^\infty H_2(k_x, k_y)\, dk_y \qquad \text{A-7}$$

Two exceptions to this are grating-like surfaces and isotropic surfaces. For grating-like surfaces,

$$H_2(k_x, k_y) = \frac{1}{4} H_1(k_x)\, \delta(k_y) \qquad \text{A-8}$$

Isotropic surfaces can be described by a single variable, $k = \sqrt{k_x^2 + k_y^2}$. To solve for isotropic surfaces, we substitute

$$k_y = \sqrt{k^2 - k_x^2}$$
$$dk_y = \frac{k}{\sqrt{k^2 - k_x^2}}\, dk \qquad \text{A-9}$$

into Eq. A-7.

$$H_1(k_x) = 4 \int_{k_x}^{\infty} \frac{k\, H_2(k)}{\sqrt{k^2 - k_x^2}}\, dk \qquad \text{A-10}$$

This can be solved for $H_2(k)$, yielding an Abel transform: [46][43][47]

$$H_2(k) = -\frac{1}{2\pi} \int_{k}^{\infty} \frac{dH_1(k_x)}{dk_x} \frac{dk_x}{\sqrt{k_x^2 - k^2}} \qquad \text{A-11}$$
$$\equiv \mathbf{A}[H_1](k)$$

Conveniently, the Abel transform of a K-correlation has already been done for us. [48][43]

$$H_2(k) = \frac{A'}{[1 + (Bk)^2]^{(C+1)/2}}$$
$$A' = \frac{\Gamma[(C+1)/2]}{2\sqrt{\pi}\,\Gamma(C/2)}\, AB \qquad \text{A-12}$$

where A, B and C are the values obtained from the one-dimensional K-correlation fit. Unfortunately, we can not blindly apply this formula since we fit the one-dimensional PSD with two K-correlations for different sections. The Abel transform, $\mathbf{A}[H_1](k)$, depends on $H_1(k_x)$ at all spatial frequencies higher than k. With a little manipulation it is easy to show that for a one-dimensional PSD fit in two sections, such as

$$H_1(k_x) = \begin{cases} H_A(k_x) & k_x > k_A \\ H_B(k_x) & k_x < k_A \end{cases} \qquad \text{A-13}$$

that the corresponding two-dimensional PSD is

$$H_2(k) = \begin{cases} A[H_A](k) & k > k_A \\ A[H_B](k) + A[H_A](k_A) - A[H_B](k_A) & k < k_A \end{cases} \qquad \text{A-14}$$

A.4 Gaussian Beams

The scattering theory described above is strictly only true for plane waves. To apply this theory to a mirror in a Fabry-Perot cavity, we need to make some approximations. The eigenmodes of a Fabry-Perot cavity are almost exactly given by the Hermite-Gaussian functions. We are principally concerned with the lowest order mode, the so-called TEM_{00} mode, which is cylindrically symmetric. We approximate the TEM_{00} mode as being composed of a sum of plane waves. Note that locally at every mirror surface the plane wave components are normal to the surface as the radius of curvature of the Gaussian eigenmode must match that of the mirror surface. Because the spot size is very small compared to the cavity length, the scattering angular distribution for the sum of plane waves will not be much different from that of a single plane wave. The critical assumption is that the fraction of light which is scattered outside the beam from one reflection is the fraction lost due to scattering.

The beam divergence angle of a Gaussian beam is

$$\theta_D = \frac{\lambda}{\pi w_0} \qquad \text{A-15}$$

where w_0 is the cavity waist radius. Any light scattered inside this angle we say is still inside the beam and is not lost due to scattering, while that scattered outside this angle is lost. There is a corresponding beam divergence wavenumber, corresponding to the lowest spatial frequency which scatters outside the beam. Since the beam divergence angles are typically small, we approximate

$$k_D \approx \frac{\theta_D}{\lambda} \qquad \text{A-16}$$

It is instructive to calculate typical beam divergence angles of various cavities. Table A-2 gives three sample cases: a short Fabry-Perot cavity such as may be used in table-top experiments, an arm cavity of the 40m interferometer, and an arm cavity in LIGO.

Table A-2: Beam Divergence Angles and Wavenumbers for Standard Cavities

Cavity	w_0	l	θ_D, rad	k_D, cm^{-1}
Short	0.2 mm	50 cm	8.19×10^{-4}	15.9
40 m	2.2 mm	40 m	7.44×10^{-5}	1.45
LIGO	2 cm	4 km	8.19×10^{-6}	0.16

Thus, in principle to find the total scattering losses, we should integrate from $\theta_1 = \theta_D$ to $\theta_2 = \frac{\pi}{2}$, or from $k_1 = k_D$ to $k_2 = \infty$. Unfortunately, we have no data for high wavenumbers. We can use the fact, however, that our scattering losses for short cavities are 45 ppm or less. Then by integrating from the beam divergence angle for short cavities to that for the 40-m interferometer, we can calculate the additional scattering losses incurred.

A.5 Results of Scattering Calculations

We now have a prescription for estimating the scattering losses due to surface roughness for mirrors in a Fabry-Perot cavity. The one-dimensional, one-sided PSD of the surface profile is taken. This is fit to a K-correlation which can be easily transformed into the equivalent two-dimensional PSD form under the assumption that the surface is isotropic.[1] One then integrates over the appropriate range of spatial frequencies to obtain the scattering loss for a mirror used in a particular Fabry-Perot cavity. The dependence of scattering loss on cavity length is contained in the choice of the limits of integration.

Using Eq. A-12 and Eq. A-14, we convert our fitted one-dimensional PSD to its equivalent two-dimensional form:

$$\frac{H_2(k)}{\lambda^2} = \begin{cases} \dfrac{1.08\times10^{-9}}{[1+(0.2k)^2]^2} & k > 1.7 \\ \dfrac{7.70\times10^{-6}}{[1+(2.5k)^2]^{2.6}} - 2.74\times10^{-9} & k < 1.7 \end{cases} \qquad \text{A-17}$$

We need to integrate Eq. A-5 to find the total light scattered through some range of angles. We can assume normal incidence. The fraction of light scattered between angles θ_1 and θ_2 is

$$\begin{aligned} S_{12} &= \int_0^{2\pi}\int_{\theta_1}^{\theta_2} \frac{1}{P_i}\frac{dP}{d\Omega_s}\, d\Omega_s \\ &= 16\pi^2 \int_{k_1}^{k_2}\int_{k_1}^{k_2} \frac{H_2(k_x, k_y)}{\lambda^2}\, dk_x\, dk_y \end{aligned} \qquad \text{A-18}$$

1. A particular mirror's surface profile will generally not be isotropic, but we assume that the average surface profile of a number of similar mirrors is isotropic.

where we have used $dk_x dk_y = d\Omega_s \cos\theta_s / \lambda^2$. Since the two-dimensional PSD is isotropic, it is most convenient to convert this integral to polar coordinates (k, β).

$$\begin{aligned} S_{12} &= 16\pi^2 \int_{k_1}^{k_2} \int_{0}^{2\pi} \frac{H_2(k)}{\lambda^2} k\, dk\, d\beta \\ &= 32\pi^3 \int_{k_1}^{k_2} \frac{H_2(k)}{\lambda^2} k\, dk \end{aligned} \qquad \text{A-19}$$

In the arm cavities of the 40-m interferometer, the additional scattering losses are:

$$\begin{aligned} S_{12} &= 32\pi^3 \int_{1.45}^{15.9} \frac{H_2(k)}{\lambda^2} k\, dk \\ &= 32\pi^3 \left[\int_{1.45}^{1.7} \left(\frac{7.70\times10^{-6} k}{[1 + (2.5k)^2]^{2.6}} - 2.74\times10^{-9} k \right) dk + \int_{1.7}^{15.9} \frac{1.08\times10^{-9} k}{[1 + (0.2k)^2]^2}\, dk \right] \\ &= 12 \text{ ppm} \end{aligned} \qquad \text{A-20}$$

This upper bound on the additional loss is tolerable, and maybe noticeable.

For comparison we can calculate the additional scattering losses for LIGO arm cavities assuming the LIGO test masses had the same surface roughness as the current monolithic test masses.

$$\begin{aligned} S_{12} &= 32\pi^3 \int_{0.16}^{1.45} \frac{H_2(k)}{\lambda^2} k\, dk \\ &= 32\pi^3 \int_{0.16}^{1.45} \left(\frac{7.70\times10^{-6} k}{[1 + (2.5k)^2]^{2.6}} - 2.74\times10^{-9} k \right) dk \\ &= 290 \text{ ppm} \end{aligned} \qquad \text{A-21}$$

This is in addition to the scattering losses expected for a 40-m arm cavity. The much larger losses for larger spot size arise from the very large amplitude, low spatial frequency com-

ponents of the surface height PSD. It is an ongoing task within the LIGO Project to have mirrors developed with surface figure superior to this.

An overlap integral can also be used to estimate the scattering from the mirror surface. The eigenmodes of a cavity whose mirrors have small surface height variations are very close to the TEM_{xy} modes of an ideal cavity. The amount of light scattered out of the fundamental mode is approximately

$$S = 1 - \left| \int_{-\infty}^{\infty} \int_{-\infty}^{\infty} E_{00}{}^{*}\, e^{i2kh(x,y)}\, E_{00}\, dx\, dy \right|^2 \qquad \text{A-22}$$

where E_{00} is the complex field amplitude of the TEM_{00} mode. This method will not work well for spots sizes in the 40-m arm cavities as we have only four surface height data points inside the waist. We can use this method, however, as a useful check for larger spot sizes. After removing the effect of tilt, a LIGO size spot on the 40-m test masses had an overlap integral loss of 385 ppm. This is still an overestimate as the net curvature of the surface has not been removed which will not give scattering, but there is reasonable agreement between the overlap integral and the 347 ppm[1] scattering losses estimate calculated with the method described above.

A.6 Contamination of Mirrors in Vacuum

We must also be concerned with contamination of the optical surfaces in vacuum. [49] Elastomers are often desirable for inclusion in vacuum systems either as seals or for

1. This comes from a 45 ppm limit on the scattering losses over 1 m cavity lengths, a 12 ppm limit on the additional losses incurred in going from 1 m to 40 m, and 290 ppm in going from 40 m to 4 km.

their mechanical properties. In the 40-m interferometer they are used as part of the vibration isolation system [50] and as seals for all of the large aperture flanges. There has been some concern that these materials may contaminate mirrors in vacuum, and to address this concern a table top experiment was constructed to set quantitative limits on the contamination rate.

Previous research in this area has focused on measuring outgassing and deposition kinetics, primarily for certifying materials as acceptable for spacecraft use. [51] Predicting the change in optical properties from the amount of surface contaminant is difficult.

We attempted to avoid these difficulties by measuring optical degradation directly, at room temperature and at pressures and time scales relevant for gravitational wave detectors. Sample elastomers have been tested by placing a specimen in a cleaned and baked vacuum chamber with a high finesse Fabry-Perot cavity. Except for the specimen, only metal and glass were used inside the vacuum chamber. The chamber was then evacuated and the losses in the Fabry-Perot cavity were measured periodically using the ringdown technique. Changes in the absorption and scattering of the mirrors were inferred from the measured changes in the storage time.

A.7 Vacuum Contamination Test Setup

Three test cavities were used, each in a separate vacuum chamber. One was used as a control with no specimen in the chamber; one was exposed to RTV-615 silicone rubber; and one was exposed to Fluorel. Over a period of several months, we noticed little change in the mirror losses, indicating that these materials may be used in vacuum systems with low loss mirrors.

The optical cavities consisted of two 110 ppm (nominal) transmission mirrors. The input mirror was flat while the other had a 50 cm radius of curvature. They were held 29.1 cm apart by an aluminum spacer, which was suspended using 150 μm diameter wires for vibration isolation. The entire spacer assembly was constructed of aluminum except for the steel wires, stainless-steel screws and balls on which the mirrors rested, and beryllium-copper springs. The spacer had a slot where a specimen could be placed in close proximity (less than 5 cm) to the input mirror.

Each vacuum chamber was a 20 cm diameter, 66 cm long tube, constructed of stainless-steel with Kovar-sealed Pyrex windows at both ends. Before installing the mirrors, beryllium-copper springs and the specimen, the vacuum chamber and all other components were vacuum baked at 190 °C for 24 hours. The beryllium-copper springs were unavailable at the time of the initial bake and were instead baked in air at 200 °C for 48 hours. The vacuum chamber was evacuated through a turbomolecular pump to reduce potential backstreaming of pump oil from the rotary vane roughing pump. An 8 L/s ion pump attached to the chamber was started when the chamber pressure dropped below 10^{-5} Torr. After the initial surge of ion pump current, an all-metal valve was used to isolate the chamber from the roughing pump and the mechanical pumps were removed. In this way pressures below 10^{-8} Torr were achieved and maintained, except for the chamber containing Fluorel, which only achieved 2×10^{-7} Torr due to the high outgassing load from the specimen.

The specimens were prepared and handled carefully before being inserted into the test chambers. The fluoroelastomer specimen was a single piece of 3M-Fluorel 2176 (70 durometer) molded into a truncated cone, 5 cm high, 4 cm in diameter at the base and 3 cm

in diameter at the top. It was cured by the manufacturer for 25 minutes at 180 °C and was not postcured.[1] After we received the part from the manufacturer, it was baked in vacuum for 46 hours at 110 °C.[2]

The RTV specimen consisted of six pieces of RTV-615 silicone rubber. Each one was a cylinder 1 cm in diameter and 1 cm in height. After casting, these were soaked in methylene chloride for 5 days with the solvent changed twice. The RTV pieces were then baked in vacuum for 90 hours at 200 °C.

A diagram of the experimental apparatus is shown in Figure A-3. An argon-ion laser was used as the light source for the mirror loss measurements. Feedback to a Pockel's cell inside the laser cavity locked the laser frequency to the test cavity modes for times on the order of 0.1 ms. The feedback loop derived its error signal from the light reflected from the cavity using the RF reflection locking technique. [52] When the light transmitted through the cavity reached a preset trigger level, an acousto-optic modulator was used to completely shut off the light incident on the cavity. At the same time a storage scope began recording the output of a photodiode monitoring the light that leaks out of the cavity. Typically 32 such decay transients were averaged together. The data were then fit to an exponential of the form:

$$V = A + B\exp\left(-\frac{t}{\tau_e}\right) \qquad \text{A-23}$$

---

1. Postcuring is a process which is used to remove some volatile materials from Fluorel after it is cured. It is normally used with O-rings, for example.
2. After the experiments described in this paper were performed, we developed a better method of cleaning Fluorel which significantly decreased its outgassing. After being cured it was postcured by baking it in air at a temperature which is ramped from 80 °C to 230 °C over a period of 46 hours. The slow ramp was necessary to avoid cracking the Fluorel piece. It was then baked at 230 °C for 14 hours. After cooling, the Fluorel piece was vacuum baked for 10 days at 200 °C.

The resulting τ_e is the energy storage time which is used to calculate the total cavity loss using Eq. A-1. The light trigger level was set so that only the storage time of the TEM_{00} mode was measured. Ten such measurements (each representing the average of 32 decay transients) were made and averaged to provide an estimate of the measurement uncertainty.

A.8 Results of Vacuum Contamination Test

A plot of total cavity loss versus time for the control cavity and the two materials tested so far is shown in Figure A-4. The large differences in the initial losses arose from spatial nonuniformity of the mirrors. Measurements were repeated often for the first 48 hours to look for any rapid degradation. In all three cases, the losses measured immediately before pumping down were about 10 ppm higher than losses measured after one hour of pumping. This decrease is consistent with the expected decrease in Rayleigh scattering from the air in the chamber.

The results of linear fits to the data are shown in Table A-3. We do not necessarily expect a contamination effect to be linear, but a linear fit is a convenient way of quantifying trends in the data for comparisons between the three cavities. Since fluctuations in the data typically exhibited time scales of several days, only one point was retained for the fit from the initial 48 hour period in the cases of the control cavity and RTV test cavity. The Fluorel test cavity showed a decrease in losses for the first 200 hours. There are several mechanisms which could explain such an effect. For instance, the mirror coating could have absorbed water or a contaminant film could have formed on the mirror before evacuation of the chamber, which then desorbed in vacuum. Whatever the explanation, it was

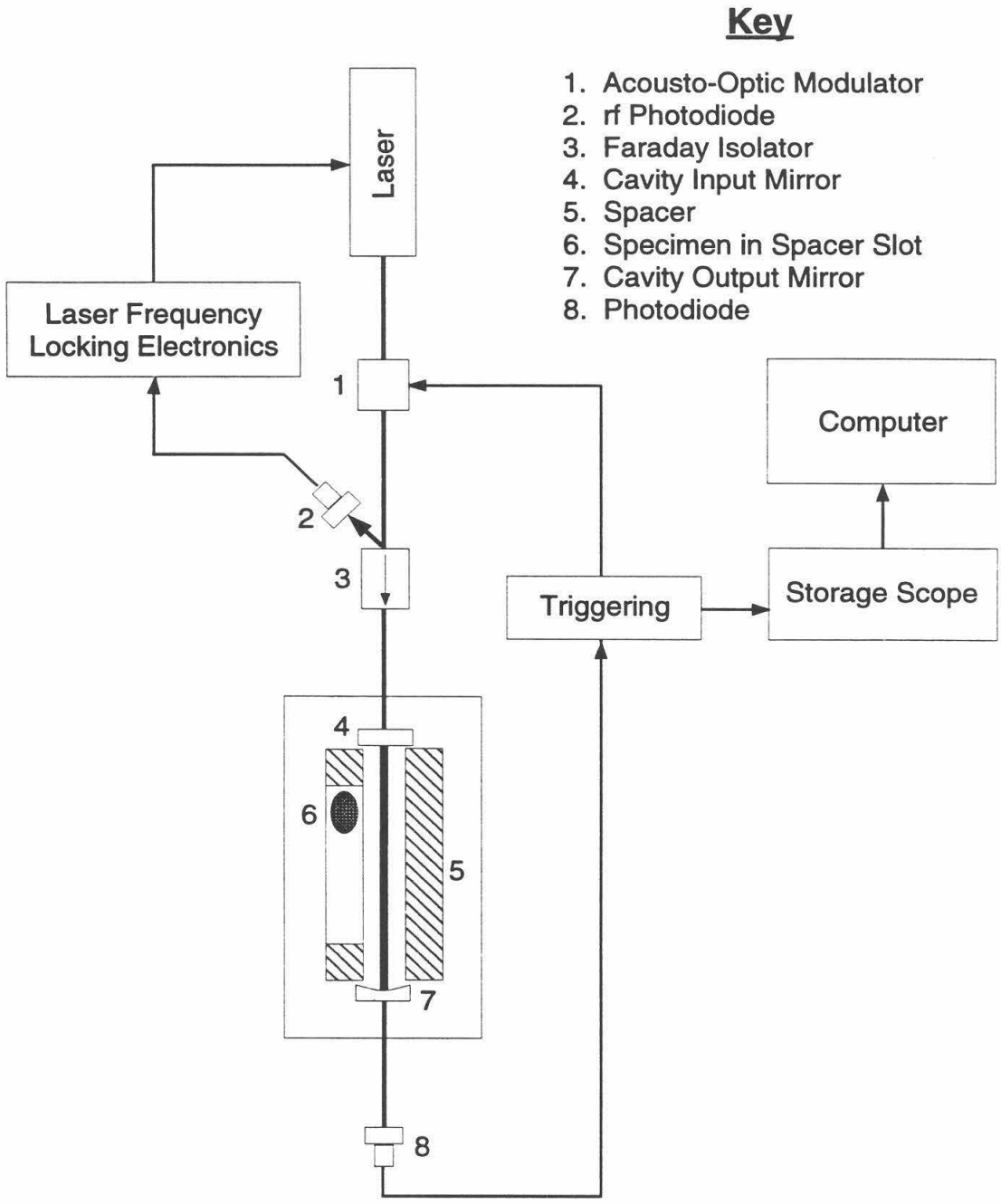

Figure A-3: Schematic diagram of the experimental apparatus for the vacuum contamination tests.

decided that the most conservative estimate of mirror degradation due to exposure to Fluorel would be obtained by starting the linear fit after the initial downward trend at 200

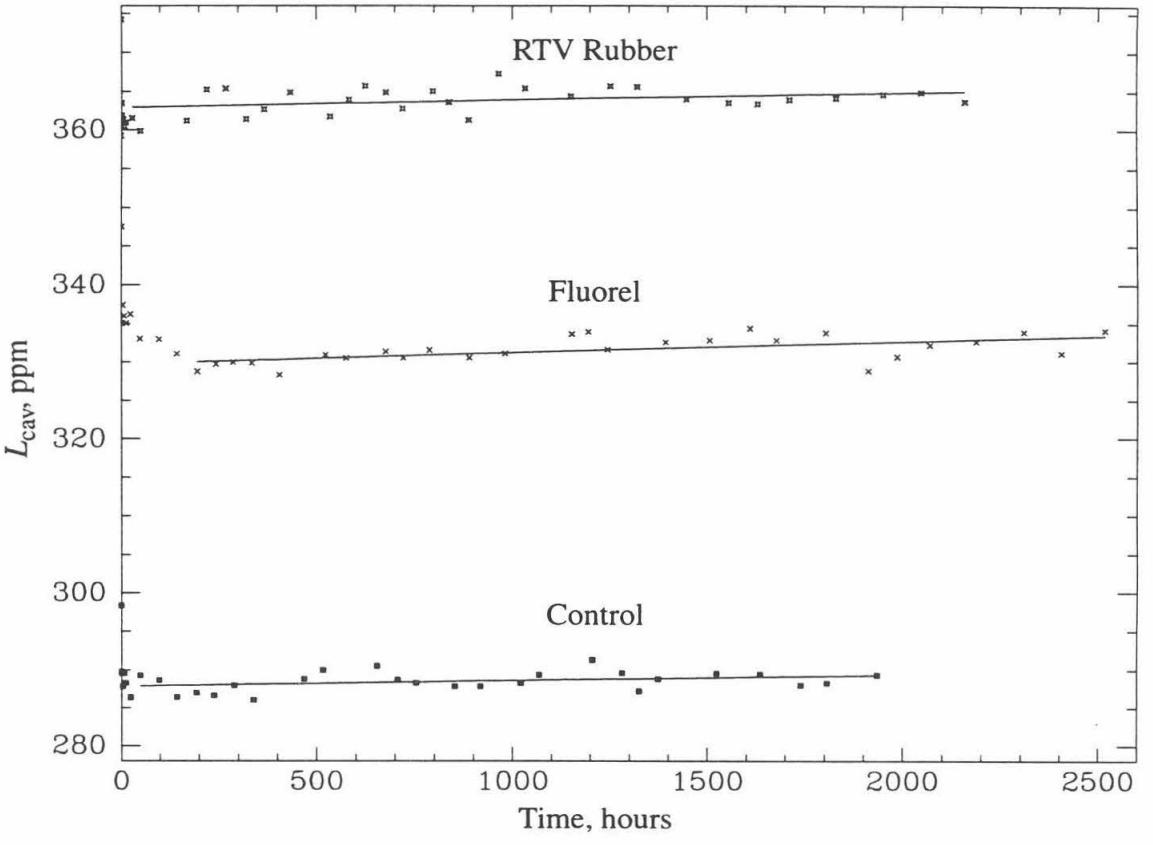

Figure A-4: Total cavity loss versus time for three test chambers with straight-line fits. The lengths of the lines indicate the regions over which the fits were taken.

hours.

Table A-3: Results of Vacuum Contamination Tests

Specimen	Rate of Increase of Losses (ppm/week)	
	Best Fit	95% Confidence Limit
Control	0.13 ± 0.07	< 0.24
Fluorel	0.25 ± 0.06	< 0.35
RTV	0.16 ± 0.08	< 0.29

In general our short-term measurement uncertainty for τ_e was much smaller than

observed day-to-day fluctuations in this parameter. We suspect the larger fluctuations resulted from movement of the spot positions on the mirrors. A small temperature change in the aluminum spacer could cause it to bend slightly in addition to changing its length. Since the waist (radius) was 0.2 mm, a small spot motion would significantly change the total losses if the mirror losses were not very uniform. In fact, mirrors tested from this coating batch typically showed factor-of-two variations in losses with position. We expect that by using better mirrors in the future, our measurements will become more accurate.

Table A-4: Results of Residual Gas Analyses

Mass	Effective Outgassing Rates (Torr L/s cm^2)		
	Fluorel (No Postcure)	Fluorel (Postcured)	RTV-615
18	1.8×10^{-9}	8.8×10^{-14}	$< 7.5\times10^{-14}$
28	3×10^{-10}	1.9×10^{-12}	$< 6.9\times10^{-13}$
44	8×10^{-12}	1.6×10^{-12}	$< 9\times10^{-14}$
All others	$< 6.8\times10^{-11}$	$< 7.3\times10^{-14}$	$< 3.8\times10^{-15}$
RGA electronic noise level	2.3×10^{-15}	1.4×10^{-16}	1.9×10^{-16}

For comparison with the optical tests, the outgassing properties of identically prepared specimens were characterized by a residual gas analyzer (RGA). The measurements were carried out in the same chamber in which the specimens were baked so that the specimens were not exposed to air between their baking and taking the spectra. The outgassing rates were calibrated by opening a calibrated N_2 leak into the test chamber.[1] Table A-4 shows the outgassing rates at various mass numbers. These outgassing rates indicate the

1. The calibrated leak itself was checked against another calibrated leak.

successful removal of volatile hydrocarbon residues by the cleaning and baking procedure. Note, however, that total outgassing rates on elastomers prepared in this way and then exposed to air before installation in a vacuum system are expected to be higher than the values in Table A-4. During exposure to air, gases are reabsorbed into the elastomers. The pressures in test chambers that contained elastomers were observed to decrease more slowly than in the control chamber because of this subsequent outgassing. This effect was far more prominent in the Fluorel sample than in the RTV sample, which we attribute to the lower permeation rate in the Fluorel specimen and the larger size of that specimen.

Within measurement errors the cavities exposed to Fluorel or RTV did not show a significantly higher rate of mirror loss increase than the control cavity. Although the best linear fit for the control cavity shows a slight loss increase, we feel it is premature to speculate on its cause given our measurement accuracy. Partially as a result of this work, these materials have been placed on a list of materials qualified to be placed in the 40-m vacuum system. Current experiments are attempting to improve the limits set for Fluorel, RTV and other materials, and to determine if continuously maintaining optical power within the cavities will increase the degradation rate.

Appendix B: Time Domain Performance of the Interferometer

Most of the characterization of the 40-m interferometer noise performance has been in the frequency domain. This is because in diagnosing servo problems or tracking down specific noise sources, the frequency domain is normally most useful. Typically less than a minute of the gravitational wave signal is fed into a commercial spectrum analyzer such as the HP 3563A which digitizes and Fourier transforms this signal to produce an estimate of the power spectrum. This method assumes the noise is stationary.

Unfortunately, this is not true for two reasons. The alignment of the optical cavities and the resulting sensitivity and noise performance drift with time.[1] Also we observe occasional, very large noise transients which are far larger and more frequent than could be expected from Gaussian statistics. LIGO will be operated continuously and be searching chiefly for impulsive signals. These large noise transients could limit the ultimate sensitivity of the detector to be substantially worse than expected from the power spectrum.

To study and hopefully ameliorate both of these effects, we have taken continuous data records which are several hours in length. By analyzing these data in the time domain, we can characterize the non-gaussian event rate and make some observations about the duty cycle and performance variability of the interferometer over longer times. The data were taken on the 40-m interferometer in its Fabry-Perot configuration before recombination. The nonstationary sources of noise that were identified we expect to be present in either configuration, and the results of early data runs on the recombined interferometer

1. Ideally only shot noise should be affected by this kind of slow drift, but imperfections in the mirrors and the alignment system can give rise to a number of noise sources which depend on the laser spot position on the mirrors.

indicate qualitative agreement with the results from the Fabry-Perot configuration. [53]

An important question to answer when determining the reduction of the interferometer's sensitivity due to nonstationary noise is for which type of gravitational wave source is the sensitivity computed? The nonstationary noise may have a frequency or time domain character that is markedly different from the signal waveform that is expected from some gravitational wave sources, and thus it will not affect the sensitivity to these signals.

There are at least three major types of astrophysical sources for gravitational waves. [54][55] These are final inspiral to coalescence of binary star systems, pulsars and other periodic sources, and supernova and other burst sources. The best understood source is coalescing binaries whose chirp waveforms have been calculated to high precision [56][57][58] and for which there are reasonable estimates of the event rate as a function of the volume of space surveyed [59][60]. Using standard optimal filtering signal analysis techniques, there is a reasonable probability that these sources will be detected by LIGO. [61][62] The gravitational waveform for pulsars is also known very precisely as it is a sine wave in a coordinate system which is at rest with respect to the sun. [63] The pulsar frequency is modulated, however, by the earth's rotation and its orbit around the sun. There is also the very slow spindown of the pulsar and occasional glitches. A complete pulsar search would involve removing the modulation and spindown and looking for narrow features in a power spectrum of the interferometer output, but this must be done for every possible source direction in the celestial sphere and for a wide range of spindown rates. To achieve the desired sensitivity one must coherently analyze long stretches of data which make this beyond the computing capabilities of modern supercomputers. Better search algorithms or faster computers may make this practical in the future. Burst sources such as

supernovae have poorly understood waveforms [64] and, as such, are hard to design search algorithms for.

Past gravitational wave searches on prototype gravitational wave interferometers, such as the 40-m interferometer, have concentrated largely on coalescing binaries [65][66] or pulsar searches [63][67][68]. It is only from these sources that any astrophysically meaningful results can be obtained, although the limits set are still orders of magnitude away from being astrophysically significant. Although the waveforms for supernova events are not well known, some types may ring for several cycles at kHz frequencies. This is markedly different from coalescing binaries where the dominant signal to noise contribution is from frequencies around 100 Hz and the signal will be in the LIGO detector's observing bandwidth for about 6 s.

The work of this thesis is principally concerned with prototyping techniques by which the shot noise limited sensitivity of gravitational wave interferometers can be improved by modifying their optical topology. It was a natural extension of this work to characterize the time domain performance of the interferometer in this frequency band and for sources that lie in this frequency band. These sources, as mentioned above, are burst sources. Because the waveforms for these sources are largely unknown, the strategy was adopted to search for a "typical" template of a single cycle of a sine wave at 1 kHz using optimal filtering techniques. In addition an effort was made to understand the sources of the nonstationary, fast transients which limit the sensitivity to our template.

B.1 Data Acquisition System

A block diagram of the data acquisition system is show in Figure B-1. Up to 16 chan-

nels of data are taken by a 12-bit, 16-channel analog-to-digital converter (ADC). Four channels are taken at 9868.42105 samples/second[1] and 12 channels are taken at 1/10th this rate. Typical channel assignments are shown in Table B-1. Because of ground loops induced by connecting the ADC to certain monitor outputs, some of these channels were not recorded during much of the data runs. A Concurrent RTU 6400 computer with 2 processors and 16 MB of memory controls the ADC and queues the digitized data to be written to an Exabyte tape, each of which has a 2 GB storage capacity. Approximately five hours of data can be written to a single Exabyte tape.

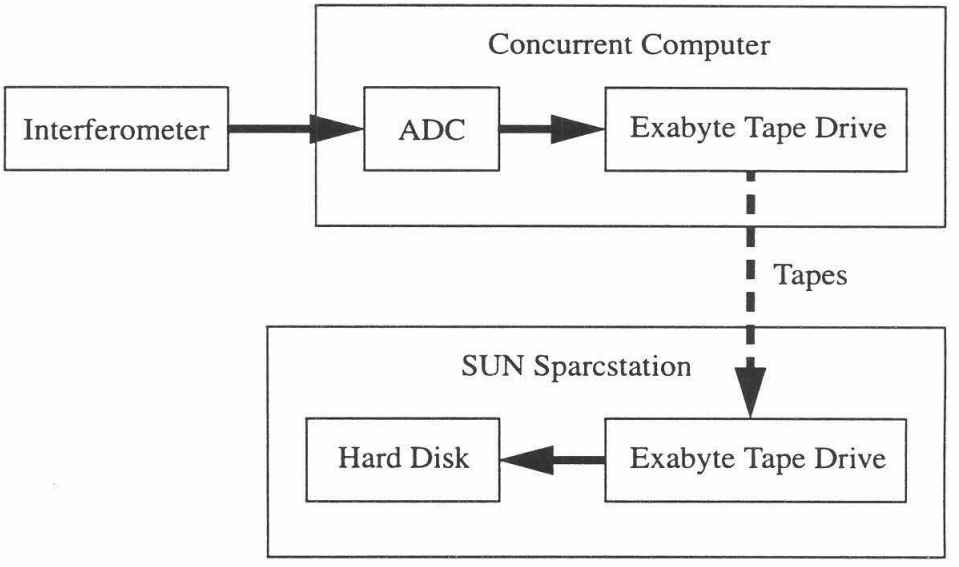

Figure B-1: Block diagram of the data acquisition system.

The tapes are later read onto a 9 GB hard disk connected to a SUN SPARCstation 10 computer which is used to do the actual analysis. The hard disk is connected to the computer via a SCSI connection to allow fast access times during data analysis and avoid net-

1. This number happens to be a convenient multiple of the computer's internal clock rate.

work delays in working with remotely served file systems.

Table B-1: Typical Channel Assignments

Channel	Signal	Filtering
0[a]	Gravitational Wave	100 Hz HP[b] (12 dB/oct.), 100-300 Hz BP (6 dB/oct.), 125-1600 Hz BP (12 dB/oct.), 4.5 kHz LP
2	Microphone	0.3-3000 Hz BP (6 dB/oct.) and 4.5 kHz LP
3	Primary Cavity Servo Preamplifier[c]	100-4000 Hz BP and 4 kHz LP
4[d]	Gravitational Wave (DC coupled)	3 kHz LP (12 dB/oct.)
5	Mode Cleaner Piezo Drive Monitor Out	none
6	Seismometer	0.03-100 Hz BP (6 dB/oct.) and 400 Hz LP
7	Laser Slow Piezoelectric Controlled Mirror Monitor	400 Hz LP
10	In Lock (TTL)	none
11	Arm 1 Visibility	none
12	Arm 2 Visibility	none
13	Mode Cleaner Visibility	none
15	Arm 1 Coil Driver Monitor	none

a. Channels 0 - 3 are fast channels taken at 9.9 ksamples/second.
b. HP indicates a high-pass filter, BP indicates a band-pass filter, and LP indicates a low-pass filter. Roll off is assumed to be 24 dB/octave unless otherwise noted.
c. This is the same module later used as the common mode servo preamplifier.
d. Channels 4 - 15 are slow channels taken at 0.99 ksamples/second.

B.2 Digitization Noise

The analog data which are digitized by the ADC are stored in binary format with a finite number of bits devoted to each sample. The effects of this finite storage register length need to be considered in shaping the pre-whitening filters and in the actual data

analysis. [69] Each digitized value represents a small range of potential analog signal levels. This uncertainty in the original signal level that is introduced in the analog-to-digital conversion process can be modeled as an additive noise signal. This derived noise signal, which we refer to as *digitization noise*, will prove to be a convenient way of analyzing the effects of the finite register length of the ADC.

There are additional finite register length effects that come about in the data analysis computations because the values are represented to finite accuracy by standard 4 byte floating point variables. We also model these effects by an additive error which we refer to as *roundoff error.* Care was taken during the calculations to consider this source of error by using methods with better numerical stability and by making empirical estimates of the rounding error by performing numerical calculations with only slightly different input parameters and checking that the results were reasonably equivalent.

To derive a form for digitization noise, let us assume that we have sampled some input signal at equally spaced points in time to arrive at the sequence $\{x(n)\}$, $0 < n < N$, where the samples are known to infinite precision. Now we pass this sequence through a quantizer, Q. Generally, either rounding or truncation must be used to represent the sequence with finite precision. The representation used for the quantized data and the method of quantization will determine the error introduced for a particular sample. However, the rms level of the additive digitization noise does not depend on these details. We consider the case of rounding where the size of each quantization step is $\Delta = 20(2^{-b})$ V,[1] where b is the number of bits used by the ADC, as shown in Figure B-2.

---

1. The acceptable input range for the ADC is ±10 V. Thus 20 V is divided up into 2^b quantization steps.

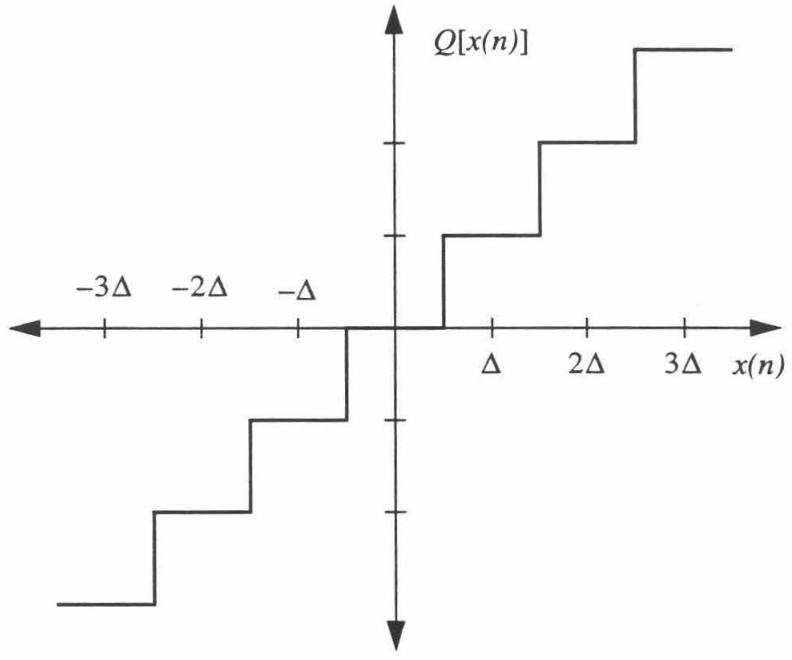

Figure B-2: Example of a rounding quantizer.

We can write,

$$Q[x(n)] = x(n) + e(n) \qquad \text{B-1}$$
$$-\frac{\Delta}{2} < e(n) \leq \frac{\Delta}{2}$$

Of course Eq. B-1 implies that we know *e(n)* exactly for every *n*. This is the error due to finite register length in the quantization process. Although this error is deterministic, we will treat it as if it were a random process and use a statistical model to describe it. In particular we make the following assumptions:

1. {e(n)} is a sequence sampled from a stationary random process.
2. {e(n)} is uncorrelated with {x(n)}.
3. The error process is a white-noise process.
4. The probability distribution function of the error process is uniform over the range of the quantization error.

There are obviously cases where these assumptions are clearly invalid, for example if the

input signal is a step function. However, if the input signal has a form such that the amplitude of the signal is likely to traverse many quantization steps in each sampling interval in a somewhat unpredictable manner, then these assumptions can be quite good. This is generally the case when other sources of noise are greater than the size of the quantization step. The gravitational wave signal is sampled with sufficiently small quantization steps that we can generally make these assumptions.

Let us calculate the rms level of digitization noise. We are assuming that the quantizer rounds so that we get the uniform probability density function shown in Figure B-3, but the result is valid for truncation as well.

$$\sigma^2 = \int_{-\frac{\Delta}{2}}^{+\frac{\Delta}{2}} e^2 \frac{1}{\Delta}\, de = \frac{1}{3\Delta} e^3 \Bigg|_{-\frac{\Delta}{2}}^{+\frac{\Delta}{2}} \qquad \text{B-2}$$

$$= \frac{\Delta^2}{12}$$

We have a 12-bit ADC with ±10 V range so that $\Delta = 4.88$ mV, thus $\sigma = 1.41$ mV. All the digitization noise power is contained in the band below the Nyquist frequency, and in this band it is white. Therefore, digitization noise is at the level 2.01×10^{-5} V/$\sqrt{\text{Hz}}$ or -94 dB.

The limited input range of the ADC conspires with digitization noise to set a limit on the maximum average signal to noise ratio measurable per sample. The largest signal that can be digitized by the ADC without distortion is 10 V. The ratio of the largest signal measurable to the digitization noise level is known as the dynamic range. The dynamic range is the highest power signal to noise ratio achievable because of digitization noise. In this

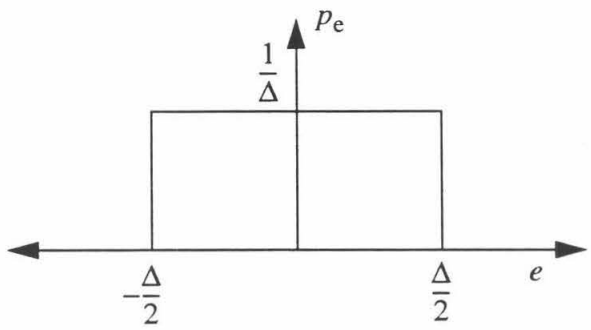

Figure B-3: Probability density function for a rounding quantizer.

case,

$$\begin{aligned} \text{SNR} &< \left(\frac{10\ \text{V}}{1.41 \times 10^{-3}\ \text{V}}\right)^2 \\ &< 77\ \text{dB} \end{aligned} \qquad \text{B-3}$$

Note, that changing the input range of the ADC does not affect this limit as the input range also appeared in the expression for σ. The maximum signal to noise ratio measurable in the face of digitization noise depends only on the number of bits used to store the binary data. For an arbitrary number of bits, the limit is:[1]

$$\begin{aligned} \text{SNR} &< \frac{1}{\Delta^2/12} = \frac{12}{2^{2(-b+1)}} = 3(2^{2b}) \\ &< 4.77 + 6.02\ b\ \text{dB} \end{aligned} \qquad \text{B-4}$$

B.3 Pre-Whitening and Anti-Aliasing Filters

The raw gravitational wave signal would exceed the signal to noise limits imposed by digitization noise. This is because we are attempting to detect minute test mass motions on

1. Note that this is for an analog signal which is symmetric around zero. For a single-sided signal a DC offset could be applied to use the full dynamic range of the ADC and gain 6 dB in SNR.

the order of 10^{-18} m/$\sqrt{\text{Hz}}$ above 100 Hz in the presence of much larger rms motions on the order of 0.1 μm. Most of the test mass motion is associated with the pendulum resonance around 1 Hz. To compensate for this we apply analog filters before the ADC so that the resulting signal fits well within the 77 dB range on the power spectrum from highest peak to lowest valley. These filters we call pre-whitening filters.

Note that the task of our current pre-whitening filters is only to change the overall shape of the power spectrum, and not to help reduce narrow features. The narrow features, primarily due to line spikes and suspension wire resonances, are numerous, far above the background (typically > 40 dB), and extremely narrow (typically < 0.1 Hz). This makes them very hard to remove with an analog filter; however, with a 12-bit ADC, this did not prove necessary.

An additional reason for analog filtering of the data before the ADC is to avoid aliasing problems. If the signal to be digitized has significant power above the Nyquist frequency of the ADC, this power will be aliased back into the band below the Nyquist frequency as shown on Figure B-4. [70] Typically anti-aliasing filters are designed to ensure that the power spectrum is not corrupted by aliasing up to frequencies 75-80% of the Nyquist frequency.[1]

The pre-whitening and anti-aliasing filters must also amplify the raw interferometer output to a level which uses as much of the ADC's dynamic range as possible while allowing some reserve for rare, very large events. Because an important goal of this work is to study these events, a very conservative reserve was allowed so that events up to roughly

1. It is possible to design anti-aliasing filters such that power in frequencies near or above the Nyquist frequency is less than the digitization noise, effectively eliminating aliasing. For reasons which are discussed in Section B.5, this is not desirable.

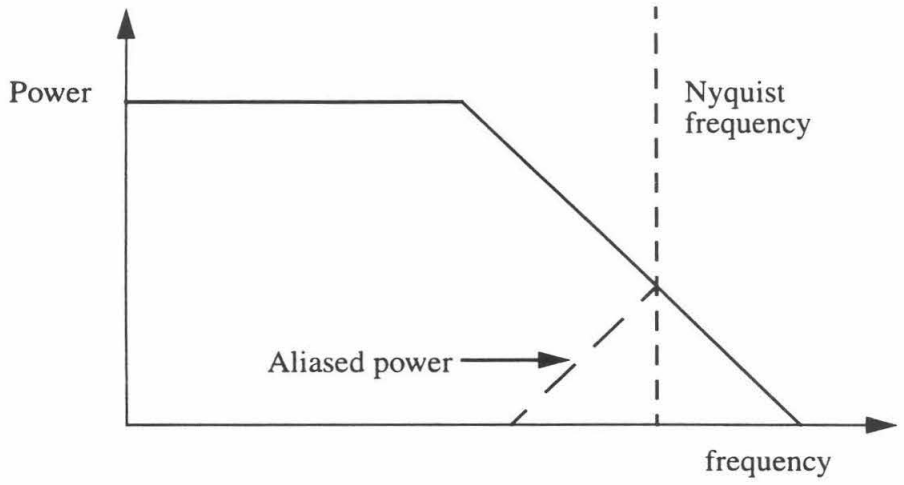

Figure B-4: Signal power above the Nyquist frequency is aliased back into the band below this frequency.

100 σ would not exceed the dynamic range of the ADC.

By using a number of adjustable filters, the raw gravitational wave signal was pre-whitened and attenuated sufficiently at high frequencies to avoid aliasing problems. A typical resulting power spectrum recorded by an HP 3563A signal analyzer is shown in Figure B-5.

B.4 Optimal Filtering

The general problem we are faced with is that we want to determine if a known signal exists in a data set which may be composed only of noise or of noise plus signal. We apply some filter to the data set, $o(t)$, to determine whether the signal exists. Any linear filter can be expressed as a correlation:[1]

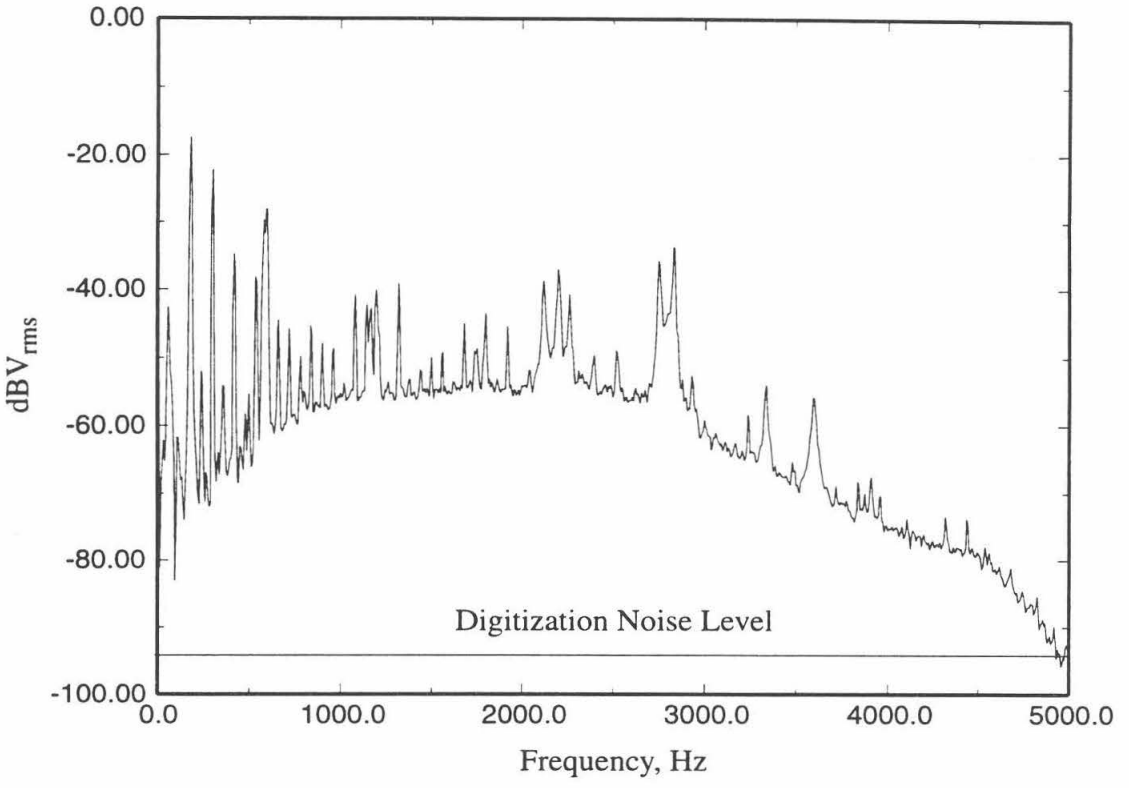

Figure B-5: Power spectrum of interferometer output after filtering as seen by ADC.

$$c(t) = \int_{-\infty}^{\infty} o(\tau)\, q(\tau - t)\, d\tau \qquad \text{B-5}$$

where $c(t)$ is the filter output and $q(t)$ is the impulse response of the filter. The convolution theorem allows us to write this more simply in the frequency domain:

$$\tilde{c}(f) = \tilde{o}(f)\, \tilde{q}^*(f) \qquad \text{B-6}$$

A signal is said to be present if $c(t)$ is above some threshold level. The question then is

1. Note that although we are considering only linear filters here, we do not restrict ourselves to causal filters. That is the filter output at a particular time can depend on filter inputs in the future. This obviously requires analysis on the complete data set after data acquisition.

what filter to use for $q(t)$ and what threshold level to use.

The optimal filter is so named because it gives the highest signal-to-noise ratio (SNR) of any linear filter. For a known signal, $h(t)$, the optimal filter is

$$\tilde{q}(f) = \frac{a\,\tilde{h}(f)}{S(f)} \qquad \text{B-7}$$

where $S(f)$ is the power spectral density of the noise and a is a normalization constant. This says that the optimal SNR is obtained by correlating the data set with the signal, weighted at every frequency by the inverse of the power spectral density of the noise. Thus frequencies where the noise is low will be weighted more strongly by the filter. Because the signal we are looking for is assumed to be rare, we can estimate the power spectral density of the noise by measuring the power spectral density of the output of the detector averaged over some long period of time. The optimal SNR achieved, then, in the presence of the signal is

$$(\mathrm{SNR})^2 = 4\int_0^\infty \frac{|\tilde{h}(f)|^2}{S(f)}\,df \qquad \text{B-8}$$

The SNR measure with an optimal filter will be the optimal SNR with a variance of 1.

The question of what threshold level to choose is a matter of trading off the probability of missing a real signals versus the probability of falsely detecting a signal when none is present. In our case we approach this from the standpoint that we can allow an average of one false event in ten years in a pair of identical interferometers, aligned with each other and separated by 3000 km. This is similar to the specification for the LIGO detectors. Thus, we are asking the question, if the 40-m interferometer and an identical instrument were being used as the two LIGO interferometers, what threshold level could we set to have reasonable confidence that any events detected were true events?

The signals we are considering here have durations of 1 ms. The light travel time between the two detectors is 10 ms. Thus we will only consider events in the two detectors coincident if they occur within this window of 21 ms of each other. Thus if we see events in each detector at a rate of r_1 per year, the rate at which we will see coincident events in both detectors within 10 ms of each other is:

$$r_2 = r_1^2 \left(\frac{21 \text{ ms}}{1 \text{ year}} \right) = 6.66 \times 10^{-10} \, r_1^2 \qquad \text{B-9}$$

Since we want $r_2 = 0.1$ / year, this means we can tolerate a false alarm event rate in one detector of $r_1 = 1.22 \times 10^4$ events per year or 1.4 events per hour. In addition to being coincident in time we also expect the signals to have the same amplitudes as recorded by the two detectors since they are aligned with each other. We adopt the criterion that the signals must have the same amplitude to within 10%.

It is in principle straightforward to optimally filter the data for a known signal in either the time (Eq. B-5) or frequency (Eq. B-6) domain. Although these two methods are mathematically equivalent, the frequency domain is computationally much more efficient. The time domain method involves doing a separate integral for each arrival time, t, in Eq. B-5. The frequency domain method on the other hand involves two Fourier transforms, one to put the data into the frequency domain and one to return the filtered data to the time domain to determine arrival times. However, these can be computationally very efficient using Fast Fourier Transform (FFT) algorithms. [71]

A FFT requires approximately $N \log N$ multiplications, where N is the number of data points, and for efficiency all of these points should be held in the computer memory. Thus we must filter the data set in smaller blocks of data. The price we pay for doing this

is that in order to avoid edge effects and splitting a signal between two blocks of data, we must overlap adjacent blocks of data as shown in Figure B-6.

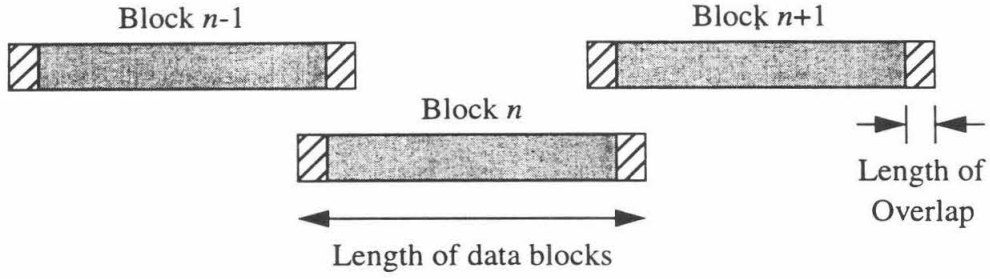

Figure B-6: Picture of overlapping blocks of data. The shaded regions are recorded as filtered data, while the hashed regions are discarded.

The question of how long the blocks of data should be and how much of an overlap is required has received some discussion for the case of coalescing binaries. [65][55] For optimally filtering very short signals, however, these considerations are not entirely applicable. The length of the blocks of data is set by the minimum frequency width feature that one wishes to resolve in the power spectral density of the noise. If the data blocks are T seconds long, the width of the frequency bins will be $1/T$. The interferometer noise spectrum has very sharp features in it, particularly line spikes and the resonances of the wire violin modes, with FWHM of substantially less that 0.1 Hz. If these features are not resolved, the optimal filtering algorithm will essentially ignore everything in the frequency bin they are in and, in a sense, throw away more usable observing bandwidth than was necessary. Another concern is that although some spectral features have very narrow peaks over short time scales, over several minutes the exact frequency of these peaks may drift. Very fine frequency resolution is not necessary in this case. A data block length of 10 s was chosen as a reasonable compromise that was quite manageable computationally.

The overlap between blocks was chosen empirically. Clearly it has to be at least as long as the signal, but the impulse response of the optimal filter will typically have significant amplitude for much longer times. This can be an issue due to edge effects, because the block of data is assumed by the algorithm to repeat indefinitely and thus there will generally be a discontinuity at the edges. This jump at the Nyquist frequency will be hugely amplified by the filter because of the $1/S(f)$ weighting, so we must discard the data around the edges for a time that is comparable to the impulse response of the filter. An overlap of 0.4 s at the beginning and end of each block of data worked well and was typically a few times the length of the large transients seen at the edges of the filtered blocks of data.

B.5 Nonstationary Noise Sources

The nonstationary noise transients in the raw interferometer output are disturbingly frequent and large. Qualitatively they all look similar because a high frequency disturbance anywhere is filtered by the differential mode servo[1] to look like the impulse response of the servo loop. A typical example is shown in Figure B-7. Note that these nonstationary events look very similar to the signal we are optimally filtering for. For kHz frequency burst sources, these nonstationary noise transients very significantly limit the interferometer sensitivity.

The rate of the nonstationary noise events in the 40-m interferometer has varied by orders of magnitude over time. Data runs, typically of several hours duration, have been taken occasionally by the author in the 40-m interferometer since August 1992. Although

1. Note that because these measurements were made in the Fabry-Perot configuration, the differential mode servo loop in that configuration in fact only controlled the length of one arm of the interferometer. Its open loop gain, however, was very close to the recombined differential mode servo open loop gain.

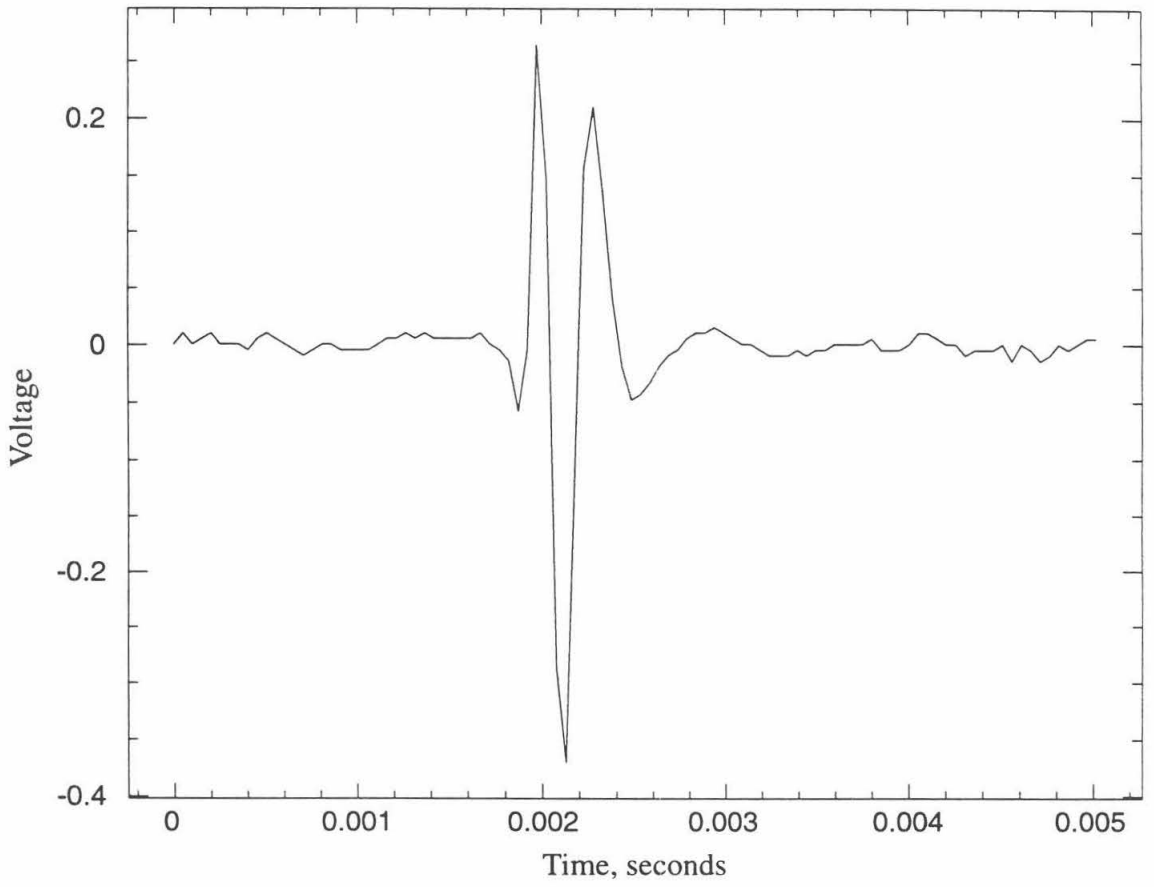

Figure B-7: Typical nonstationary noise transient in interferometer output.

the history of the interferometer's modifications is too complicated to describe here, the interferometer was under more or less continual modification during this time in its function as a test bed for LIGO. This made meaningful characterization of the nonstationary noise very difficult. Many of the noise sources that would be likely to contribute such noise would depend on fine details such as the quality of a particular cabling connection, which would be changed frequently. The earliest data indicated that the rate of 8σ events in the interferometer varied between 0.3 to 1.5 per second. After a major vacuum rebuild and recabling by late 1993, the rates for 8σ events varied between 0.01 to 5×10^{-4} per sec-

ond. During this time two data runs recorded no events above those expected from Gaussian noise in almost 2 hours of running each time. Early results from the recombined interferometer found rates for 8σ events of 0.2 to 6×10^{-4} per second. [53]

Although most observed nonstationary noise transients are of unknown cause, there have been several sources identified and a number of candidates eliminated. The only environmental noise source observed to cause these noise transients has been magnetic fields. A magnetic pickup coil placed a few meters past the end of the east arm and aligned with the axis through the center of the test mass observed noise bursts which were coincident with events in the interferometer output. This is shown in Figure B-8. However, during this same period of time, there were many far larger noise transients that were not correlated with events on the magnetic pickup coil. One such very large noise transient is shown in Figure B-9.[1]

Other types of excess noise, to which we can ascribe a cause, do not appear in the raw interferometer output, but are only seen after optimally filtering. If the anti-aliasing filters are rolled off too sharply, some part of the frequency band below the Nyquist frequency will be limited by digitization noise. This will produce non-Gaussian noise in the output of the optimal filter. This is because the $1/S(f)$ factor in the optimal filter will emphasize the frequency bands where digitization noise dominates other random noise contributions. Digitization noise is inherently non-Gaussian. Its probability density function is shown in Figure B-3. Thus we must assure in designing our pre-whitening and anti-aliasing filters that no part of the power spectrum below the Nyquist frequency is dominated by digitiza-

1. Note that the voltage scale for the interferometer output on Figure B-9 is an order of magnitude larger than on Figure B-8.

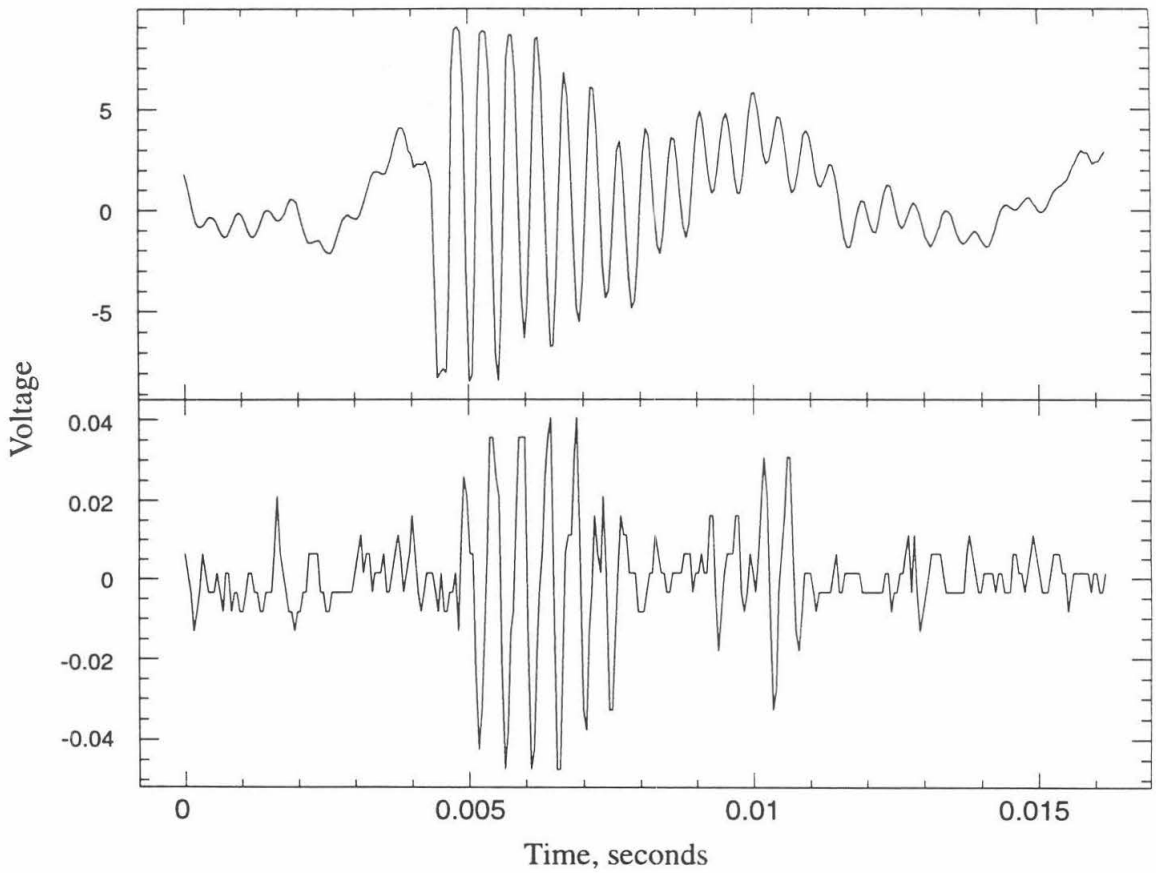

Figure B-8: Large transient on magnetic pickup coil (upper plot) seen in interferometer output (lower plot) from August 27, 1992.

tion noise as mentioned in Section B.3.

The tape writing process itself also appears to produce non-Gaussian noise. For some tapes after optimal filtering, the output shows huge peaks that are spaced 5.1 seconds apart. This is exactly the period between successive writes to tape. The storage buffers in the data acquisition computer's memory are flushed to the tape every 5.1 seconds. There is no indication of anything correlated with the tape writing interval in the unfiltered interferometer output. A similar effect was seen in an MIT prototype delay line interferometer by D. Dewey. [72] The exact reason for these peaks is unknown and they seem to come and

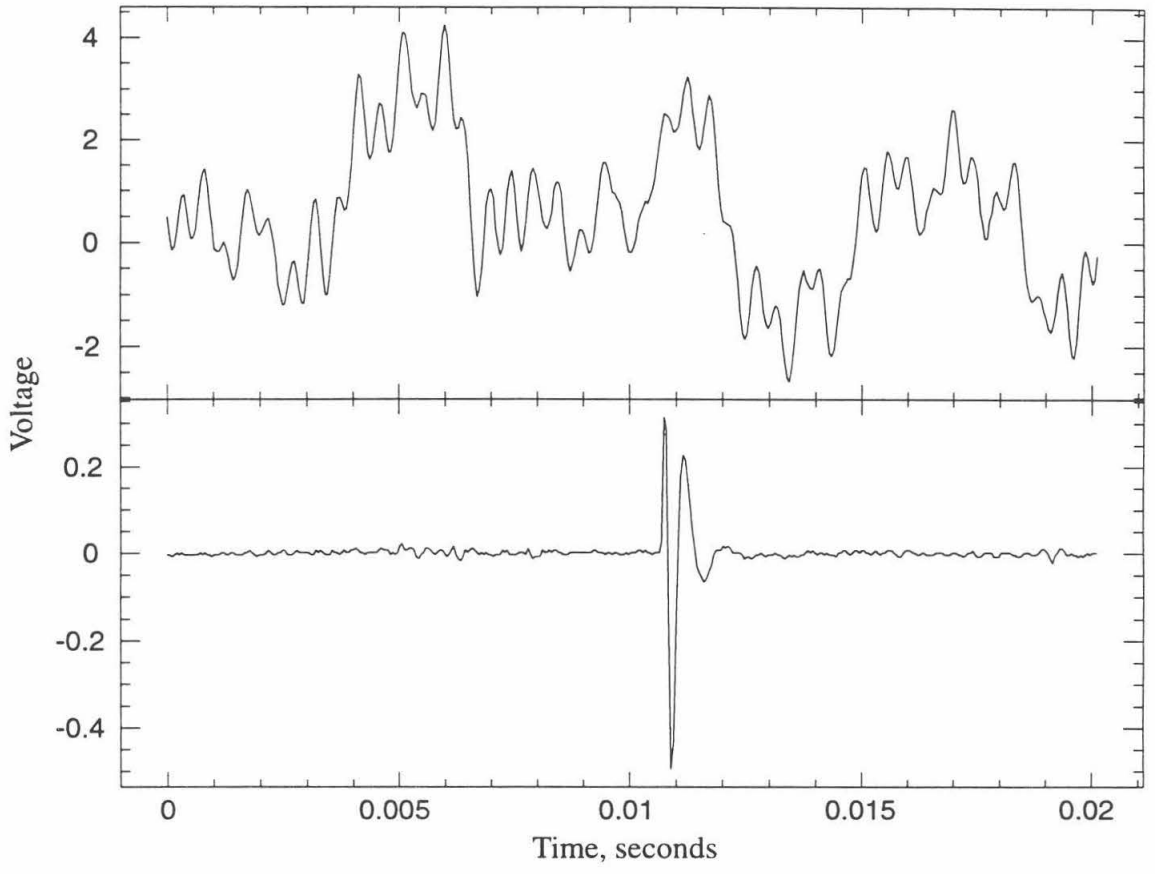

Figure B-9: Large transient on interferometer output (lower plot) not seen on magnetic pickup coil (upper plot) on August 27, 1992.

go over periods of tens of minutes. Possible explanations are electromagnetic pickup in the ADC when the tape drive motor turns on or a defect in the software that causes individual samples of data to be lost at each tape cycle. Whatever the explanation it is clear that in some situations the tape writing impresses an intermittent, small, high frequency signal onto the data which is amplified greatly by the optimal filter.

Aside from the magnetic pickup coil, no correlations have been seen between large events on the interferometer output and large events or slow trends on other channels that were recorded. The other channels which do not appear to be the cause of the very large

transients in the interferometer output include: the output of the first arm preamplifier module which was later used in the recombined interferometer as the common mode preamplifier, the seismometer, a microphone suspended over the laser table, the voltage on the slow piezoelectric transducers which are used for laser frequency stabilization, and the level of the DC coupled interferometer output. Some events seen on the microphone were correlated with events on the seismometer as is expected. A large event on any of these channels might reasonably be expected to provide a significant disturbance to the interferometer. On the other hand the level of the slow piezoelectric transducers on the laser or the DC coupled interferometer output might have been expected to correlate with increased levels of noise transients as the laser mirror or test mass drive coil circuits got near the edge of their range.

B.6 Gravitational Wave Search

Over the course of the week of November 14-21, 1994, a data run was taken with the 40-m interferometer as a simulated search for gravitational waves. These data were used by A. Gillespie to search for gravitational waves from coalescing binaries. [65] 11 tapes were recorded containing over 46 hours of data. During this time the interferometer was in lock 88.5% of the time. However, much of the time the interferometer was in lock for only brief periods. To allow the test mass suspension wire's violin resonance to decay and the noise to settle to a stable level after acquiring lock, the first 3 minutes of each locked section of data were discarded. With this criterion, the useful fraction of the data for analysis was only 60.8%, or just over 28 hours of useful data. The useful fraction varied greatly with time, being as low as 26.2% for one four and a half hour data tape, to 90.3% for a

tape started 12 hours later.

The results discussed below are for the tape with the greatest useful time for analysis which was recorded between the hours of 11:15 pm and 3:15 am on the night of November 19-20, 1994. On this tape 3.98 hours of data were filtered. The results from other tapes were similar except for those sections of time that had to be discarded because of the appearance of large noise transients synchronized with the tape writing.

A histogram of the unfiltered sample values is shown as a solid line in Figure B-10 compared with a dashed line indicating a Gaussian estimate using the same total number of points and standard deviation as the data. The standard deviation is calculated by taking the standard deviation of the entire data set in the time domain. The non-Gaussian part of the noise accounts for a very small part of the total energy of the signal because the large events are relatively infrequent. Thus, those points that lie outside the Gaussian tail are described as excess non-Gaussian events.

Any particular non-Gaussian event in the data record will be composed of a number of individual samples that lie outside the Gaussian distribution. We would like to identify all these non-Gaussian samples as a single event, which we shall call a "pulse." The utility of doing this is demonstrated in Figure B-11. During this data run on March 2, 1994, a waveform to produce a single cycle of a sine wave at 1 kHz was fed the calibration coil on the east end test mass at various points in time. There were 1670 total applied pulses and they were all correctly found by the pulse finding algorithm. In the sample value histogram, these distinct events show up as a broad region of non-Gaussian samples above 1 V, while on the pulse height histogram, it can be seen that all of the non-Gaussian events were clustered in height around 3.8 V. This also served as a test of our ability to correctly

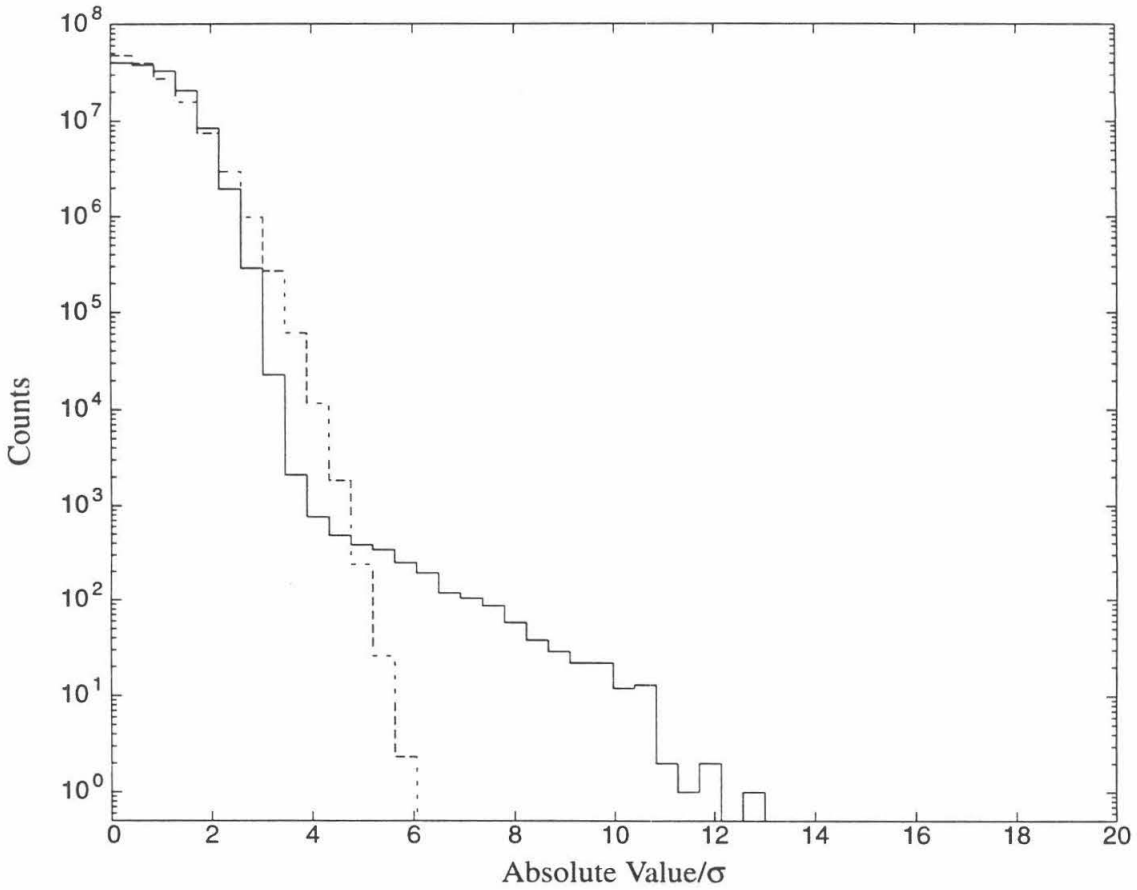

Figure B-10: Histogram of unfiltered sample values (solid) with line for comparison, showing Gaussian distribution with same number of points and standard deviation (dashed).

calibrate the expected SNR of applied pulses as the calculated SNR for these pulses from Eq. B-8 agreed with the central pulse height observed.

The following algorithm was used to identify pulses. A threshold level is set at 3σ. The computer searches through the data for a time when the threshold is exceeded. When a threshold crossing is detected, it continues searching through the data, counting down a delay time, but resets the delay time every time the data again exceeds threshold. When the delay time is finished counting down, the computer records the entire event as one

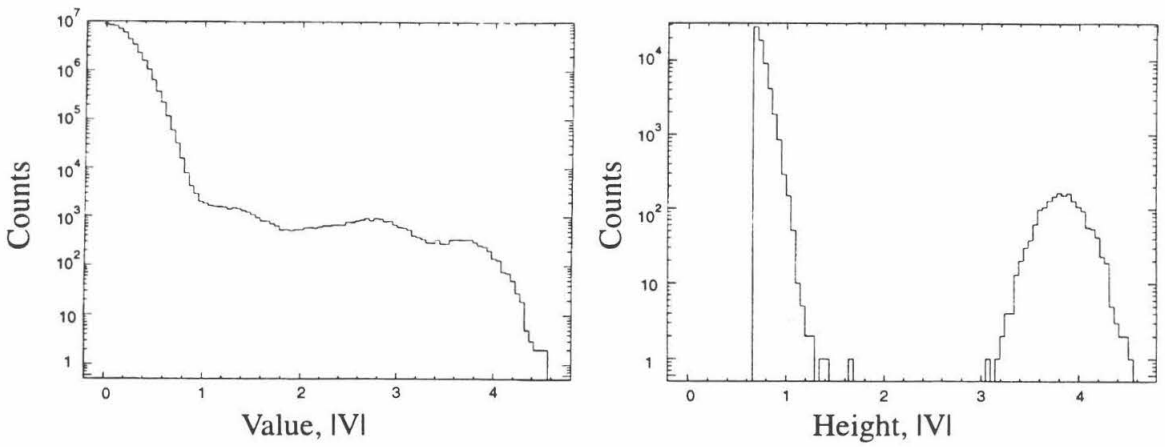

Figure B-11: Sample value histogram (left) and pulse height histogram (right) of same 46 minutes of data with pulses fed into calibration coil of interferometer.

pulse with a height equal to the absolute value of the peak data point in the pulse. In this way, an event that consist of multiple oscillations is treated as a single pulse. The delay time need only be set to be longer than one-half the typical oscillation period and is assumed to be much shorter than the typical time between pulses. In this case a 1 ms delay time was used.

Applying this pulse finding algorithm to the unfiltered data and histogramming the output, we get the result shown in Figure B-12. Note that the pulse finding algorithm is a non-linear filter and as such its output, given a Gaussian input, will be non-Gaussian. In the limiting case of very rare, high σ events, however, its output will closely approximate a Gaussian. A Gaussian distribution with the same number of points and standard deviation as the pulse data is shown for comparison with the above caveat.

The sample value and pulse height histogram of the optimally filtered outputs are shown in Figure B-13 and Figure B-14 with Gaussian distributions for comparison. Notice

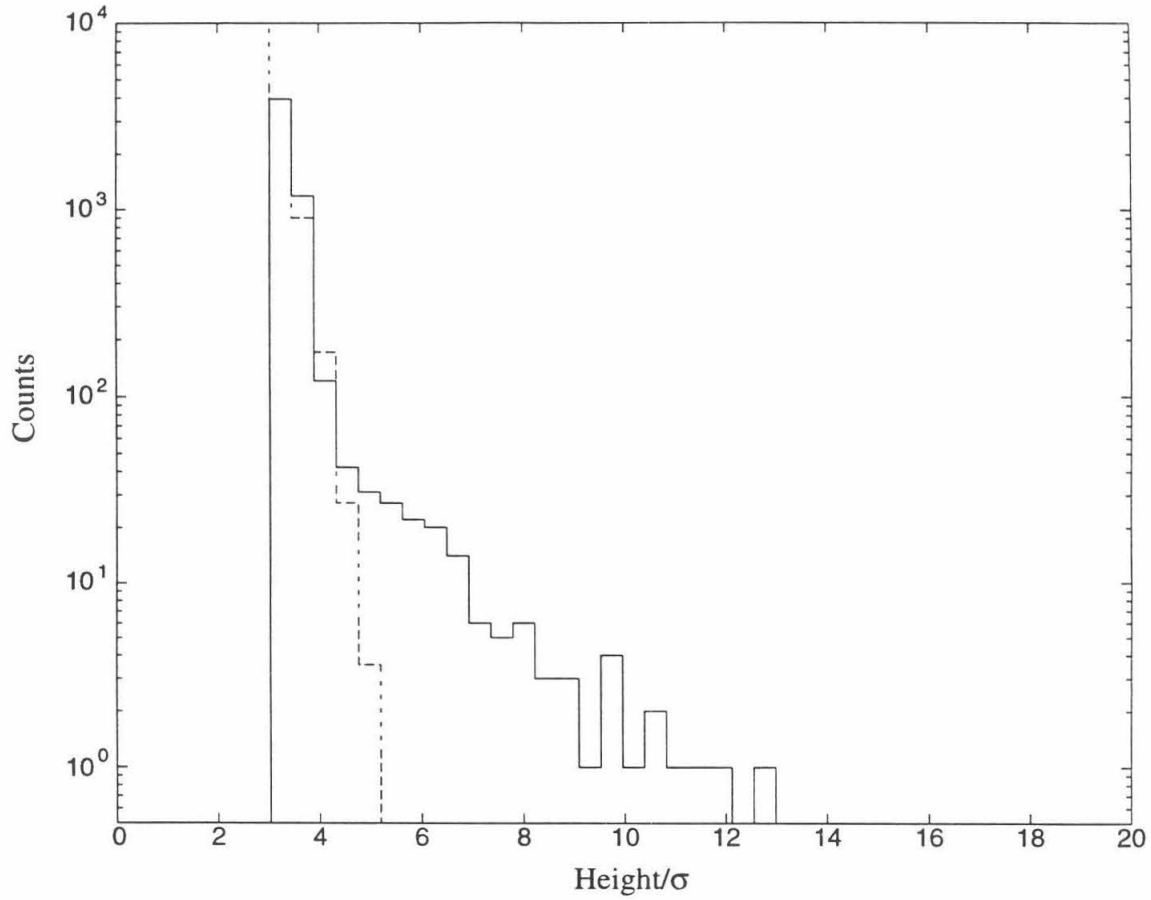

Figure B-12: Histogram of unfiltered pulse heights (solid) with line for comparison, showing Gaussian distribution with same number of points and standard deviation (dashed).

that optimal filtering made the situation worse in the sense that there are now more high σ events. This means that the non-Gaussian noise transients are very similar in shape to a single cycle of a sine wave at 1 kHz.

From Figure B-14 we can determine above what threshold level would it be reasonable to declare an event in the output of the optimal filter a candidate gravitational wave event. Assuming that we have another identical, aligned detector 3 km away, we showed before that we could allow 1.4 false events per hour in a single detector. Thus in the 3.98

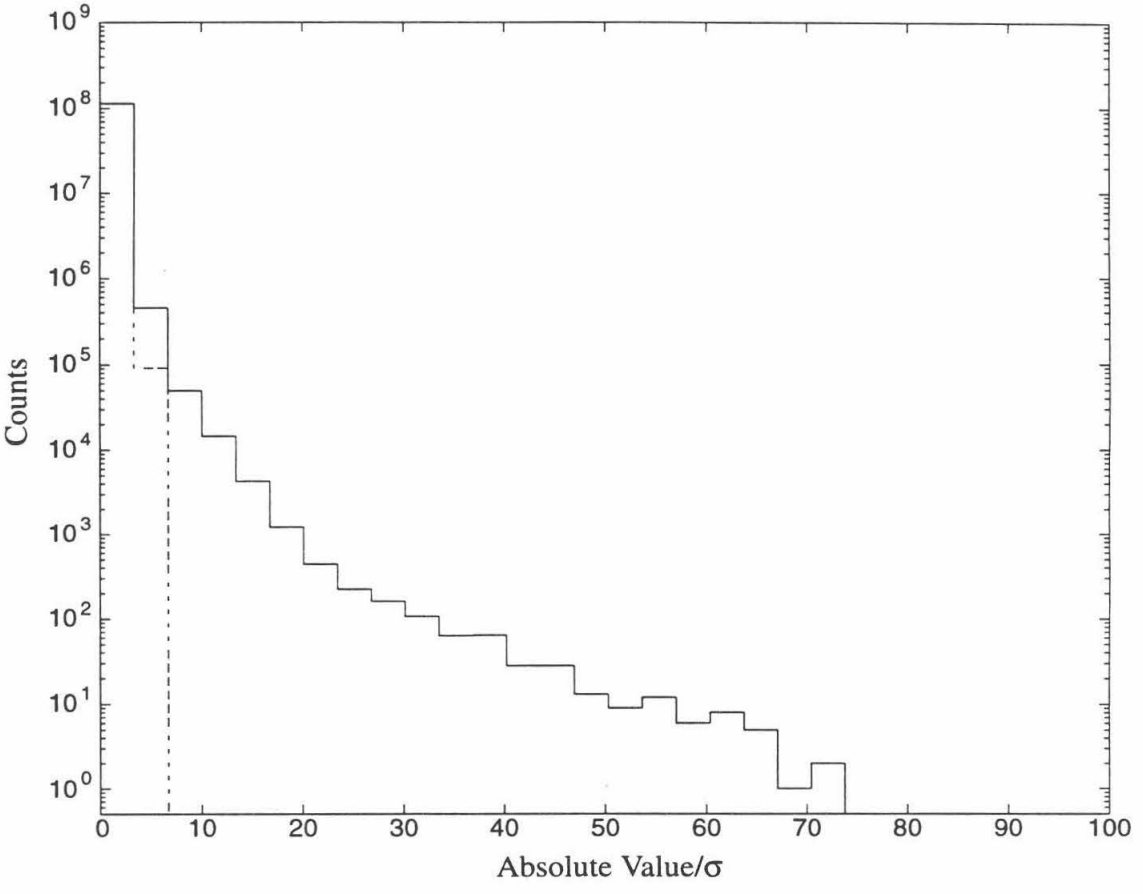

Figure B-13: Histogram of optimally filtered sample values (solid) with line for comparison, showing Gaussian distribution with same number of points and standard deviation (dashed).

hours of analyzed data, we can allow six false events. The lowest threshold we can set where there are six or fewer events with heights within 10% of each other is 44σ. If the noise were purely Gaussian, we could set this threshold at 6σ. Thus the non-Gaussian part of the noise causes us to lose a factor of 7 in sensitivity for detecting a single cycle of a 1 kHz sine wave.

From Eq. B-8 we can determine how large of a signal would produce a 44σ event in

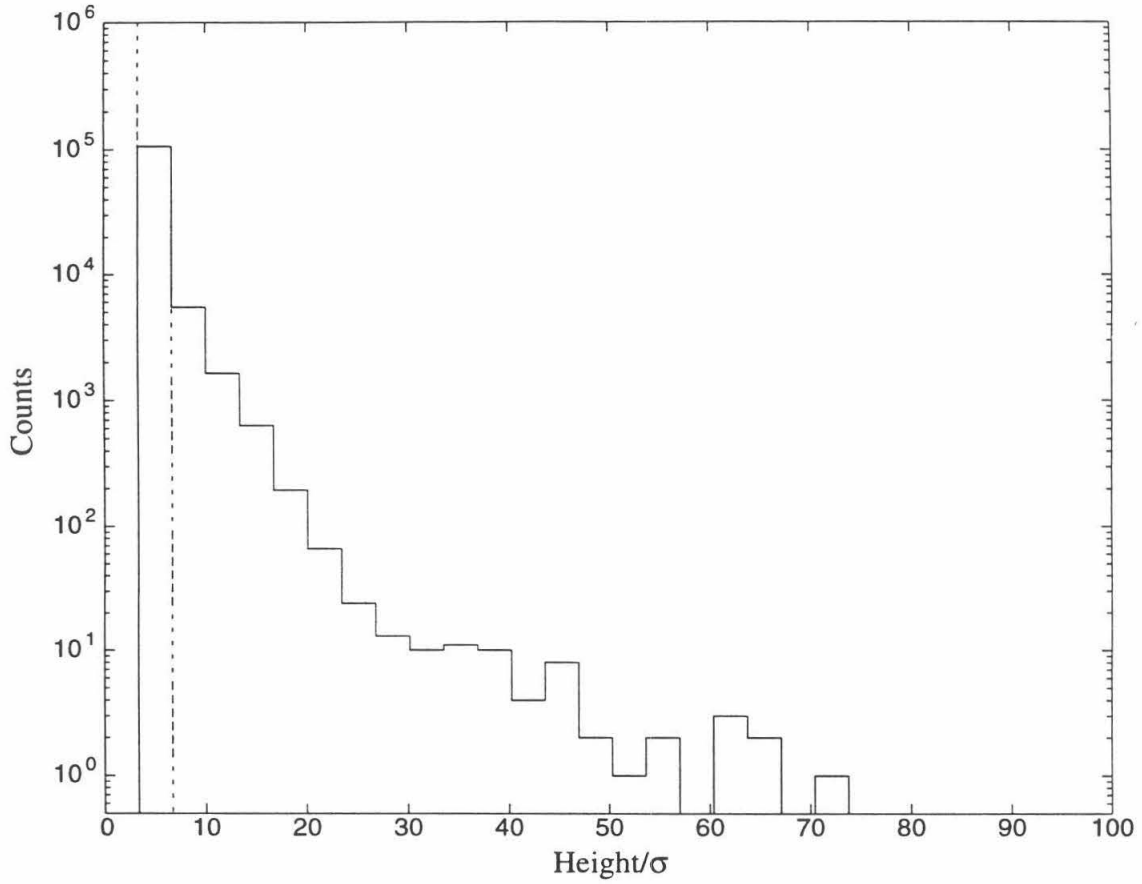

Figure B-14: Histogram of optimally filtered pulse heights (solid) with line for comparison, showing Gaussian distribution with same number of points and standard deviation (dashed).

the output of our optimal filter. A single cycle of a 1×10^{-15} m_{rms} sine wave at 1 kHz would give an output of 88σ from the optimal filter. Thus, the 40-m interferometer sensitivity to a single cycle of a 1 kHz sine wave is 5×10^{-16} m_{rms}. Various regions of the detector bandwidth contribute different amounts to the sensitivity to this signal. We identify the $(SNR)^2$ contribution per Hz at a particular frequency as the integrand of Eq. B-8, $|\tilde{h}(f)|^2/S(f)$. The $(SNR)^2$ contribution per Hz when optimally filtering for a single cycle

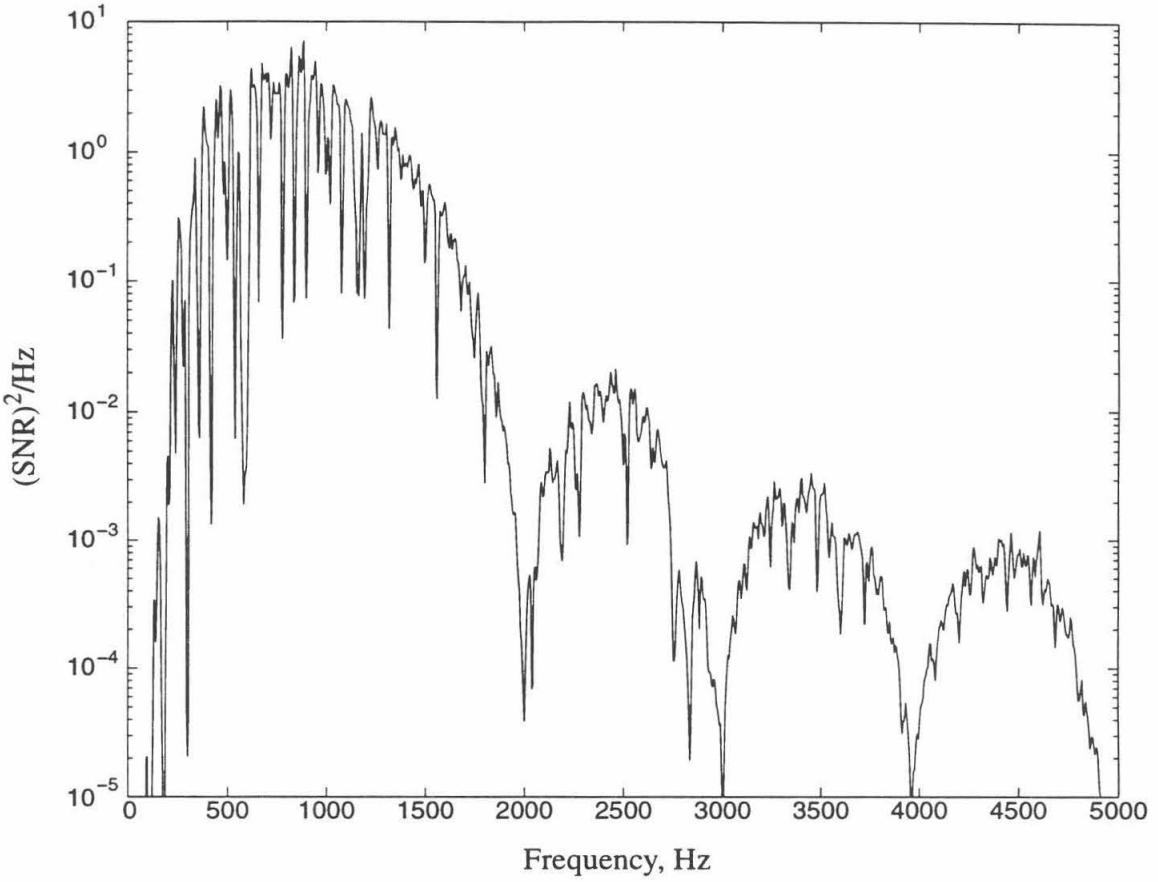

Figure B-15: Squared signal-to-noise ratio contribution per Hz to the output of an optimal filter searching for single cycle of a 1×10^{-15} m_{rms} sine wave at 1 kHz.

of a 1 kHz sine wave is shown in Figure B-15. As expected it is peaked between 300 and 1200 Hz, as this is the region of best interferometer sensitivity.

Appendix C: Effect of Shaking an End Mirror

Here we derive the effect on E_A of shaking mirror 4 at frequency Ω as mentioned in Section 2.4. To do this we will need to calculate the field reflected from the arm cavity, E_5, in terms of the incident field, E_4. This is done in two steps. First we solve for E_5 given a small DC displacement of mirror 4. Then we generalize this result to frequencies in the gravitational wave band.

Consider a small displacement of mirror 4 away from the carrier resonance. Let $x_4 = 0$ on resonance so that $x_4 = x_0$ after the displacement. We define a generalized notion of the arm cavity reflectivity away from resonance so that $E_5 = r_{arm}(\phi)\, E_4$, where from Eq. 2-8,

$$r_{arm}(\phi) = \frac{r_3 - (1 - L_3)\, r_4\, e^{i\phi}}{1 - r_3\, r_4\, e^{i\phi}} \qquad \text{C-1}$$
$$\phi = 2\, k\, x_4$$

Taylor expand $r_{arm}(\phi)$:

$$E_5 = E_4 \left(r_{arm}\big|_{x_4 = 0} + \frac{dr_{arm}}{dx_4}\bigg|_{x_4 = 0} x_0 + \ldots \right) \qquad \text{C-2}$$

Thus, using Eq. 2-14 and $d\phi/dx_4 = 2k$, for arbitrarily small x_0 we can write

$$E_5 = E_4 \left[\frac{r_3 - (1 - L_3)\, r_4}{1 - r_3\, r_4} - 2ik \frac{T_3\, r_4}{(1 - r_3\, r_4)^2}\, x_0 \right] \qquad \text{C-3}$$

Now let $x_4 = x_0 \sin \Omega t$. Note that in the small amplitude limit we are considering, shak-

ing the rear mirror at frequency Ω is equivalent to injecting sidebands through the rear mirror at frequencies Ω above and below the carrier frequency. We consider then the effect of sidebands injected through the rear mirror. The transmission of light injected through the arm cavity is, from Eq. 2-9,

$$t_{arm}(\phi) = \frac{t_3 t_4 e^{i\phi/2}}{1 - r_3 r_4 e^{i\phi}} \qquad \text{C-4}$$

Now, $\phi = 2\omega l/c$ where ω is the angular frequency of the light and l is the length of the cavity. The frequency of the light with the impressed sidebands from the mirror motion is $\omega = \omega_0 \pm \Omega$ where ω_0 is the carrier resonance frequency. If we assume Ω is small compared to the cavity free spectral range,[1] we can approximate:

$$\exp[i\phi] = \exp\left[2i(\omega_0 \pm \Omega)\frac{l}{c}\right] = \exp\left[i\Omega\frac{2l}{c}\right] \approx 1 \pm i\Omega\frac{2l}{c} \qquad \text{C-5}$$

$$t_{arm}(\phi) = \frac{t_3 t_4\left(1 \pm i\Omega\frac{l}{c}\right)}{1 - r_3 r_4\left(1 \pm i\Omega\frac{2l}{c}\right)} \qquad \text{C-6}$$

This has a zero at angular frequency c/l which is twice the cavity free spectral range. This zero is well above the gravitational wave band and therefore not of interest. There is also a pole at angular frequency

$$\omega_c = \frac{c}{2l}\frac{1 - r_3 r_4}{r_3 r_4} \qquad \text{C-7}$$

---

1. The arm cavities for LIGO will have a free spectral range of 37.5 kHz, and for the 40-m interferometer it is 3.75 MHz.

This is the so called *cavity pole*. It will typically be important and lie in the gravitational wave band.

We can now generalize from the DC case by noting that all the frequency dependence in the transfer function from x_4 to E_5 is contained in a single pole.

$$E_5 = E_4\left[\frac{r_3-(1-L_3)\,r_4}{1-r_3\,r_4} - 2ik\frac{T_3\,r_4}{(1-r_3\,r_4)^2}\frac{x_0\sin(\Omega t+\psi)}{\sqrt{1+(\Omega/\omega_c)^2}}\right] \qquad \text{C-8}$$

where ψ is a phase factor which is irrelevant for this analysis.

If we assume negligible losses in the beam splitter,

$$E_4 = \frac{E_2}{\sqrt{2}} \qquad E_6 = -\frac{E_2}{\sqrt{2}} \qquad \text{C-9}$$

The field at the antisymmetric port is

$$E_A = \frac{1}{\sqrt{2}}E_5 + \frac{1}{\sqrt{2}}E_7 \qquad \text{C-10}$$

Now,

$$E_7 = E_6\frac{r_5-(1-L_5)\,r_6}{1-r_5\,r_6} \qquad \text{C-11}$$

$$\therefore\ E_A = E_{DC} - i\,k\,E_2\frac{T_3\,r_4}{(1-r_3\,r_4)^2}\frac{x_0\sin(\Omega t+\psi)}{\sqrt{1+(\Omega/\omega_c)^2}} \qquad \text{C-12}$$

where E_{DC} is the excess light at the antisymmetric port due to the imperfect matching of mirror parameters between the two arms or, more generally, any non-interfering sources of light on the photodetector.

Appendix D: Average Power Spectrum of the Demodulator Output

In this appendix, we derive the average power spectrum of the demodulator output, [73] $\overline{S_{i_d i_d}}(f)$, from the time-averaged autocorrelation function, $\overline{R_{i_d i_d}}(\tau)$. To calculate $\overline{R_{i_d i_d}}(\tau)$, we first find the expectation value of the photocurrent, $E\{\boldsymbol{i_p}(t)\}$, in the absence of any signal. In this case $E_A = E_{DC}$, thus from Eq. 2-35:

$$\begin{aligned} E\{\boldsymbol{i_p}(t)\} &= |E_{DC}|^2 + 2E_+^{\,2} + 4E_+ \mathrm{Im}[E_{DC}]\cos\omega t \\ &\quad -2E_+^{\,2}\cos 2\omega t - 4E_{2+}\mathrm{Re}[E_{DC}]\sin 2\omega t \\ &= E_{DC}^{\,2} + 2E_+^{\,2} - 2E_+^{\,2}\cos 2\omega t - 4E_{2+}E_{DC}\sin 2\omega t \end{aligned} \qquad \text{D-1}$$

E_{DC} has no imaginary part, because if it had, the length control servo would induce a differential change in the cavity lengths to cancel it.

The total number of electrons having left the photodetector since some initial time t = 0 is modeled as a non-uniform Poisson process. A Poisson process ***x(t)*** is a random process which is constant except for unit increments at random points in time, $\boldsymbol{t_i}$.[74] We label $\lambda(t)$ the density of the points of $\boldsymbol{t_i}$. The term *non-uniform* applies if the density of points is a function of time. We identify $\lambda(t) = E\{\boldsymbol{i_p}(t)\}$. We write this as

$$\lambda(t) = a + b\cos 2\omega t + c\sin 2\omega t \qquad \text{D-2}$$

The photodetector output current is then a random process which is the derivative of a Poisson process. This is called a process of Poisson impulses. [75]

$$\begin{aligned} i_p(t) &= \frac{dx(t)}{dt} \\ &= \sum_i \delta(t - t_i) \end{aligned} \qquad \text{D-3}$$

The autocorrelation of a non-uniform Poisson process is: [76]

$$R_{xx}(t_1, t_2) = \begin{cases} \int_0^{t_2} \lambda(t)\, dt \left[1 + \int_0^{t_1} \lambda(t)\, dt \right] & t_1 > t_2 \\ \int_0^{t_1} \lambda(t)\, dt \left[1 + \int_0^{t_2} \lambda(t)\, dt \right] & t_2 > t_1 \end{cases} \qquad \text{D-4}$$

The autocorrelation of the derivative of a random process is given by [77]

$$R_{x'x'}(t_1, t_2) = \frac{\partial^2 R_{xx}(t_1, t_2)}{\partial t_1\, \partial t_2} \qquad \text{D-5}$$

Since $i_p(t) = x'(t)$ we have only to substitute into the equation above to find the autocorrelation for the photocurrent. So,

$$\begin{aligned} R_{i_p i_p}(t_1, t_2) &= \frac{\partial^2 R_{xx}(t_1, t_2)}{\partial t_1\, \partial t_2} \\ &= \begin{cases} \lambda(t_1)\, \lambda(t_2) & t_1 > t_2 \\ \lambda(t_2)\, \lambda(t_1) & t_2 > t_1 \end{cases} \end{aligned} \qquad \text{D-6}$$

However, there is a discontinuity in the derivative at $t_1 = t_2$. Thus,[1]

$$R_{i_p i_p}(t_1, t_2) = \lambda(t_1)\, \lambda(t_2) + \lambda(t_1)\, \delta(t_1 - t_2) \qquad \text{D-7}$$

---

1. Note that Eq. D-7 reduces trivially to the stationary case quoted in [78] for a process of Poisson impulses with constant density of points:

$$R_{x'x'}(\tau) = \lambda^2 + \lambda\, \delta(\tau)$$

We can use this result to find the time-averaged autocorrelation of the demodulator output $i_d(t) = i_p(t)\cos\omega t$:

$$\begin{aligned} R_{i_d i_d}(t+\tau, t) &= E\{i_p(t+\tau)\cos\omega(t+\tau)\, i_p(t)\cos\omega t\} \\ &= E\{i_p(t+\tau)\, i_p(t)\}\cos\omega(t+\tau)\cos\omega t \\ &= [\lambda(t+\tau)\,\lambda(t) + \lambda(t+\tau)\,\delta(\tau)]\cos\omega(t+\tau)\cos\omega t \end{aligned} \qquad \text{D-8}$$

$$\begin{aligned} \overline{R_{i_d i_d}}(\tau) &= \frac{1}{T}\int_0^T R_{i_d i_d}(t+\tau, t)\, dt \\ &= \frac{1}{T}\int_0^T [\lambda(t+\tau)\,\lambda(t) + \lambda(t+\tau)\,\delta(\tau)]\cos\omega(t+\tau)\cos\omega t\, dt \end{aligned} \qquad \text{D-9}$$

where T is the modulation period. The first term above will turn out to be irrelevant to our analysis; it is

$$\begin{aligned} &\frac{1}{T}\int_0^T \lambda(t+\tau)\,\lambda(t)\sin\omega(t+\tau)\sin\omega t\, dt \\ &\quad = \frac{1}{T}\int_0^T [a + b\cos 2\omega t + c\sin 2\omega t] \\ &\qquad [a + b\cos 2\omega(t+\tau) + c\sin 2\omega(t+\tau)]\cos\omega(t+\tau)\cos\omega t\, dt \\ &\quad = \frac{1}{2}\left[\left(a^2 + ab + \frac{1}{4}(b^2+c^2)\right)\cos\omega\tau + \frac{1}{4}(b^2+c^2)\cos 3\omega\tau\right] \end{aligned} \qquad \text{D-10}$$

The second term we will not evaluate for now. To find the average power spectrum, we take the Fourier transform of the average autocorrelation:

$$\overline{S_{i_d i_d}}(f) = 2\int_{-\infty}^{\infty} \overline{R_{i_d i_d}}(\tau)\, e^{2\pi i f\tau} d\tau \qquad \text{D-11}$$

We will evaluate the two terms in Eq. D-9 one at a time. The first term from Eq. D-10

gives

$$2\int_{-\infty}^{\infty}\frac{1}{2}\left[\left(a^2-2ab+\frac{1}{4}(b^2+c^2)\right)\cos\omega\tau+\frac{1}{4}(b^2+c^2)\cos 3\omega\tau\right]e^{2\pi if\tau}dt$$
$$=\left(a^2+ab+\frac{1}{4}(b^2+c^2)\right)\delta(2\pi f-\omega)+\frac{1}{4}(b^2+c^2)\,\delta(2\pi f-3\omega) \qquad \text{D-12}$$

To evaluate the second term we will switch the order of integration:

$$\frac{2}{T}\int_{-\infty}^{\infty}\int_{0}^{T}\lambda(t+\tau)\delta(\tau)\cos\omega(t+\tau)\cos\omega t\,dt\,e^{2\pi if\tau}d\tau$$
$$=\frac{2}{T}\int_{0}^{T}\int_{-\infty}^{\infty}\lambda(t+\tau)\delta(\tau)\cos\omega(t+\tau)\cos\omega t\,e^{2\pi if\tau}d\tau\,dt$$
$$=\frac{2}{T}\int_{0}^{T}\lambda(t)\cos^2\omega t\,dt \qquad \text{D-13}$$
$$=\frac{2}{T}\int_{0}^{T}(a+b\cos 2\omega t+c\sin 2\omega t)\cos^2\omega t\,dt$$
$$=a+\frac{b}{2}$$

Therefore, the average power spectrum of the demodulator output is

$$\overline{S_{i_d i_d}}(f)=3{E_+}^2+{E_{DC}}^2$$
$$+(9{E_+}^4+6E_{DC}^2{E_+}^2+{E_{DC}}^2+4E_{2+}^2E_{DC}^2)\,\delta(2\pi f-\omega) \qquad \text{D-14}$$
$$+(E_+^4+4E_{2+}^2E_{DC}^2)\,\delta(2\pi f-3\omega)$$

Appendix E: Description of the 40-m Interferometer

The electronics and optics used in the 40-m interferometer in its Fabry-Perot configuration were modified as little as possible for recombination. The modifications to optics and photodiodes were shown on Figure 2-3. The servo systems used for recombination and the necessary modifications are discussed in more detail below.

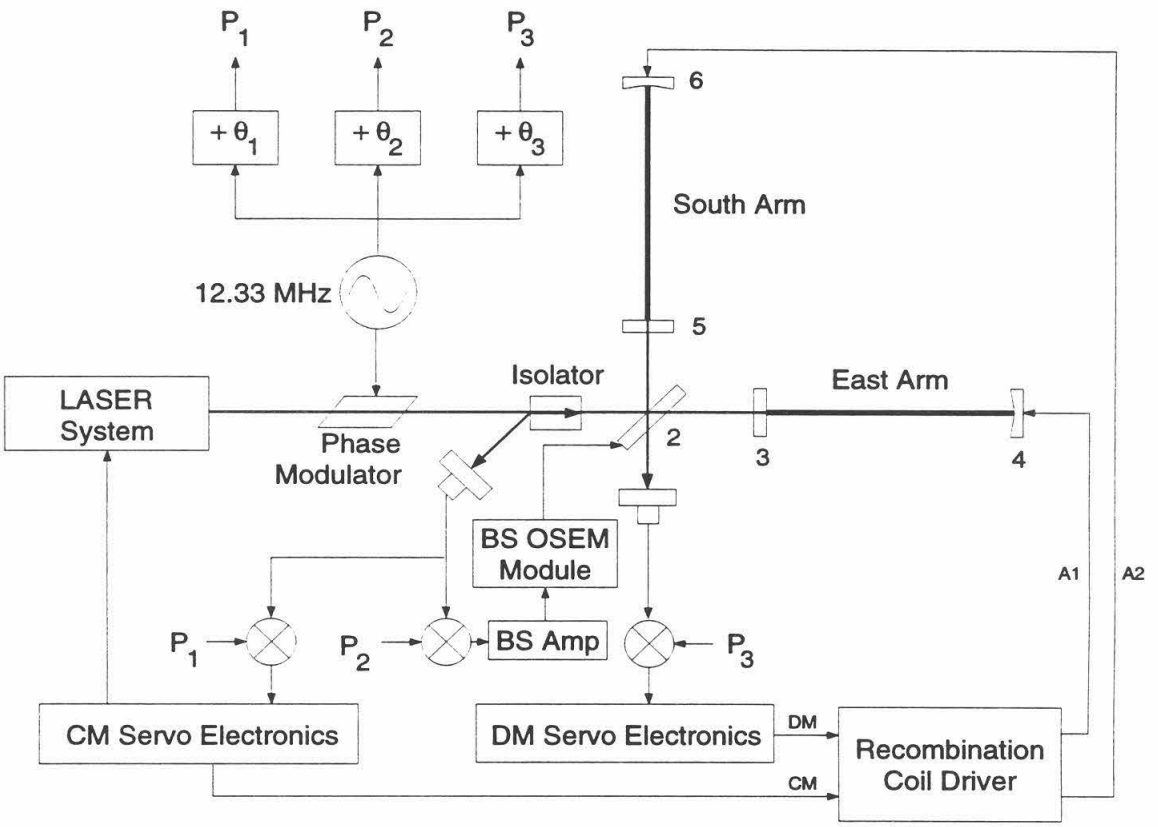

Figure E-1: Block diagram of the length control servos for the recombined 40-m interferometer.

A block diagram of the length control servos is shown in Figure E-1. Notice that the south arm is the arm that receives the light reflected from the beam splitter while the east arm is the arm that receives the transmitted light. The south arm is shown in its position on

the figure for ease of drawing, but in the 40-m interferometer it is south of the rest of the interferometer.

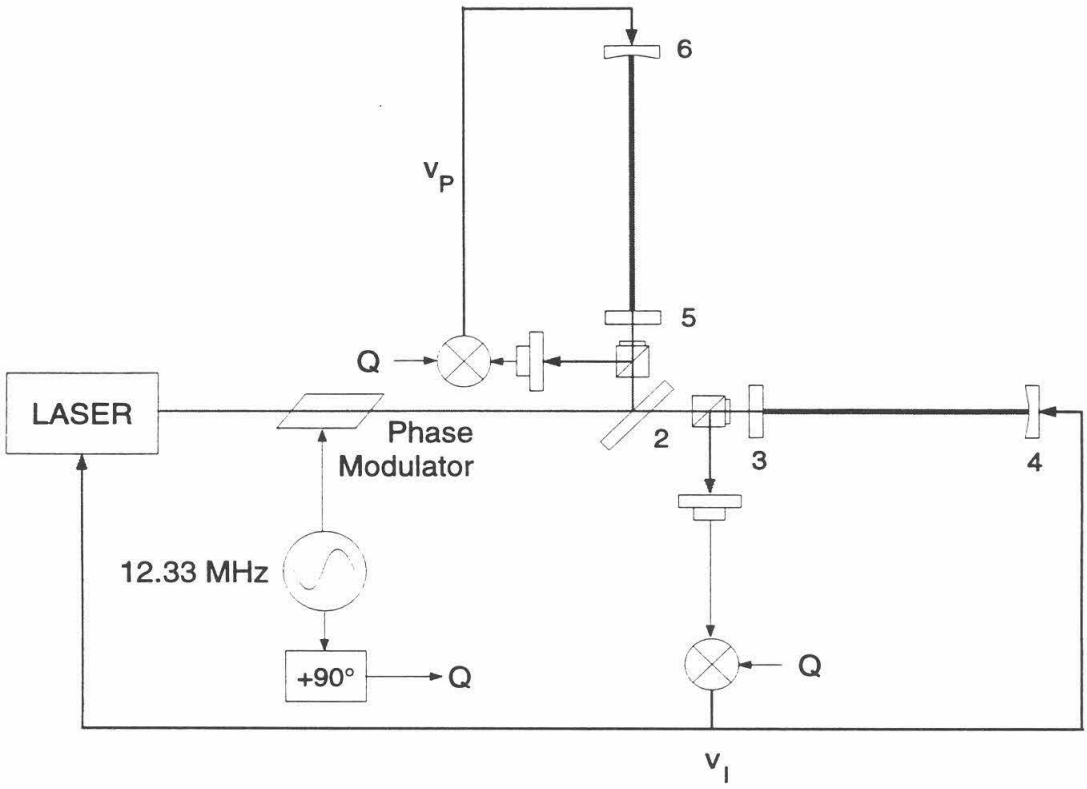

Figure E-2: Fabry-Perot interferometer configuration.

In the Fabry-Perot configuration (See Figure E-2.) the east arm was often referred to as the first arm and the south arm as the second arm. An error signal which provided the difference between the arm cavity resonant frequency and the laser frequency was extracted for each arm independently. The first arm error signal was fed back to laser at frequencies above approximately 3 Hz, so that the laser frequency followed the resonant frequency of that arm. At frequencies below 3 Hz the error signal was fed back to magnetic coils on the east end mass which maintained the arm on resonance. The arm length

was used as a reference for the laser frequency at higher frequencies because it was a more stable length reference at those frequencies, while below 3 Hz the motion of the pendulum suspensions of the test mass made the laser system a more stable frequency reference. The second arm error signal was fed back to control the second arm cavity's length such that its resonant frequency was at the laser frequency. The feedback signal was thus proportional to the difference between the lengths of the first and second arms because the length of the first arm was encoded on the laser frequency.

An important realization was that the performance required of the common mode servo in a recombined configuration had already been achieved by the first arm servo. In the case of the common mode servo, an error signal proportional to the average of the two arm lengths is used to control the laser frequency, except at very low frequencies. The open loop gain necessary is comparable to the first arm servo and so only the electronics which drive the end masses were modified.

Similarly the second arm servo had also achieved the performance goals for the differential mode servo. Thus the second arm electronics were used to control the differential mode. A new electronic module was constructed to allow the feedback to two end masses to be a sum of signals from the common and differential mode feedback signals. This is the recombination coil driver in Figure E-1 and the outputs, A1 and A2, were simply linear combinations of the common and differential mode inputs, CM and DM, as follows:

$$\begin{aligned} A1 &= CM + DM \\ A2 &= CM - DM \end{aligned} \qquad \text{E-1}$$

The servo to control the Michelson near mirror difference had to be designed and constructed specifically for recombination. The beam splitter was controlled in the previous

configuration by four magnets glued onto it, three in a triangular configuration on one face and one on its side to damp side to side motion. These magnets were driven by optically sensed electromotors (OSEMs) which ensure that the magnet remains in a fixed position in the middle of a coil surrounding it by use of an LED shadow sensor. The beam splitter OSEM control module also included provisions to allow a more sensitive signal proportional to the alignment error to be summed onto the coils. In this way the alignment and position fluctuations of the beam splitter were damped to a degree that was adequate for operation of the Fabry-Perot interferometer. As part of the recombination task, the beam splitter OSEM control module was modified to allow us to sum in a longitudinal drive signal (for control of the Michelson near mirror difference degree of freedom) to the three coils on the face of the beam splitter. This signal was provided by the beam splitter servo amplifier, designed to meet the criteria on the beam splitter loop gain discussed in Appendix F.

Each of the three servo loops had independent phase shifters to adjust the phase of the demodulation signal. These were adjusted as discussed in Section 3.3.

The box marked "LASER System" on Figure E-1 includes the laser, optics and servo systems to provide frequency and intensity stabilized laser light to the interferometer. A more detailed drawing of the laser system alone is shown in Figure E-3. The laser system provides frequency stabilized light, independent of the interferometer, by controlling the laser frequency to match the resonant frequency of a reference cavity. Since the light passing through this cavity is used by the interferometer, the cavity also provides some spatial filtering of undesirable higher order modes and reduces intensity fluctuations. In this capacity the reference cavity is called a mode cleaner cavity. The feedback to the laser fre-

quency is actuated by moving the laser mirrors (one with large dynamic range and slower response and one with faster response and lower dynamic range) and by frequency shifting the light at high frequencies with a Pockel's cell. The free running laser has a typical line width of 3 MHz which is reduced to roughly 30 Hz after being locked to the reference cavity. The bandwidth of the laser servo is approximately 1 MHz and it has a gain of 10^9 at low frequencies.[1]

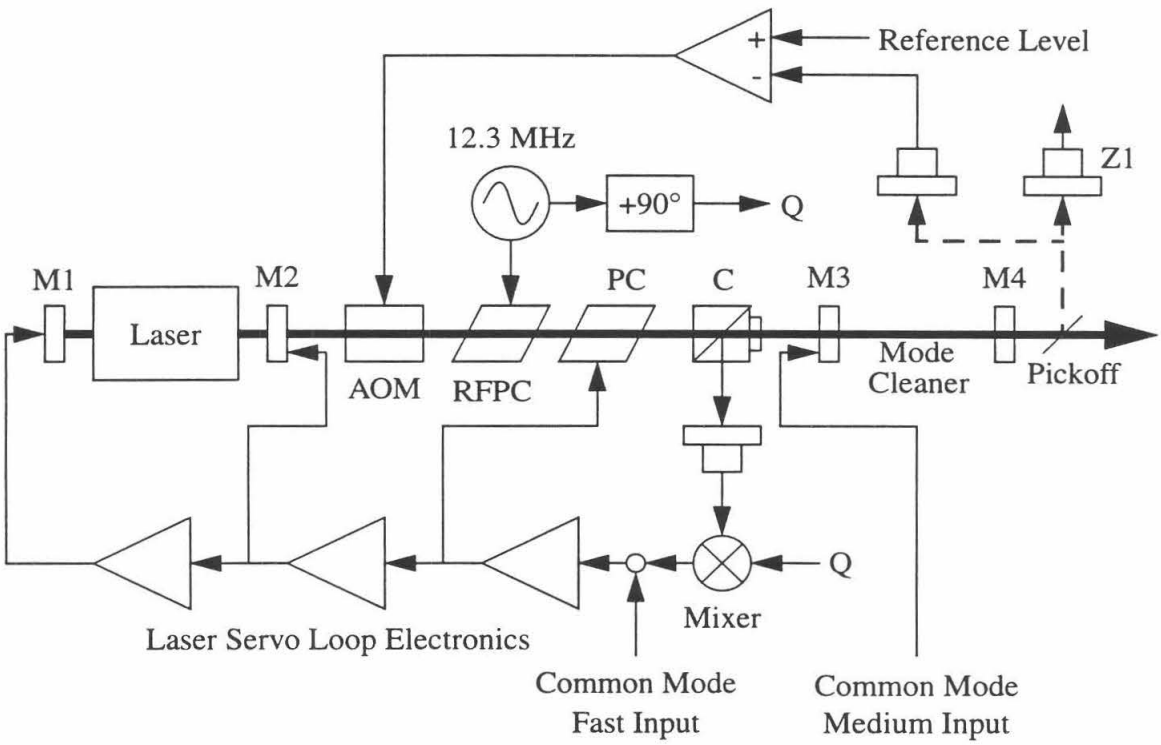

Figure E-3: Laser frequency and intensity stabilization system. The laser frequency is changed by feeding back to the laser mirrors (M1 and M2) or phase correcting Pockel's cells (PC). 12.3 MHz sidebands are put on the laser light with an RF Pockel's cell (RFPC) and the light returning from the mode cleaner cavity (mirrors M3 and M4) is extracted with a circulator (C) for RF reflection locking.

Notice that there are actually two feedback paths from the common mode servo to the

1. This gain suppresses the laser frequency noise to the noise level of the reference cavity.

laser frequency. As mentioned above, at frequencies below 3 Hz the common mode error signal is used to control the average of the two arm cavity lengths. At frequencies from 3 Hz to a few kHz, the error signal is used to control the length of the reference cavity. At frequencies above this to several hundred kHz, the common mode signal is summed directly into the laser servo.

Power stabilization of the laser light is also provided by a power stabilization servo. A small fraction of the light directly before the beam splitter is diverted to a photodiode. The difference between the power on this photodiode and a reference level is used to control an acousto-optic modulator which diverts power out of the laser beam to maintain a constant power level incident on the beam splitter. For diagnostic purposes an independent and low noise photodiode is available as well to monitor a fraction of the light incident on the beam splitter. This is the so called Z1 photodiode.

Appendix F: Design of the Beam Splitter Servo

The beam splitter servo is the only servo that had to be designed "from scratch" for the recombined interferometer. This appendix discusses the design criteria and techniques that were used to settle on a particular open loop shape.

In general servo loops have some frequency band (typically lower frequencies) where they must actively control the degree of freedom they are sensing. It is assumed that in this frequency band the sensor noise is much lower than the disturbances that must be suppressed (or else we need a more quiet sensor to proceed) and the important performance criteria in this region is the degree of suppression that is needed, or equivalently, the open loop gain.

In some frequency region outside this band where the servo is "active" (typically higher frequencies), the sensor noise may be larger than the size of the natural disturbances or the dynamics of the system may be poorly understood. The disturbances are assumed to be small enough in this frequency region that the natural motion of the degree of freedom is acceptable without servo control. The performance criteria in this frequency band is that the servo system does not make things unacceptably worse. This is the fundamental trade-off in single-input, single-output (SISO) servo design: the servo must adequately control low frequency motions without exciting the system to unacceptably high levels at higher frequencies in the process.

For the beam splitter servo, the low frequency criteria is taken from Table 2-3. The rms deviation of the Michelson near mirror difference after suppression by the servo must be less than 4×10^{-9} m_{rms}.

The criteria for higher frequencies is that the motion of the beam splitter in the gravitational wave band must not corrupt the gravitational wave signal.[1] This is potentially a problem because the sensing of the beam splitter position is fairly noisy due to shot noise.

Quantitatively, we require that above 100 Hz the gravitational wave sensitivity limit due to beam splitter motion is less than two times the limit due to shot noise in the gravitational wave signal.[2] At these frequencies the beam splitter control loop sensors will be dominated by shot noise and will impress this noise multiplied by the complementary sensitivity, T, upon the beam splitter position. The complementary sensitivity is defined as

$$T = \frac{G}{1+G} \qquad \text{F-1}$$

where G is the open loop gain in the beam splitter servo loop. Thus we require that for $f \geq$ 100 Hz,

$$T(f) < 2\left(\frac{S_{\phi_- \rightarrow \Phi_-}(0)}{S_{\Phi_-}(0)}\right)^{-\frac{1}{2}} \qquad \text{F-2}$$

Therefore, from Eq. 3-12, $T(f > 100\ \text{Hz}) < 0.34$, or equivalently the open loop gain of the beam splitter servo must satisfy

$$G(f > 100\ \text{Hz}) < 0.5 \qquad \text{F-3}$$

Using these two criteria the beam splitter open loop gain was designed iteratively. The

1. Another criteria, which is not important in this case but of concern in other designs, is that the open loop gain be substantially less than one at frequencies where the beam splitter has its internal mode resonances. Driving the beam splitter at these frequencies will produce a peak in the response which could cause the servo loop to become unstable. The internal modes of the beam splitter are all at frequencies well above 1 kHz and thus are not of concern here.
2. The sensitivity limit due to shot noise in the gravitational wave signal is less than 3×10^{-19} $\text{m}/\sqrt{\text{Hz}}$ at 100 Hz, while the best displacement sensitivity ever achieved in the 40-m interferometer at 100 Hz is 6×10^{-18} $\text{m}/\sqrt{\text{Hz}}$. This requirement corresponds to a factor of ten margin.

disturbance spectrum was taken to be roughly ten times the LIGO standard spectrum of test mass motion.[1] Each potential loop shape had to meet the criteria that it had high enough low frequency gain that it suppressed the rms beam splitter motion to the level desired and was below 0.5 at 100 Hz. A computer algorithm was used to ensure stability which gives the optimal behavior (in some sense) at the unity gain crossing while modifying the input loop gain as little as possible where it is much higher or lower than one.[2] Generally the modified loop gain output by the computer had quite a large number of poles and zeros. Thus the procedure was iterated to find a loop shape which was close to the "optimal" loop shape while being reasonable to construct with analog electronics. The open loop gain as implemented in the 40-m interferometer, after some modifications necessary because several electrical components did not perform as expected,[3] is shown in Figure F-1.

---

1. The LIGO standard spectrum assumes a site with less seismic noise than the 40-m interferometer and also includes the effect of slightly better isolation than is provided by the seismic isolation stacks currently installed in the 40-m interferometer.
2. The algorithm is "ncfsyn" which is part of the μ-Tools package for MATLAB. The method uses normalized coprime factor descriptions of the loop gain to attempt to robustly stabilize it in some optimal sense. The algorithm is described in detail in [79] and [80].
3. The beam splitter servo amplifier transfer function did not meet specifications as delivered in the critical frequency region between 50 and 100 Hz. In addition the response of the beam splitter OSEM module or the drive coils provided more phase lag than initially expected. Both of these things were compensated for by additional electronics added after the beam splitter servo amplifier.

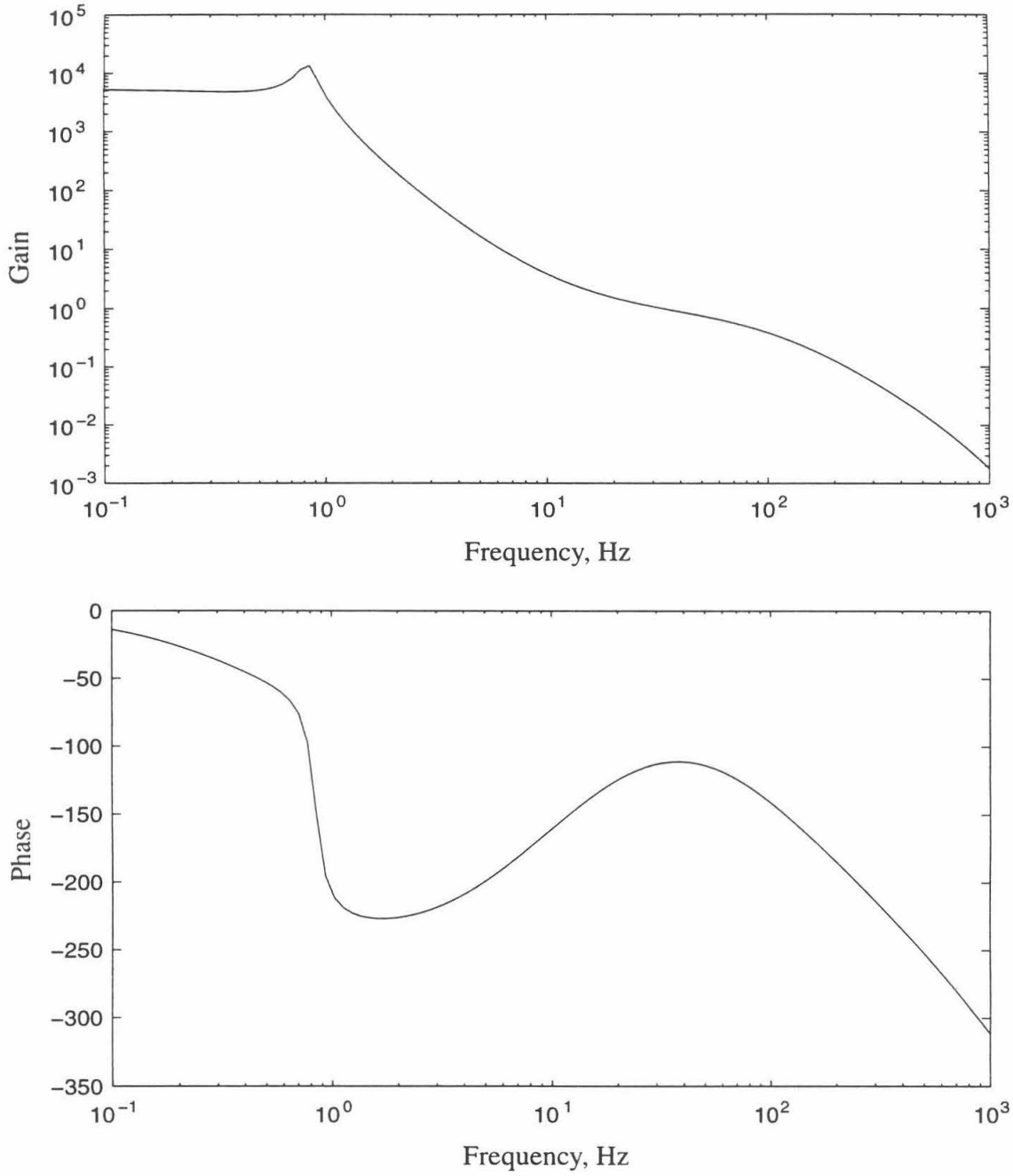

Figure F-1: Open loop gain of the beam splitter servo.

Bibliography

[1] J. Weber, Phys. Rev. **117** (1960) 306.

[2] P.F. Michelson, J.C. Price, and R.C. Taber, Science **237** (1987) 150.

[3] W.O. Hamliton, in *Proccedings of the Sixth Marcel Grossman Meeting on General Relativity*, ed. H. Sato (World Scientific, Singapore, 1993).

[4] G.E. Moss, L.R. Miller, and R.L. Forward, Applied Optics **10** (1971) 2495.

[5] R. Weiss, *Quarterly Progress Report of the Research Laboratory of Electronics of the Massachusetts Institute of Technology*, **105** (1972) 54.

[6] R.L. Forward, Phys. Rev. D **17** (1978) 379.

[7] P. Bender, I. Ciufolini, J. Cornelisse, K. Danzmann, W. Folkner, F. Hechler, J. Hough, Y. Jafry, R. Reinhard, D. Robertson, A. Rüdiger, M. Sandford, R. Schilling, B. Schutz, R. Stebbins, T. Sumner, P. Touboul, S. Vitale, H. Ward, and W. Winkler, *LISA: Laser Interferometer Space Antenna for the Detection and Observation of Gravitational Waves, Pre-Phase A Report*, Max-Planck-Institut für Quantenoptik Internal Report **208** (1995).

[8] A. Abramovici, W.E. Althouse, R.W.P. Drever, Y. Gursel, S. Kawamura, F.J. Raab, D. Shoemaker, L. Sievers, R.E. Spero, K.S. Thorne, R.E. Vogt, R. Weiss, S.E. Whitcomb, and M.E. Zucker, Science **256** (1992) 325.

[9] R. Weiss and A. Lazzarini, "LIGO Science Requirements Document," Internal LIGO document LIGO-E950018-02-E (1995).

[10] K. Danzmann, H. Lück, A. Rüdiger, R. Schilling, M. Schrempel, W. Winkler, J. Hough, G.P. Newton, N.A. Robertson, H. Ward, A.M. Campbell, J.E. Logan, D.I. Robertson, K.A. Strain, J.R.J. Bennett, V. Kose, M. Kühne, B.F. Schutz, D.

Nicholson, J. Shuttleworth, H. Welling, P. Aufmuth, R. Rinkleff, A. Tünnermann, and B. Willke, "GEO 600. A 600m Laser Interferometric Gravitational Wave Antenna," in *Proceedings of the First Edoardo Amaldi Conference on Gravitational Wave Experiments*, ed. E. Coccia, G. Pizzella and F. Ronga (World Scientific, Singapore, 1995).

[11] R.W.P. Drever, G.M. Ford, J. Hough, I.M. Kerr, A.J. Munley, J.R. Pugh, N.A. Robertson, and H. Ward, "A Gravity-Wave Detector Using Optical Cavity Sensing," 9th International Conference on General Relativity and Gravitation at Jena, GDR (1980).

[12] R.W.P. Drever, in *Gravitational Radiation*, ed. N. Deruelle and T. Piran (North Holland, Amsterdam, 1983), 321.

[13] C. Bradaschia, R. Del Fabbro, A. Di Virgilio, A. Giazotto, H. Kauzky, V. Montelatici, D. Passuello, A. Brillet, O. Cregut, P. Hello, C.N. Man, P.T. Manh, A. Marroud, D. Shoemaker, J.Y. Vinet, F. Barone, L. di Fiore, L. Milano, G. Russo, J.M. Aguirregabiria, H. Bel, J.P. Duruisseau, G. le Denmat, Ph. Tourrenc, M. Capozzi, M. Longo, M. Lops, I. Pinto, G. Rotoli, T. Damour, S. Bonazzolla, J.A. Marck, Y. Gourghoulon, L.E. Holloway, F. Fuligni, V. Iafolla, and G. Natale, Nucl. Instrum. Methods A **289** (1990) 518.

[14] J.D. Jackson, *Classical Electrodynamics, Second Edition* (John Wiley & Sons, 1975), 271.

[15] M.W. Regehr, *Signal Extraction and Control for an Interferometric Gravitational Wave Detector,* Ph.D. Thesis, California Institute of Technology, 1995.

[16] J.A. Giaime, *Studies of Laser Interferometer Design and a Vibration Isolation Sys-*

tem for Interferometric Gravitational Wave Detectors, Ph.D. Thesis, Massachusetts Institute of Technology, 1995.

[17] D. Shoemaker, J. Giaime, F. Raab, M. Regehr, and L. Sievers, "Comparison of 2 Fixed Mass Interferometer Testbeds and the Resulting Recommendation for the Initial LIGO Interferometer Design," Internal LIGO document (1993).

[18] R.E. Spero, "In-Situ Measurement of Cavity Parameters Needed for Calculating Shot Noise," Internal LIGO document LIGO-T940065-00-R (1994).

[19] A. Yariv, *Optical Electronics, Fourth Edition* (Saunders College Publishing, San Francisco, 1991), p. 54.

[20] Regehr, pp. 32-36.

[21] Regehr, Chapter 4.

[22] This section is largely taken with corrections from T. Lyons and M. Regehr, "Shot Noise in a Recycled Unbalanced LIGO," unpublished (1994).

[23] T.M. Niebauer, R. Schilling, K. Danzmann, A. Rüdiger, and W. Winkler, Phys. Rev. A **43** (1991) 5022.

[24] D. Shoemaker, P. Fritschel, J. Giaime, N. Christensen, and R. Weiss, Applied Optics **30** (1991) 3133.

[25] W.A. Gardner and L.E. Franks, IEEE Trans. on Information Theory **IT-21** (1975) 4.

[26] A. Papoulis, Probability, Random Variables, and Stochastic Processes, Third Edition (McGraw-Hill, San Francisco, 1991), pp. 373-374.

[27] D.Z. Anderson, Applied Optics **23** (1984) 2944.

[28] Yariv, p. 121.

[29] This section follows very closely the treatment given in Regehr, Appendix B.

[30] J. Camp, "Frequency, Intensity, and Oscillator Noise in the LIGO," Internal LIGO document LIGO-T960019-00-D (1996).

[31] D. Shoemaker, "Modulation and topology: Deviations from resonance," Internal LIGO document (1991).

[32] Regehr, p. 151, equation (B.5).

[33] A. Abramovici, W. Althouse, J. Camp, D. Durance, J.A. Giaime, A. Gillespie, S. Kawamura, A. Kuhnert, T. Lyons, F.J. Raab, R.L. Savage, Jr., D. Shoemaker, L. Sievers, R. Spero, R. Vogt, R. Weiss, S. Whitcomb, and M. Zucker, Phys. Let. A **218** (1996) 157.

[34] A.D. Gillespie, *Thermal Noise in the Initial LIGO Interferometers*, Ph.D. Thesis, California Institute of Technology, 1995.

[35] J. Camp, L. Sievers, R. Bork, and J. Heefner, Optics Letters **20** (1995) 2463.

[36] Regehr, pp. 88-90.

[37] Regehr, p. 91.

[38] D. Schnier and K. Danzmann, "Recycling of light power and external modulation on the Garching 30m Interferometer with suspended optical components," Verhandl. DPG (VI) 31, Q 11.2 (1996).

[39] M.-K. Fujimoto, M. Ohashi, T. Yamazaki, M. Fukushima, A. Araya, K. Tsubono, N. Mio, and S. Telada, "Development of a 20m Prototype Laser Interferometric Gravitational Wave Detector at NAO," in *Proceedings of the First Edoardo Amaldi Conference on Gravitational Wave Experiments*, ed. E. Coccia, G. Pizzella and F. Ronga (World Scientific, Singapore, 1995).

[40] G.A. Kerr, *Experimental Developments towards a Long Baseline Gravitational Radi-*

ation Detector, Ph.D. Thesis, University of Glasgow, 1986, pp. 117-130.

[41] A. Gillespie and F. Raab, Phys. Lett. A **178** (1993) 357.

[42] D.Z. Anderson, J.C. Frisch, and C.S. Masser, Applied Optics **23** (1984) 1238.

[43] E.L. Church, P.Z. Takacs, and T.A. Leonard, in *Scatter from Optical Components*, ed. J.C. Stover, Proc. SPIE **1165** (1989), 136.

[44] J.C. Stover, *Optical Scattering, Measurement and Analysis* (McGraw-Hill, San Francisco, 1990), 60-61.

[45] Stover, Chapter 5.

[46] Stover, p. 37.

[47] E.L. Church, H.A. Jenkinson, J.M. Zavada, Optical Engineering **18** (1979), 125.

[48] Stover, p. 83.

[49] This section and the following discussion of optical contamination in vacuum is taken from A. Abramovici, T.T. Lyons, and F.J. Raab, Applied Optics **34** (1995) 183, and is presented here in context.

[50] J. Giaime, P. Saha, D. Shoemaker, and L. Sievers, Rev. Sci. Instrum. **67** (1996) 208.

[51] See, for example, A.P. Glassford, ed., *Optical System Contamination: Effects, Measurement, Control*, Proc. Soc. Photo-Opt. Instrum. Eng. **777** (1987), **1329** (1990), **1754** (1992).

[52] R.W.P. Drever, J.L. Hall, F.V. Kowalski, J. Hough, G.M. Ford, A.J. Munley, and H. Ward, Appl. Phys. B **31** (1983) 97.

[53] J. Mason, private communication (1996).

[54] K.S. Thorne, in *Particle and Nuclear Astrophysics and Cosmology in the Next Millennium*, ed. E.W. Kolb and R. Peccei (World Scientific, 1995).

[55] B. Schutz, in *The Detection of Gravitational Waves*, ed. D.G. Blair (Cambridge University Press, Cambridge, 1991).

[56] L. Blanchet, T. Damour, B.R. Iyer, C.M. Will, and A.G. Wiseman, Phys. Rev. Lett. **74** (1995) 3515.

[57] T.A. Apostolatos, C. Cutler, G.J. Sussman, and K.S. Thorne, Phys. Rev. D **49** (1994) 6274.

[58] H. Tagoshi and M. Sasaki, Prog. Theor. Phys. **92** (1994) 745.

[59] R. Narayan, T. Piran and A. Shemi, Ap. J. **379** (1991) L17.

[60] E.S. Phinney, Ap. J. **380** (1991) L17.

[61] S.V. Dhurandhar and B.S. Sathyaprakash, Phys. Rev. D **49** (1994) 1707.

[62] T.A. Apostolatos, Phys. Rev. D **52** (1995) 605.

[63] T.M. Niebauer, A. Rudiger, R. Schilling, L. Schnupp, W. Winkler and K. Danzmann, Phys. Rev. D **47** (1993) 3106.

[64] S.C. Smith, J.L. Houser, and J.M. Centrella, Ap. J. **458** (1996) 236.

[65] A.D. Gillespie, *Thermal Noise in the Initial LIGO Interferometers*, Ph.D. Thesis, California Institute of Technology, 1995.

[66] S. Smith, *A Search for Gravitational Waves from Coalescing Binary Stars Using the Caltech 40 Meter Gravity Wave Detector,* Ph.D. Thesis, California Institute of Technology, 1988.

[67] M.E. Zucker, *Experiments with a Laser Interferometer Gravitational Wave Antenna*, Ph.D. Thesis, California Institute of Technology, 1989.

[68] J.C. Livas, *Upper Limits for Gravitational Radiation From Some Astrophysical Sources*, Ph.D. Thesis, Massachusetts Institute of Technology, 1987.

[69] The primer on digitization noise given in this section follows closely the treatment of A.V. Oppenheim and R.W. Schafer, *Digital Signal Processing* (Prentice-Hall, New Jersey, 1975), pp. 404-418.

[70] Oppenheim, pp. 26-30.

[71] W.H. Press, S.A. Teukolsky, W.T. Vetterling, and B.P. Flannery, *Numerical Recipes in C, The Art of Scientific Computing, Second Edition* (Cambridge University Press, Cambridge, 1992), Chapter 12 and references therein.

[72] D. Dewey, *A Search for Astronomical Gravitational Radiation with an Interferometric Broad Band Antenna*, Ph.D. Thesis, Massachusetts Institute of Technology, 1986.

[73] Most of this calculation is also shown in Regehr, Appendix A.

[74] Papoulis, pp. 57-60 and p. 290.

[75] Papoulis, pp. 313-314.

[76] Papoulis, p. 291, equation (10-17).

[77] Papoulis, p. 313-314, equation (10-95).

[78] Papoulis, P. 314, equation (10-100).

[79] D.C. McFarlane and K. Glover, IEEE Trans. Auto. Control **37** (1992) 759.

[80] D.C. McFarlane and K. Glover, *Robust Controller Design Using Normalized Coprime Factor Plant Descriptions*, Lecture Notes in Control and Information Sciences **138** (Springer Verlag, 1989).